Universidade de Aveiro
2014
Departamento de Eletrónica, Telecomunicações e Informática

Susana de Jesus Mota

Modelos de Canal para Sistemas MIMO

Channel Modeling for MIMO Systems

Universidade de Aveiro
2014
Departamento de Eletrónica, Telecomunicações e Informática

Susana de Jesus Mota

Modelos de Canal para Sistemas MIMO

Channel Modeling for MIMO Systems

Tese apresentada à Universidade de Aveiro para cumprimento dos requisitos necessários à obtenção do grau de Doutor em Engenharia Eletrotécnica, realizada sob a orientação científica do Doutor Armando Carlos Domingues da Rocha, Professor Auxiliar do Departamento de Eletrónica, Telecomunicações e Informática da Universidade de Aveiro

Apoio financeiro da FCT e do FSE

À minha família

“*Alea jacta est* ”

Júlio César

o júri

presidente

Doutor Vítor José Babau Torres
Professor Catedrático da Universidade de Aveiro

Doutor Francisco António Bucho Cercas
Professor Catedrático do ISCTE-IUL – Instituto Universitário de Lisboa

Doutor Fernando Pérez-Fontán
Professor Catedrático da Universidade de Vigo

Doutor João Nuno Pimentel Silva Matos
Professor Associado da Universidade de Aveiro

Doutor Fernando José da Silva Velez
Professor Auxiliar da Universidade da Beira Interior

Doutor Armando Carlos Domingues da Rocha
Professor Auxiliar da Universidade de Aveiro (Orientador)

agradecimentos

Ao Prof. Doutor Armando Rocha, meu orientador, pelo apoio, pela disponibilidade, pelo aconselhamento, pela sua orientação afinada e focalizada evitando desvios vãos, por todos os esforços que desenvolveu e acima de tudo, pela paciência e compreensão. Devo também pela sua iniciativa de solicitar a colaboração do Prof. Doutor Fernando Pérez-Fontán da Universidade de Vigo, Espanha.

Ao Prof. Doutor Fernando Pérez-Fontán, por me ter acolhido tão prontamente e cordialmente, pelas discussões proveitosas que mantivemos, pelas sugestões, pela motivação que sempre me transmitiu e ainda por todo o empenho que mostrou para tornar possíveis as reuniões que fomos mantendo periodicamente.

Ao Instituto de Telecomunicações – polo de Aveiro, pelas condições de trabalho que me proporcionou.

A toda a equipa técnica do Instituto de Telecomunicações, por todo apoio prestado, especialmente ao Miguel Lacerda e ao Paulo Gonçalves pelo apoio durante as campanhas de medidas.

À Fundação para a Ciência e Tecnologia (FCT), pela bolsa concedida (Ref.ª SFRH / BD / 6418 / 2001).

À minha família, em especial ao meu marido, à minha filha, aos meus pais, à minha irmã e ao meu cunhado pelo apoio contínuo.

Também a todos os meus amigos pelo facto de o serem, mas em especial ao amigo Lucénio pelo seu apoio, pelo seus esforços e pela confiança que em mim depositou.

palavras-chave

Sistemas MIMO, Modelos de Canal, Multipercurso, Canal Rádio Direcional, Medidas Experimentais, Estimação Paramétrica, Classificação de Dados

resumo

Os sistemas equipados com múltiplas antenas no emissor e no recetor, conhecidos como sistemas MIMO (*Multiple Input Multiple Output*), oferecem capacidades mais elevadas, permitindo melhor rentabilização do espectro e/ou utilização de aplicações mais exigentes. É sobejamente sabido que o canal rádio é caracterizado por propagação multipercurso, fenómeno considerado problemático e cuja mitigação tem sido conseguida através de técnicas como diversidade, formatação de feixe ou antenas adaptativas. Explorando convenientemente o domínio espacial os sistemas MIMO transformam as características multipercurso do canal numa mais-valia e permitem criar vários canais virtuais, paralelos e independentes. Contudo, os benefícios atingíveis são condicionados pelas características do canal de propagação, que poderão não ser sempre as ideais.

Este trabalho centra-se na caracterização do canal rádio para sistemas MIMO. Inicia-se com a apresentação dos resultados fundamentais da teoria da informação que despoletaram todo o entusiamo em torno deste tipo de sistemas, sendo discutidas algumas das suas potencialidades e uma revisão dos modelos existentes para sistemas MIMO.

A caracterização do canal MIMO desenvolvida neste trabalho assenta em medidas experimentais do canal direcional adquiridas em dupla via. O sistema de medida é baseado num analisador de redes vetorial e numa plataforma de posicionamento bidimensional, ambos controlados por um computador, permitindo obter a resposta em frequência do canal rádio nos vários pontos correspondentes à localização dos elementos de um agregado virtual. As medidas são posteriormente processadas com o algoritmo SAGE (*Space-Alternating Expectation-Maximization*), de forma a obter os parâmetros (atraso, direção de chegada e amplitude complexa) das componentes multipercurso mais significativas. Seguidamente, estes dados são tratados com um algoritmo de classificação (*clustering*) e organizados em grupos. Finalmente é extraída informação estatística que permite caracterizar o comportamento das componentes multipercurso do canal.

A informação acerca das características multipercurso do canal, induzidas pelos espalhadores (*scatterers*) existentes no cenário de propagação, possibilita a caracterização do canal MIMO e assim avaliar o seu desempenho. O método foi por fim validado com medidas MIMO.

keywords

MIMO Systems, Channel Models, Multipath, Diretional Radio Channel, Experimental Measurements, Parametric Estimation, Data Clustering

abstract

Systems equipped with multiple antennas at the transmitter and at the receiver, known as MIMO (Multiple Input Multiple Output) systems, offer higher capacities, allowing an efficient exploitation of the available spectrum and/or the employment of more demanding applications. It is well known that the radio channel is characterized by multipath propagation, a phenomenon deemed problematic and whose mitigation has been achieved through techniques such as diversity, beamforming or adaptive antennas. By exploring conveniently the spatial domain MIMO systems turn the characteristics of the multipath channel into an advantage and allow creating multiple parallel and independent virtual channels. However, the achievable benefits are constrained by the propagation channel's characteristics, which may not always be ideal.

This work focuses on the characterization of the MIMO radio channel. It begins with the presentation of the fundamental results from information theory that triggered the interest on these systems, including the discussion of some of their potential benefits and a review of the existing channel models for MIMO systems.

The characterization of the MIMO channel developed in this work is based on experimental measurements of the double-directional channel. The measurement system is based on a vector network analyzer and a two-dimensional positioning platform, both controlled by a computer, allowing the measurement of the channel's frequency response at the locations of a synthetic array. Data is then processed using the SAGE (Space-Alternating Expectation-Maximization) algorithm to obtain the parameters (delay, direction of arrival and complex amplitude) of the channel's most relevant multipath components. Afterwards, using a clustering algorithm these data are grouped into clusters. Finally, statistical information is extracted allowing the characterization of the channel's multipath components.

The information about the multipath characteristics of the channel, induced by existing scatterers in the propagation scenario, enables the characterization of MIMO channel and thus to evaluate its performance. The method was finally validated using MIMO measurements.

Table of Contents

List of Figures

List of Tables

Notation and List of Symbols

Throughout the thesis, the following notation is used to represent common operators:

$(\bullet)^*$	Complex conjugate operator
$\otimes$	Convolution operator
$\|\bullet\|$	Euclidean norm
$\mathrm{E}[\ ]$	Mathematical expectation
$[\bullet]^H$	Matrix conjugate-transpose operator
$[\bullet]^{\mathrm{T}}$	Matrix transposition operator

List of most symbols used through the thesis

$c(\phi,\theta)$	Array steering vector
$R_h(\tau_1,\tau_2,t_1,t_2)$	Autocorrelation function of the impulse response
D_τ	Average delay
ϕ	Azimuth
ν_{CH}	Calinski-Harabasz index value
c_k	Centroid of the *k*-th cluster
C	Channel capacity
B_c	Coherence bandwidth
$X_\ell(f)$	Complete data
α	Complex Amplitude

$h(\tau;\theta_\ell)$	Contribution of the ℓ-th MPC to the array impulse response
$S(f;\theta_\ell)$	Contribution of the ℓ-th MPC to the channel transfer function
r_m	Coordinates of the *m*-th antenna element
Kr	Decision rank fusion value
ζ	Delay scaling factor
S_τ	Delay spread
τ	Delay variable
$\delta(\bullet)$	Dirac delta function
$\mathbf{\Omega}_{rx}$	Direction of arraival
$\mathbf{\Omega}_{tx}$	Direction of departure
$\Delta_{\mathrm{Tx}}/\Delta_{\mathrm{Rx}}$	Distance between antennas at transmitter/receiver
d_0^{ij}	Distance from the *j*-th transmit antenna to the *i*-th receive antenna
$\mathrm{d}_1^{\ell j}$	Distance from the *j*-th transmit antenna to the ℓ-th scatterer
$\mathrm{d}_2^{i\ell}$	Distance from the ℓ-th scatterer to the *i*-th receive antenna
β	Elevation
e	Ellipse eccentricity
a	Ellipse semi-major axis
b	Ellipse semi-minor axis
$\hat{\theta}$	Estimate of θ
$\hat{x}_\ell(f;\hat{\theta}')$	Estimate of the complete data
f	Frequency variable
ν_{Dij}	Generalized Dunn's index using δ_i/Δ_j the
I_M	Identity matrix of size MxM
λ_i	*i*-th eigenvalue of the channel
$\Lambda(\theta;y)$	Log-likelihood function of θ given an observation y
$\mathbf{D}$	Matrix of channel singular values
$\mathbf{n}(t)$	Noise vector
L	Number of channel multipath components
K	Number of clusters

Nr	Number of receiving antennas
M	Number of receiving sensors
Nt	Number of transmitting antennas
ν_{PBM}	PBM index value
φ_ℓ	Phase of the ℓ-th channel scatterer
Γ	Power decay constant for clusters (Saleh-Valenzuela model)
γ	Power decay constant for MPCs (Saleh-Valenzuela model)
S_k	Power decay slope
P_{ck}	Power of cluster *ck*
K_0	Power ratio for cluster 0
K_1	Power ratio for clusters type 1
K_2	Power ratio for clusters type 2
$p_h(\tau)$	Power-delay profile
$\mathbf{y}(t)$	Received signal
$S(\tau,\nu)$	Scattering function
SF-A	Score fusion-arithmetic mean value
SF-G	Score fusion-geometric mean value
SF-Med	Score fusion-median value
δ_i / Δ_j	Set distance / Cluster diameter
ρ	Signal to noise ratio
c	Speed of light in vacuum
σ	Standard deviation
t	Time variable
$h_{ij}(t,\tau)$	Time-variant impulse response from *j*-th transmit antenna to *i*-th receive antenna
$\mathbf{H}(t,\tau)$	Time-variant impulse response matrix
$T(f,t)$	Time-variant transfer function
$H(f)$	Transfer function
P_T	Transmitted power
$\mathbf{s}(t)$	Transmitted signal
Ψ_{Tx} / Ψ_{Rx}	Transmitter/receiver array orientation referred to *x*-axis

$\Phi_{\mathrm{Tx}} / \Phi_{\mathrm{Rx}}$	Transmitter/receiver route direction referred to *x*-axis
$\delta_{\mathrm{Tx}} / \delta_{\mathrm{Tx}}$	Transmitter/receiver route sampling step
$e(\phi, \beta)$	Unit vector in $\mathbb{R}^3$ pointing toward direction defined by ϕ and β
θ	Vector containing the parameters of L MPCs
θ_ℓ	Vector containing the parameters of the ℓ-th MPC
λ	Wavelength
ν_{XB}	Xie-Beni index value

Acronyms

3GPP	3th Generation Partnership Project
ACF	Autocorrelation Function
AIC	Akaike Information Criterion
BWA	Broadband Wireless Access
CDF	Cumulative Density Function
CDMA	Code Division Multiple Access
CH	Calinski-Harabasz Validity Index
COST	European Cooperation in Science and Technology
CSI	Channel State Information
CVI	Cluster Validity Index
DCIR	Directional Channel Impulse Response
DoA	Direction of Arrival
DoD	Direction of Departure
DPE	Deterministic Parameter Estimation
DSF	Delay Scaling Factor
EM	Expectation-Maximization
ESPRIT	Estimation of Signal Parameter via Rotational Invariance Technique
ESV	Extended Saleh Valenzuela model
ETSI	European Telecommunications Standards Institute
FD-SAGE	Frequency Domain Space-Alternating Generalized Expectation Maximization

GO	Geometrical Optics
GPIB	General Purpose Interface Bus
GSCM	Geometry-based Stochastic Channel Model
HiperMAN	High Performance Radio Metropolitan Area Network
IEEE	Institute of Electrical and Electronics Engineers
IFFT	Inverse Fast Fourier Transform
IR	Impulse Response
ITU	International Telecommunication Union
KPM	KPowerMeans
LoS	Line-of-Sight
LTE	Long Term Evolution
MAC	Medium Access Control
MCD	Multipath Component Distance
MDL	Minimum Description Length
MIMO	Multiple-Input Multiple-Output
MISO	Multiple-Input Single-Output
MLE	Maximum Likelihood Estimation
MPC	Multipath Component
MUSIC	Multiple Signal Classification
OFDM	Orthogonal Frequency Division Multiplex
OLoS	Obstructed Line of Sight
PDP	Power-Delay Profile
PMP	Point-to-Multipoint
PP	Point-to-Point
PSBE	Parametric Subspace Based Estimation
RF	Radio Frequency
SAGE	Space-Alternating Generalized Expectation-Maximization
SCM	Spatial Channel Model
SCME	Spatial Channel Model Extended

SDMA	Space Division Multiple Access
SFIR	Spatial Filtering for Interference Reduction
SIMO	Single-Input Multiple-Output
SISO	Single-Input Single-Output
SNR	Signal to Noise Ratio
STC	Space Time Code
SUI	Stanford University Interim
SV	Saleh and Valenzuela
ToA	Time of Arrival
US	Uncorrelated Scattering
V-BLAST	Vertical – Bell Labs Layered Space Time
VNA	Vector Network Analyzer
W-CDMA	Wideband Code Division Multiple Access
WIM I	WINNER Phase I channel model
WIM II	WINNER Phase II channel model
WiMax	Worldwide Interoperability for Microwave Access
WINNER	Wireless World Initiative New Radio
WLAN	Wireless Local Area Network
WSS	Wide Sense Stationary
WSSUS	Wide Sense Stationary Uncorrelated Scattering
XB	Xie-Beni Validity Index

Chapter 1

Introduction

Personal wireless communications are certainly a story of true success. The most obvious is perhaps the case of mobile communications, where the achievement is due to its attractiveness and users' acceptance on the one hand and on the other, a great competition between operators of mobile networks which allows providing reasonable prices for the advantages that these networks offer when compared with the fixed network. However, nowadays other types of wireless communications such as WLANs (Wireless Local Area Networks) and fixed broadband wireless accesses also take prominent places in society. These services have been experiencing an increasing need for higher transmission rates, capacity and quality of service owing to the increase of users and also owing to the emergence of more demanding applications.

Power and spectrum constraints enforce a difficult challenge: to enhance the performance, under unfriendly conditions, without increasing the power or spectrum requirements. The radio channel is particularly problematical due to phenomena as multipath, fading, shadowing, time dispersion and Doppler shift. A convenient use of the assigned frequency bands is required so new, appealing and ground-breaking services may be placed at the users' disposal. Therefore, solutions able to exploit efficiently the available spectrum need to be employed, not only for mobile communications but also for other types of wireless communications.

Early communication systems were based on the use of one antenna at transmitter and one antenna at the receiver being known as SISO (Single-Input Single-Output) systems. This kind of systems allows exploiting time, frequency and codification domains. By employing smart antennas techniques – systems where several antennas are available at one side (usually at the base station) – it is possible to exploit partially the spatial domain [1-3]. Namely, it is possible to benefit from the advantages offered by spatial diversity techniques [4, 5] and/or from the gains given by beamforming [6, 7].

MIMO (Multiple-Input Multiple-Output) systems employ several antennas at both link ends (i.e., at the transmitter and at the receiver) and may be perceived as the logical extension of smart antennas technology and allow to fully exploit the spatial domain. These systems promise more than the simultaneous use, at the transmitter and at the receiver, of spatial diversity or beamforming. Studies presented in [8] and [9] showed that by using MIMO technology in an environment characterized by an high number of independent multipath components the capacity linearly grows with the minimum number of transmit and receive antennas, while the use of several antennas at one link end only provides a logarithmic increase. The concept of *spatial multiplexing* is the key for this result: the multipath propagation characteristics are conveniently exploited so several parallel non-interfering virtual sub-channels are provided.

Results on the capacity gains offered by MIMO systems, provided by early studies, stimulated the interest on these systems in the area of space-time signal processing. A number of algorithms [10-14] have been proposed in order to achieve the gains foreseen. Nevertheless, the achievable benefits are constrained by the characteristics of the propagation channel which are not always the ideal or the most desirable. Only a comprehensive description of the propagation channel allows the assessment of the actual transmission capacity.

This work aims to be a contribution to the characterization of the radio channel for MIMO systems. The channel is described using experimental measurements of the double-directional channel. The measurement system is based on a vector network analyzer and a two-dimensional positioning platform, both controlled by a computer, allowing the measurement of the channel's frequency response at the locations of a synthetic array. Data is then processed using the SAGE (Space-Alternating Generalized Expectation-Maximization) algorithm to obtain the parameters (delay, direction of arrival and complex amplitude) of the channel's most relevant multipath components. Afterwards, using a clustering algorithm, these data are grouped into clusters. Finally, statistical information is extracted allowing the characterization of the channel's multipath

components which enables the characterization of MIMO channel and thus to evaluate its performance.

This dissertation is organized as follows:

Chapter 2 presents the fundamental results from information theory that triggered the interest on these systems, a discussion of some of their potential benefits and a review of the existing channel models for MIMO systems.

Chapter 3 starts with the theoretical characterization of the wideband directional channel impulse response. After that, the SIMO (Single-Input Multiple-Output) measurement system and the measurement campaign are presented. The measurement campaign has been carried out inside a sports hall: for each transmit-receive arrangement of positions a double-directional measurement is available, consisting of two measurement files, corresponding respectively, to the forward and reverse measurement. Subsequently, a brief review on the available methods to estimate the parameters of the multipath components arriving to a given receiver is given: the SAGE algorithm is explained in detail and its performance is evaluated using synthetic data, generated with the extended Saleh-Valenzuela model. Finally, experimental directional channel impulse responses, obtained by entering measured data into the SAGE algorithm, are given.

Chapter 4 presents an exploratory study of the experimental directional channel impulse responses obtained in Chapter 3. It begins with a brief review of the clustering algorithms, focusing mainly on the selected algorithm. Next, the clustering framework is described covering: the selected clustering algorithm; the measure function for evaluation of distance between multipath components; the algorithm initialization; and the estimation of the number of clusters that better fits the data. By using synthetic data sets, a structured study on the performance of the selected framework and procedure adjustments, motivated by this evaluation, are presented. Once more, synthetic data sets were generated with the extended Saleh-Valenzuela model. Afterwards, the clustering output solutions for the experimental directional channel impulse responses estimated in chapter 3, with the SAGE algorithm, are presented and discussed. To finish, a physical analysis relating each cluster with the scenario objects and obstacles is presented: at this stage clusters are further classified according to the type of interaction which they represent (direct ray, single-interaction, higher order interaction). Additionally, clusters from each pair of measurement files composing a double-directional measurement, are linked at this stage.

Chapter 5 explains the MIMO channel model proposed and the MIMO channel simulator implemented during this work. It starts with the envisaged channel model assumptions. In

order to parameterize this model, a statistical analysis of the categorized data is accomplished. Then, the MIMO measurement setup and the measurement campaign are described. The MIMO channel measurements are presented and used for validation purposes and so, the chapter ends with a comparison of the simulator outputs and the measurements results.

Finally, Chapter 6 summarizes the major results and achievements from this dissertation and draws some conclusions. Possible future work is also identified.

Chapter 2

MIMO Wireless Communications

This chapter presents the fundamentals of MIMO systems opening with the required mathematical analysis to obtain the capacity accomplished by the system. The MIMO link is represented using a complex matrix and its capacity is achieved using the extended Shannon's capacity formula. Subsequently, a discussion on MIMO systems potentials and benefits is presented. The remaining of the chapter is devoted to the review of the most relevant existent channel models for MIMO systems.

2.1. System Model

Taking into account that MIMO systems make use of multiple antennas at both link ends, the MIMO channel must be described between all transmit and receive antenna pairs. Consider a MIMO system equipped with *Nt* antennas at the transmitter and *Nr* antennas at the receiver, as Figure 2-1 shows. Furthermore, consider the time-variant impulse response between the *j*-th transmitting antenna and the *i*-th receiving antenna represented as $h_{i,j}(t,\tau)$.

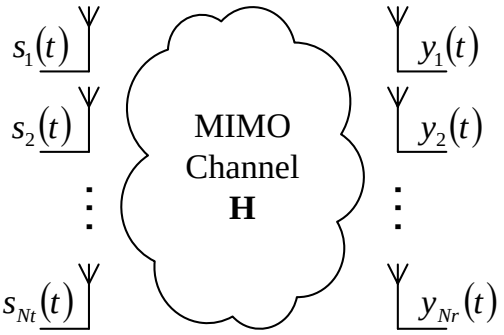

Figure 2-1: Schematic of a MIMO system with *Nt* antennas at the transmitter and *Nr* antennas at the receiver.

From a system level point of view, the linear time-variant MIMO channel may be represented by the $Nr \times Nt$ matrix, $\mathbf{H}(t,\tau)$, expressed as

$$\mathbf{H}(t,\tau) = \begin{bmatrix} h_{1,1}(t,\tau) & h_{1,2}(t,\tau) & \cdots & h_{1,Nt}(t,\tau) \\ h_{2,1}(t,\tau) & h_{2,2}(t,\tau) & \cdots & h_{2,Nt}(t,\tau) \\ \vdots & \vdots & \ddots & \vdots \\ h_{Nr,1}(t,\tau) & h_{Nr,2}(t,\tau) & \cdots & h_{Nr,Nt}(t,\tau) \end{bmatrix}. \tag{2.1}$$

Assuming $s_j(t)$ denoting the transmitted signal by the *j*-th antenna, the $Nt \times 1$ vector, $\mathbf{s}(t) = \begin{bmatrix} s_1(t) & s_2(t) & \cdots & s_{Nt}(t) \end{bmatrix}^T$, corresponds to the *Nt* transmitted signals. The vector containing the *Nr* received signals, $\mathbf{y}(t) = \begin{bmatrix} y_1(t) & y_2(t) & \cdots & y_{Nr}(t) \end{bmatrix}^T$, is then defined as

$$\mathbf{y}(t) = \int_\tau \mathbf{H}(t,\tau)\mathbf{s}(t-\tau)d\tau + \mathbf{n}(t) \tag{2.2}$$

where *t* and τ represent time and delay, respectively, and $\mathbf{n}(t)$ is a noise vector.

If time-invariant channels are taken into account, the channel matrix depends only on the delay, i.e., $\mathbf{H}(t,\tau) = \mathbf{H}(\tau)$. Therefore,

$$\mathbf{y}(t) = \int_\tau \mathbf{H}(\tau)\mathbf{s}(t-\tau)\,d\tau + \mathbf{n}(t) = \mathbf{H}(\tau) \otimes \mathbf{s}(t) + \mathbf{n}(t) \tag{2.3}$$

where $\otimes$ denote the convolution operator.

In addition, if the transmitted signal bandwidth is narrow enough that the channel response is allowed to be treated as frequency flat, the channel matrix is non-zero only for $\tau = 0$ and may be denoted simply by $\mathbf{H}$. Under this assumption, equation (2.3) may be written as

$$\mathbf{y}(t) = \mathbf{H}\mathbf{s}(t) + \mathbf{n}(t). \tag{2.4}$$

In the discrete time domain equation (2.4) may alternatively be written as

$$\mathbf{y}[k] = \mathbf{H}\mathbf{s}[k] + \mathbf{n}[k] \tag{2.5}$$

where *k* represents the index of the time sample. As may be easily concluded by observing this relation, the output at a given time instant *k* does not depend on the past inputs. Thus, aiming the legibility improvement, equation (2.5) can be simply expressed as

$$\mathbf{y} = \mathbf{H}\mathbf{s} + \mathbf{n}\,. \tag{2.6}$$

2.2. Capacity analysis

2.2.1. From Shannon to MIMO Systems Capacity

The Shannon's capacity formula provides the maximum possible rate of information transmission that can be achieved with arbitrarily small error probability, through a given channel. The instantaneous capacity, expressed in bps/Hz, of a frequency flat SISO channel (i.e., a white Gaussian channel) with complex gain *h*, is given by [8, 12]

$$C_{SISO} = \log_2\left(1 + \frac{P_T}{\sigma^2}|h|^2\right) = \log_2\left(1 + \rho|h|^2\right) \tag{2.7}$$

with P_T being the transmitted power, σ^2 the noise power and

$$\rho = \frac{P_T}{\sigma^2} \tag{2.8}$$

the Signal to Noise Ratio (SNR) at the receiver.

If receive diversity is present, it is possible to improve the capacity given the existence, at the receiver, of several replicas of the transmitted signal which potentially contribute to an increase of the SNR. Assuming *Nr* antennas at the receiver and maximum ratio combining, the SIMO capacity is defined as [14]

$$C_{SIMO} = \log_2\left(1 + \rho\sum_{i=1}^{Nr}|h_i|^2\right) \tag{2.9}$$

where h_i is the gain of the channel established between the transmit antenna and the *i*-th receive antenna. Similarly, in a transmit diversity case with *Nt* transmitting antennas, if we consider constant total transmit power (P_T) and no Channel State Information (CSI) at the transmitter, the transmit power is equally distributed by the transmitting antennas and MISO (Multiple-Input Single-Output) capacity is given by

$$C_{MISO} = \log_2\left(1 + \frac{\rho}{Nt}\sum_{j=1}^{Nt}|h_i|^2\right). \tag{2.10}$$

Examining equations (2.9) and (2.10) it is obvious that SIMO and MISO capacities increase logarithmically with the linear increase in the number of receive antennas, *Nr*, and transmit antennas, *Nt*, respectively. Moreover, it is easy to notice that $C_{SIMO} > C_{MISO}$. This result can be explained by the impossibility of the transmitter, in the MISO channel, to conveniently exploit the antenna array gain, since it has no CSI. Assuming a MISO channel with CSI and identical channel conditions, it is possible to show [13] that MISO capacity equals SIMO capacity.

Consider now the use of multiple antennas at both link ends. In this case, the channel presents multiple inputs as well as multiple outputs and its capacity may be computed by the extended Shannon's capacity formula presented in [8] and [9], defined as

$$C_{MIMO} = \max_{\mathbf{Q}:\mathrm{tr}(\mathbf{Q})\le\rho}\left\{\log_2\left(\det\left(\mathbf{I}_{Nr} + \mathbf{HQH}^H\right)\right)\right\} \tag{2.11}$$

where $\mathbf{I}_{Nr}$ is the $Nr \times Nr$ identity matrix, $\mathbf{H}^H$ represents the conjugate transpose matrix of $\mathbf{H}$ and $\mathbf{Q} = \mathrm{E}\left[\mathbf{ss}^H\right]$ is the $Nt \times Nt$ covariance matrix of the transmitted vector **s**, with $\mathrm{E}[\ ]$ being the mathematical expectation. The condition $\mathrm{tr}(\mathbf{Q}) = \rho$ must be satisfied in order to constrain the total transmit power to P_T, regardless of number of transmitting antennas (*Nt*).

2.2.2. Eigenvalue Analysis of the Channel

No CSI at the transmitter

If the transmitter has no CSI, the *Nt* components of the transmitted signal vector should be statistically independent and equally powered [13]. In this case, we have $\mathbf{Q} = (\rho/Nt)\mathbf{I}_{Nt}$ and

$$C_{UP} = \log_2\left(\det\left(\mathbf{I}_{Nr} + \frac{\rho}{Nt}\mathbf{HH}^H\right)\right). \tag{2.12}$$

It can be shown that the MIMO channel capacity given by this equation increases linearly with the minimum number of transmit and receive antennas (*Nt* and *Nr*), contrasting with the logarithmically increase offered by the capacity of SIMO and MISO systems presented, respectively, in equations (2.9) and (2.10). To understand this result remember that every

matrix $\mathbf{H}$ may be decomposed into singular values according to the following transformation

$$\mathbf{H} = \mathbf{U}\mathbf{D}\mathbf{V}^H \tag{2.13}$$

where **U** and **V** are unitary matrices[1] and **D** is a diagonal matrix containing the singular values of $\mathbf{H}$, which by definition are always non-negative. Therefore,

$$\mathbf{H}\mathbf{H}^H = \mathbf{U}\left(\mathbf{D}\mathbf{D}^H\right)\mathbf{U}^H = \mathbf{U}\Lambda\mathbf{U}^H \tag{2.14}$$

is easily recognized as the eigenvalue decomposition of $\mathbf{H}\mathbf{H}^H$ with $\mathbf{\Lambda}$ the diagonal matrix of its eigenvalues. Denoting $\mathbf{\Lambda} = \text{diag}\{\lambda_1, \ \lambda_2, \ \cdots \ \lambda_{Nr}\}$ and recalling the well-known relation between singular value decomposition and eigenvalue decomposition [evident in equation (2.14)] it is straightforward to conclude that the singular values of $\mathbf{H}$ may be expressed as $\mathbf{D} = \text{diag}\left\{\sqrt{\lambda_1}, \ \sqrt{\lambda_2}, \ \cdots \ \sqrt{\lambda_{Nr}}\right\}$.

Replacing equation (2.14) and $\mathbf{Q} = (\rho/Nt)\mathbf{I}_{Nt}$ in equation (2.11) we can write

$$C_{UP} = \log_2\left(\det\left(\mathbf{I}_{Nr} + \frac{\rho}{Nt}\mathbf{U}\Lambda\mathbf{U}^H\right)\right) \tag{2.15}$$

with the subscript *UP* denoting Uniform Power allocation. Note that C_{UP} is not, actually, the Shannon capacity, because if the transmitter has the CSI it can generate a signal covariance which outperforms $\mathbf{Q} = (\rho/Nt)\mathbf{I}_{Nt}$. Even so, we refer to the expression in equation (2.15) as the capacity.

Remembering that **U** is unitary and using the identity $\det(\mathbf{I}_m + \mathbf{A}\mathbf{B}) = \det(\mathbf{I}_n + \mathbf{B}\mathbf{A})$ with **A** $m \times n$ and **B** $n \times m$, equation (2.15) reduces to

$$C_{UP} = \log_2\left(\det\left(\mathbf{I}_{Nr} + \frac{\rho}{Nt}\Lambda\right)\right), \tag{2.16}$$

which can also be expressed as

$$C_{UP} = \sum_{i=1}^{Nr}\log_2\left(1 + \frac{\rho}{Nt}\lambda_i\right). \tag{2.17}$$

Comparing this result with equation (2.7) presented in section 2.2.1 for SISO channels, we verify that the MIMO channel capacity is given by the sum of capacities of *Nr* SISO independent channels, with λ_i (the squared singular values of matrix **H**) being the

[1] A $n \times n$ (square) matrix, $\mathbf{U}$, is unitary if it satisfies the condition $\mathbf{U}^H\mathbf{U} = \mathbf{U}\mathbf{U}^H = \mathbf{I}_n$. This condition implies that $\mathbf{U}$ is unitary if and only if $\mathbf{U}^{-1} = \mathbf{U}^H$.

corresponding channel gains and P_T/Nt being the corresponding transmit power. It is well-known that the number of non-zero singular values of a $Nr \times Nt$ matrix, which is called the *matrix rank*, is at the most, equal to the minimum of *Nr* and *Nt*. Thus, the use of multiple antennas at both link ends, generates a set of virtual parallel sub-channels, between the transmitter and the receiver, resulting in a linear capacity increase with $r = \min(Nr, Nt)$, i.e., the minimum number of transmit and receive antennas.

Nevertheless, the MIMO capacity given by equation (2.17), depends crucially on the number and distribution of non-zero eigenvalues of the matrix $\mathbf{HH}^H$. Obviously, if some eigenvalues are very small or zero, the system does not accomplish the expected capacity gain since the power allocated to these sub-channels cannot reach the receiver. Results presented in [8] and [9] demonstrated that the linear capacity growth is achieved for the independent and identically distributed (iid) flat Rayleigh fading channel, in which case the entries of matrix **H** follow a complex-Gaussian distribution.

With CSI at the transmitter

Consider now the case where the transmitter has information about the channel. Would this information, somehow, help to enhance the channel capacity? CSI at the transmitter may be achieved through feedback from the receiver. In this case, the individual sub-channels may be accessed using linear signal processing at the transmitter and the receiver, enabling an increase in the capacity.

Let the $r \times 1$ signal vector which will be transmitted be denoted as $\tilde{\mathbf{s}}$, with r being the rank of the channel matrix, $\mathbf{H}$. Recall the system model presented in equation (2.6) and also, the singular value decomposition presented in equation (2.13). Note that, if the channel matrix is known at the transmitter, it may compute the corresponding singular value decomposition. Then, before transmission, the signal vector $\tilde{\mathbf{s}}$ is multiplied by matrix $\mathbf{V}$ such that $\mathbf{s} = \mathbf{V}\tilde{\mathbf{s}}$ (here $\mathbf{V}$ has dimension $Nt \times r$, corresponding to the first r right singular vectors of $\mathbf{H}$). At the receiver, the received signal vector $\mathbf{y}$ is multiplied by the matrix $\mathbf{U}^H$ according with $\tilde{\mathbf{y}} = \mathbf{U}^H\mathbf{y}$ (similarly, here $\mathbf{U}$ has dimension $Nr \times r$, corresponding to the first r left singular vectors of $\mathbf{H}$) . Hence, equation (2.6) may be rewritten as[2]

$$\tilde{\mathbf{y}} = \mathbf{D}\tilde{\mathbf{s}} + \tilde{\mathbf{n}} \tag{2.18}$$

[2] Note that the channel matrix may be expressed as $\mathbf{H} = \mathbf{UDV}^H$, with $\mathbf{U}$ and $\mathbf{V}$ being matrices with dimension $Nr \times r$ and $Nt \times r$, respectively, corresponding to the first r left and right singular vectors of $\mathbf{H}$, respectively; and with $\mathbf{D}$ being a $r \times r$ diagonal matrix containing the non-zero singular values of $\mathbf{H}$. In this case $\mathbf{U}$ and $\mathbf{V}$ are not unitary matrices but $\mathbf{V}^H\mathbf{V} = \mathbf{I}_r$ and $\mathbf{U}^H\mathbf{U} = \mathbf{I}_r$ are valid.

where the transformed received vector, $\tilde{\mathbf{y}}$, and the transformed noise vector, $\tilde{\mathbf{n}} = \mathbf{U}^H \mathbf{n}$, are both $r \times 1$ vectors and $\mathbf{D}$ is a r–dimensional diagonal matrix. Equation (2.18) means that if CSI is available at the transmitter $\mathbf{H}$ may be explicitly decomposed into r parallel sub-channels, fulfilling

$$\tilde{\mathbf{y}}_i = \sqrt{\lambda_i}\,\tilde{\mathbf{s}}_i + \tilde{\mathbf{n}}_i, \quad i = 1, 2, \ldots, r \,. \tag{2.19}$$

This explicit decomposition of the channel grants to the transmitter the access to individual sub-channels, allowing the use of some power allocation scheme which aims to maximize the channel capacity. This may be achieved by adjusting, in equation (2.11), the matrix of the signal covariance given by $\mathbf{Q} = \mathrm{E}\left[\mathbf{s}\mathbf{s}^H\right] = \mathbf{V}\mathrm{E}\left[\tilde{\mathbf{s}}\tilde{\mathbf{s}}^H\right]\mathbf{V}^H$.

Consider $\mathbf{Q}_{\tilde{\mathbf{s}}} = \mathrm{E}\left[\tilde{\mathbf{s}}\tilde{\mathbf{s}}^H\right] = \mathrm{diag}\{\gamma_1, \quad \gamma_2, \quad \cdots \quad \gamma_r\}$, with $\mathrm{E}\left[\left|\tilde{s}_i\right|^2\right] = \gamma_i$. Again, to maintain the total power constrained to P_T the condition $\mathrm{tr}\left(\mathbf{Q}_{\tilde{\mathbf{s}}}\right) = \rho$ should be satisfied. Using the singular value decomposition of the channel presented in equation (2.13), equation (2.11) may now be written as

$$C_{OP} = \max_{\mathbf{Q}_{\tilde{\mathbf{s}}}:\ \mathrm{tr}(\mathbf{Q}_{\tilde{\mathbf{s}}}) \le \rho} \left\{ \log_2\left(\det\left(\mathbf{I}_r + \mathbf{\Lambda}\mathbf{Q}_{\tilde{\mathbf{s}}}\right)\right)\right\} \tag{2.20}$$

where *OP* denotes Optimum Power allocation. Alternatively,

$$C_{OP} = \sum_{i=1}^{r} \log_2\left(1 + \lambda_i\,\gamma_i\right) \tag{2.21}$$

where the condition

$$\sum_{i=1}^{r} \gamma_i = \rho \ \text{ with } \ \gamma_i \ge 0 \tag{2.22}$$

must be satisfied.

The problem that arises is to obtain the weighting coefficients, γ_i, which provide optimum power allocation and thus, maximum transmission bit rate. This problem has already been studied and the solution is the well-know "water-filling" algorithm [9, 13, 15]. It may be easily understood if we make an analogy with a set of vessels, each having a given liquid level, specified by $1/\lambda_i$ and that it is intended to fill all the vessels to a common level μ. This can be traduced mathematically by

$$\frac{1}{\lambda_1} + \gamma_1 = \frac{1}{\lambda_2} + \gamma_2 = \cdots = \frac{1}{\lambda_i} + \gamma_i = \cdots \frac{1}{\lambda_r} + \gamma_r = \mu \tag{2.23}$$

where the weighting coefficients, γ_i, fulfill the conditions in equation (2.22).

The water-filling principle is illustrated in Figure 2-2 showing that for each level $1/\lambda_i$ less than μ, the optimal power allocation consists in filling the corresponding sub-channel up to the level defined by μ. Therefore, we conclude that the best performing sub-channels (higher gain) receive more power while the worst performing channels get less power. Eventually, if $1/\lambda_i$ is greater than μ, no power will be allocated to the corresponding sub-channel.

The solution can be found iteratively as follows. First, the counter k is set to 0 (this counter indicates the number of unused sub-channels). Then the level μ is obtained taking the power constraint into account, according to

$$\mu = \frac{1}{r-k}\left(\rho + \sum_{i=1}^{r-k}\frac{1}{\lambda_i}\right). \tag{2.24}$$

Finally, the power allocated to each sub-channel is computed using

$$\gamma_i = \mu - \frac{1}{\lambda_i}, \quad i = 1,\ldots,n-k. \tag{2.25}$$

If the power allocated to the weakest channel is negative, i.e., $\gamma_{n-k} < 0$, this channel should be discarded by defining $\gamma_{n-k} = 0$ and the power allocated to the remaining channels should be updated, by running again the algorithm with the counter k incremented by 1. The procedure is iterated until the power allocated to each channel is non-negative. Evidently, as this method only considers the channels with good-quality and rejects the bad ones, it is expected that the corresponding capacity is greater than, or at least equal to, the capacity achieved without CSI at the transmitter.

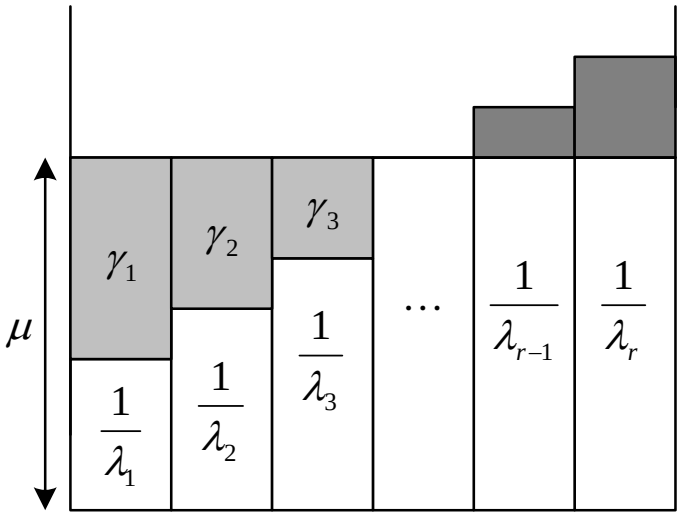

Figure 2-2: Illustration of the water-filling algorithm.

2.2.3. Stochastic Channels

MIMO capacity presented until now refers to the case of a deterministic channel or a sample channel realization. However, in general the channel matrix, **H**, is random and the corresponding capacity is a random variable where each channel realization presents an instantaneous capacity given by equation (2.17) if the channel is unknown at the transmitter, or equation (2.21) otherwise. The evaluation of the capacity offered by fading channels is usually based on two statistic quantities, namely, the ergordic capacity and the outage capacity.

Ergodic Capacity

The ergodic capacity of a MIMO channel is the ensemble average of the transmission rate over the distribution of the elements of the channel matrix, **H** [13]. It is particularly relevant when the channel is ergodic, i.e., every channel matrix is an independent realization of the same stochastic process and changes faster than the duration of a codeword (fast fading channel). In this case, any codeword experiences a large number of different channel realizations and the ergodic capacity can be viewed as the Shannon capacity of the channel since it is possible to achieve the corresponding information rate, with arbitrarily small error probability, if optimal codebooks are used.

Figure 2-3 presents the ergodic capacity as a function of the SNR for some antenna configurations, assuming an iid Rayleigh fading channel (the elements of the channel matrix follow a zero-mean and unit variance complex-Gaussian distribution) and channel unknown at the transmitter. Naturally, the ergodic capacity improves with increasing SNR. In addition, we observe that ergodic capacity improves also with increasing *Nt* and *Nr*. However, increasing *Nr* (maintaining the same *Nt*) produces a more evident boost in the capacity than increasing *Nt* (cf. curves for 1×1, 2×1, 1×2 and 2×2, 3×2, 2×3). This behavior is due to the power constraint at the transmitter and also to the inability of the transmitter to exploit the channel efficiently, since it has no CSI.

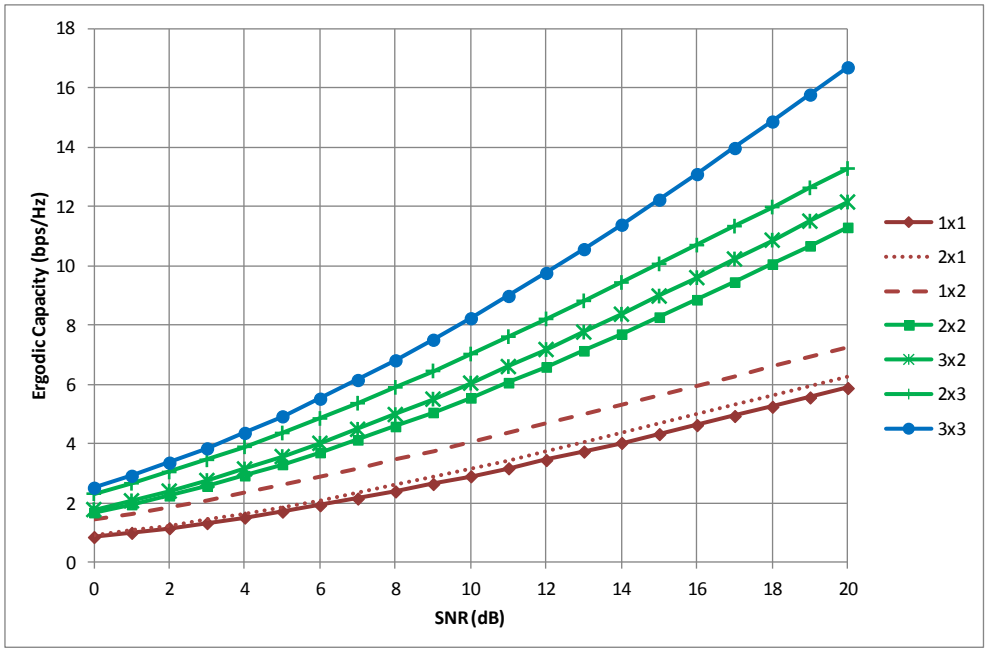

Figure 2-3: Ergodic capacity for different antenna configurations: the curves labels indicate *Nt*×*Nr*.

Outage Capacity

The outage capacity quantifies the level of capacity that is guaranteed with a given level of reliability. The q% outage capacity, $C_{out,q}$, is defined as the transmission rate that is achieved for (100-q)% of the channel realizations. As for the ergodic capacity, the outage capacity also improves with the increase in the SNR and in the number of the antennas.

Outage capacity is a useful figure for the system characterization when the channel is unknown at the transmitter and the channel matrix, although random, remains constant over the duration of a codeword (but changes independently from block to block), corresponding to a slow fading channel. In this case, for any information rate there is a certain probability that the given channel realization does not support the desired rate, resulting in packet error and consequently in the occurrence of an outage situation. Therefore, a tradeoff must be established between the desired information rate and the outage probability.

2.2.4. Frequency Selective Channels

The capacity of a frequency selective MIMO channel (i.e., a wideband channel) may be calculated by dividing the frequency band of interest into M narrower sub-bands, such that each sub-channel can be considered as frequency flat (to achieve this requirement the bandwidth of these sub-channels must be smaller than the coherence bandwidth). Capacity is then obtained by summing the capacities of these sub-channels.

Consider $\mathbf{H}_i$ (i=1, 2, …, M) as being the i-th sub-channel matrix. The input-output relation for this sub-channel is described by equation (2.6). Now, let $\boldsymbol{\mathcal{S}} = \begin{bmatrix} \mathbf{s}_1^T & \mathbf{s}_2^T & \cdots & \mathbf{s}_N^T \end{bmatrix}^T$, with dimension $Nt\,M \times 1$, and $\boldsymbol{\mathcal{Y}} = \begin{bmatrix} \mathbf{y}_1^T & \mathbf{y}_2^T & \cdots & \mathbf{y}_N^T \end{bmatrix}^T$, with dimension $Nr\,M \times 1$, be the transmitted and received signal vectors, respectively; $\boldsymbol{\mathcal{N}} = \begin{bmatrix} \mathbf{n}_1^T & \mathbf{n}_2^T & \cdots & \mathbf{n}_N^T \end{bmatrix}^T$, with dimension $Nr\,M \times 1$, be the noise vector; and the channel matrix $\boldsymbol{\mathcal{H}}$, with dimension $Nr\,M \times Nt\,M$, be a block diagonal matrix where $\mathbf{H}_i$ are the block diagonal elements. Thus, the wideband input-output relation is formally analogous to equation (2.6) and given as

$$\boldsymbol{\mathcal{Y}} = \boldsymbol{\mathcal{H}}\boldsymbol{\mathcal{S}} + \boldsymbol{\mathcal{N}}. \tag{2.26}$$

The covariance matrix of $\boldsymbol{\mathcal{S}}$, denoted as $\mathbf{Q}_{\mathcal{S}} = E\left[\boldsymbol{\mathcal{S}}\boldsymbol{\mathcal{S}}^H\right]$, satisfies $\mathrm{tr}\left(\mathbf{Q}_{\mathcal{S}}\right) = M\rho$ in order to constraint average transmit power to P_T. Form equation (2.11), the capacity of a frequency selective MIMO channels, in bps/Hz, is then given by

$$C_{FS} = \frac{1}{M} \max_{\mathbf{Q}:\mathrm{tr}(\mathbf{Q}) \le M\rho} \left\{ \log_2 \left(\det\left(\mathbf{I}_{NrM} + \boldsymbol{\mathcal{H}}\mathbf{Q}_{\mathcal{S}}\boldsymbol{\mathcal{H}}^H \right) \right) \right\}. \tag{2.27}$$

Considering the case in which the channel is unknown to the transmitter we should select $\mathbf{Q}_{\mathcal{S}} = \left(\rho / Nt\right)\mathbf{I}_{NtM}$, meaning that the transmit power is equally distributed over space (transmit antennas) and frequency. In this case, the capacity can be written as

$$C_{FS} = \frac{1}{M} \sum_{i=1}^{M} \log_2 \left(\det\left(\mathbf{I}_{Nr} + \frac{\rho}{Nt} \mathbf{H}_i \mathbf{H}_i^H \right) \right). \tag{2.28}$$

Obviously, if the entire channel response is frequency flat, i.e., $\mathbf{H}_i = \mathbf{H}$ (i=1, 2, …, M), this expression reduce to equation (2.12). In addition, if all $\mathbf{H}_i$ are iid (i.e., the bandwidth of each sub-channel is less than or equal to the coherence bandwidth), by the strong law of large numbers the capacity of a sample realization of the frequency selective channel approaches a fixed quantity as $M \to \infty$.

If the channel is random, the ergodic and outage capacity, as seen above, are helpful statistics for the channel characterization and may be defined similarly for frequency selective channels as done previously in section 2.2.3 for frequency flat channels. It is worth to mention that, the outage capacity of a frequency selective channel is higher than the outage capacity of a frequency flat channel (at low outage probabilities). This is a result of the increased tightening of the Cumulative Density Function (CDF) of capacity due to frequency diversity offered by the frequency selective channel. This effect is illustrated in Figure 2-4 showing the CDF of the information rate for a frequency selective MIMO channel ($Nt = Nr = 2$) with increasing M using a SNR of 10 dB.

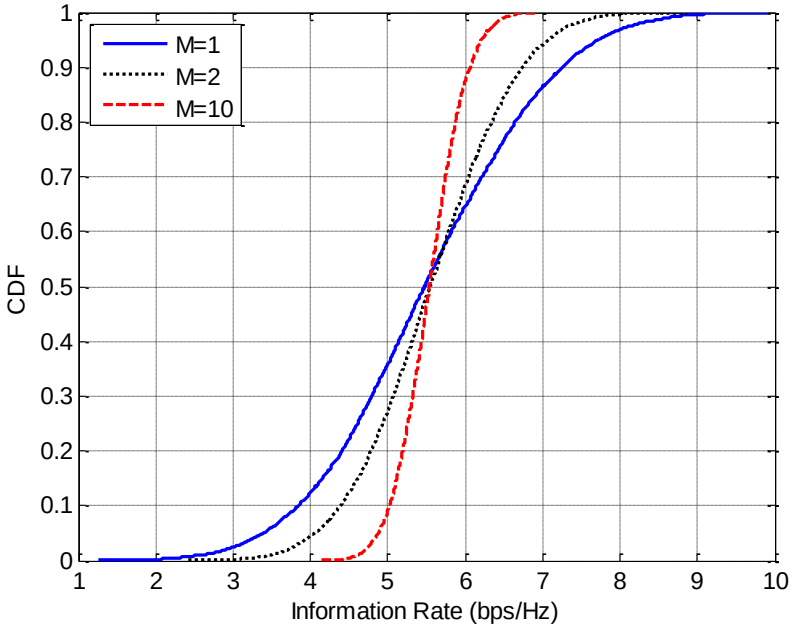

Figure 2-4: CDF of the information rate for an increasingly frequency selective MIMO channel.

As it may be observed in Figure 2-4, as the number of narrowband channels increases (*M*), the CDF tightens and therefore the outage capacity (at given outage probability) also rises. Furthermore, as the CDF tightens the outage capacity approaches to the ergodic capacity, leading us (again) to the conclusion that asymptotically (in *M*) the capacity of a sample realization of a frequency selective MIMO channel tends to the ergodic capacity.

Like in the case of the frequency flat channel, capacity of the frequency selective MIMO channel may be improved if the channel is known by the transmitter. This case may be treated using the same rationale that led to the water-filling algorithm, though here, the power has to be distributed across space and frequency in order to maximize the spectral efficiency, yielding to the space-frequency water-filling principle. Note that water-filling is applicable only to orthogonal channels. To accomplish this requirement OFDM (Orthogonal Frequency Division Multiplex) techniques are employed. The space-frequency water-filling algorithm provides the optimal power allocation, from which it can be derived the optimal space-frequency covariance matrix, $\mathbf{Q}_S$, that is constrained to $\mathrm{tr}(\mathbf{Q}_S) = M\rho$ and maximizes the channel capacity.

2.3. MIMO Potentials

It was already mentioned that the benefits of MIMO systems arise by exploiting the spatial domain which allows the system to support the use of techniques as *beamforming*, *spatial diversity* and *spatial multiplexing*. The latter can be used only in MIMO systems while the

first two, though may be used in MIMO systems, require that only one of the link ends is equipped with multiple antennas and thus may be applied as well in SIMO and MISO systems. In the following sections fundamentals of each of these techniques will be summarized.

2.3.1. Beamforming

In the last two decades beamforming (also called array gain) has been deeply studied under the scope of topics as *smart antennas* or *adaptive antennas*. In cellular environments, beamforming benefits include increased range, reduced interference and as a result increased capacity, longer mobile battery life due to reduced transmit power, reduced channel delay spread and reduced average human radio emission exposure. In MIMO systems, beamforming can be performed either at the transmitter side, the receiver side or both. However, the employment of this technique at the transmitter requires that it has CSI (it assumed that the receiver has always perfect CSI).

Beamforming enables to focus transmit or receive power into (a) certain angular direction(s) [6, 7] by choosing appropriate antenna weights. Thereby, the radiation pattern of the antenna array may be modified to enhance the quality of signals departing or arriving from the desired direction(s). Some of these techniques, particularly in the presence of interference, attempt at the same time, to create a minimum for non-desired directions like those from where the interfering signals arrive. This kind of beamforming is usually called as *spatial filtering for interference reduction* (SFIR) but, with more complex signal processing, each mobile in a cell can be extracted and simultaneously, interference can be canceled, yielding a scheme known as *space division multiple access* (SDMA).

Given that beamforming techniques aim to focus the signal power into a well-defined direction (or directions), it will perform better the more directive the channel is. The highest beamforming gain will be achieved for the most directive MIMO channel presenting one strong Direction of Departure (DoD) and one Direction of Arrival (DoA) only, such is the case under Line-of-Sight (LoS) conditions. One should note that the more directive the channel is, the more correlated are the signals from the several antennas available (spatial correlation).

2.3.2. Spatial Diversity

It is well known that the radio communications are strongly affected by fading, which is mainly generated by multipath propagation and causes fluctuations of the signal level not only across time, but also across space and frequency. This phenomenon impacts the

performance of any wireless system in terms of symbol or bit error rate. Fading is usually combated by employing diversity techniques.

The principle of any diversity scheme is to provide the receiver with multiple versions (branches) of the same transmitted signal. If these versions are affected by independent fading conditions, the probability that all branches are in a deep fade at the same time reduces dramatically. Therefore, diversity increases the reliability of the radio link and leads to improved system performance in terms of error rate.

As fading can occur in time, frequency and space domains, diversity techniques may correspondingly be developed in each of these domains. Nevertheless, both time and frequency diversity schemes involve a loss in time or bandwidth to allow the introduction of redundancy in the signal. On the contrary, spatial (and also polarization) diversity does not sacrifice time and bandwidth as it is provided by the use of multiple antennas at one or both sides of the link. However, the system spatial dimension, complexity and also cost are increased by using antenna arrays.

Obviously, the performance of spatial diversity is highly dependent on the signals (branches) correlation which under ideal conditions should not exist if the branches experience independent fades. Hence, contrasting with beamforming, spatial diversity performs better when the channel is non-directive, i.e., channels which do not present dominant multipath components (MPCs), as strong LoS component for instance.

In receive spatial diversity [16], the receiver combines the signals from the available antennas so the resulting signal presents considerably reduced amplitude fluctuations in comparison with the signal at any individual antenna. Several studies have shown that a separation of about one wavelength between the antennas suffices to provide signal branches significantly uncorrelated.

Transmit spatial diversity may be achieved either with or without CSI at the transmitter. Yet, suitable design of the transmitted signal is required to obtain the potential diversity gains. In this context many contributions have emerged of which [5, 17-19] are referred.

In MIMO systems spatial diversity can be exploited at both link ends, so the global system performance is improved and requires a combination of receive and transmit diversities presented above.

2.3.3. Spatial Multiplexing

Spatial multiplexing is only possible in MIMO systems and offers a linear increase in the transmission rate (with increasing minimum number of transmit/receive antennas) without requiring more bandwidth or transmit power. It exploits the different spatial signatures existing between each transmit-receive antenna pair, which, under favorable channel conditions, are well separated. Thereby, the bit stream to be transmitted may be split into several (*Nt* at the most) sub-streams, modulated and transmitted simultaneously from each transmit antenna. The receiver, having complete knowledge of the channel (matrix **H**), distinguishes between several sub-channels and recovers these signals, which after demodulation yield the corresponding sub-streams to be combined, so the original bit stream is reconstructed.

In a simple rationale, the problem is similar to the resolution of a system of linear equations. Actually, one decoding method commonly used is the zero-forcing technique which consists in inverting directly the channel matrix, **H**, though a simple approach it can result in poor results when the matrix is ill-conditioned. Alternatively, a receiver using maximum likelihood detector compares all possible combinations of symbols which could have been transmitted with what is observed and selects the most probable solution. This technique presents optimum performance but also high complexity which may be prohibitive. Evidently, the perfect recovery of the several transmitted sub-streams (so the original signal is also recovered) requires the equations composing the system to be independent meaning that each antenna sees an independent channel (or at least sufficiently different).

Similarly to spatial diversity and contrasting to beamforming, spatial multiplexing performs better when the signals at receiving antennas are independent such as non-directive channels exhibiting numerous MPCs. Nevertheless, unlike spatial diversity, that attempts to improve the signal quality fighting the multipath phenomenon, spatial multiplexing exploits efficiently this phenomenon in order to increase the transmission rate. A well-known algorithm that implements spatial multiplexing is the V-BLAST (*Vertical – Bell Labs Layered Space Time*) [20].

2.3.4. Transmission over MIMO systems

The analysis presented in section 2.2, based on information theory, is useful as it motivates the research for technologies and architectures to benefit from gains promised by MIMO systems when compared to conventional systems. Although, it should be noted that this analysis only provides an upper bound without any limitation of complexity, and thus does

not reflects the performance achieved by a given transmission system. In fact, in the development of any algorithm or architecture, it is necessary to establish a compromise between a given performance measure and an acceptable level of complexity. On the other hand, as seen above, the specific channel conditions may dictate which of the techniques presented in the last sections (2.3.1, 2.3.2 and 2.3.3) will perform better.

If both, transmit and receive sides are sufficiently non-directive both, spatial diversity (at transmitter and receiver) and spatial multiplexing, may be used. In this case the system requirements (desired data rate, reliability of transmission, etc.) will establish optimum tradeoff between these two techniques. In general, transmission schemes over MIMO channels typically fall into two categories: data rate maximization or diversity maximization. The first class of these techniques intends to improve the average capacity, but in general, individual streams should be encoded jointly in order to protect the transmitted signal against errors induced by channel fading and noise/interference. This brings in a second approach in which one attempts, as well, to minimize the outage probability, or equivalently, to maximize the outage capacity by introducing diversity. One should note that the level of redundancy may be so high that it does not provide any capacity improvement. In such case, the multiple antennas allows for spatial diversity but not for the data rate increase (at least in a direct manner).

The set of techniques and algorithms used to encode jointly the signals for the multiple transmit antennas are referred as *space-time codes* (STCs). Generally, these techniques consist in generating and transmitting simultaneously a number of code symbols equal to the number of transmit antennas (one symbol is transmitted from each antenna). Symbols are generated by the space-time encoder such that by using suitable signal processing and decoding procedures at the receiver, the desired diversity and/or coding gains are achieved.

The first schemes to develop STCs that emerged [18] were based on trellis codes, which required a multidimensional Viterbi algorithm at the receiver for signal decoding. Besides the coding gain that depends on the code complexity, these codes offer also a diversity gain without any loss in the bandwidth efficiency. However, in terms of complexity these techniques are very demanding which may not be reasonable for most systems.

The popularity of STCs truly increased when *space-time block codes* (STBCs) emerged, mainly because for these codes it is possible to perform decoding using simple linear processing at the receiver. However, STBCs only provide diversity gain without any coding gain. Nevertheless, due to its simplicity when compared to trellis codes, they have attracted much attention overcoming the latter. In this context, it should be noted that this technology had its genesis on the scheme proposed by Alamouti [17] for transmitters with

two antennas. The Alamouti scheme revealed to be so attractive that it was included in W-CDMA and CDMA-2000 standards. Later, it has been generalized to an arbitrary number of antennas [19]. A detailed review of STC techniques can be found in [21].

Spatial multiplexing, presented in section 2.3.3, can be seen as a special case of STBCs where streams of independent data are transmitted over different antennas enabling to maximize the average data rate over the MIMO system. Even though, it allows the independent usage of the antennas, it offers limited diversity benefits and will hardly meet the requirements for a desired bit error rate. Alternatively, using STC may result in additional coding gain and diversity gain [22] which may help to improve system performance, even if the data rate is kept at the same level. It is also possible to sacrifice some data rate for more diversity gain. On the other hand, introducing diversity will contribute to increase indirectly the data rate given the improved error performance may allow the usage of higher level modulations. Studies presented in [23, 24] discuss some tradeoffs between diversity and spatial multiplexing.

2.4. MIMO Channel Models

The evolution of wireless communications led to the enhancement of early SISO propagation models, which provided information about power, in order to consider time and frequency variations information. Later, when space diversity and smart antennas techniques emerged spatial information was also considered and directional channel models came into the scene. MIMO systems have pushed further the evolution of propagation modeling toward more complex spatial-temporal considerations. This section is extensively based on the content of [25] and also of chapter 2 from [26].

2.4.1. Brief review of propagation mechanisms

In any wireless communication system, signals arrive at the receiver via various propagation mechanisms. The existence of several MPCs with different time delays, DoDs, DoAs, phases and attenuation yield a highly complex transmission channel. The propagation mechanisms may be classified into five basic phenomena:

i. Free-space or line-of-sight (LoS) propagation;
ii. Transmission (and absorption);
iii. Specular reflection;
iv. Diffraction;
v. Diffusion or diffuse scattering.

Any combination of these mechanisms may contribute to the received signal and except for LoS, all them involve the interaction of the propagating wave with one or more obstacles – walls, trees, cars, human beings, etc – which are usually referred as scatterers or interacting objects. The LoS path experiences free-space loss only. Transmission through an obstacle also causes partial absorption of energy. Specular reflection occurs when a propagating electromagnetic wave impinges upon a plane and smooth surface whose dimensions are much larger than the wavelength. Diffraction happens when the path between the transmitter and the receiver is obstructed by a discontinuity, such as an edge, wedge or cylinder. Finally, diffusion is caused by interactions of the wave with objects whose dimensions are on the same order of the wavelength as rough objects. In this case, the resulting wave is most often non-coherent: its phase is not deterministic and therefore is only characterized in a stochastic manner.

The term channel is usually employed to describe the impulse response of the linear time-variant communication system between the transmitter and the receiver. Concerning SISO channels, a complete model for the impulse response may be expressed as the product of three factors:

- Path-loss: a real-valued attenuation factor depending on the distance between the transmitter and the receiver (also called the range) and on the so-called path-loss exponent;
- Shadowing: an additional random real-valued attenuation factor which, for a given range, depends on the specific location of the transmitter and the receiver; it is usually modeled by a lognormal variable;
- Fading: a complex variable representing the signal fluctuations caused by the combination of non-coherent MPCs.

A number of models for path-loss and shadowing have been proposed [16, 27] and their application is identical either for single or multi-antenna systems. This thesis is thus focused on MIMO fading models.

2.4.2. The double-directional channel impulse response

In MIMO systems, the transmitter and the receiver are both equipped with antenna arrays. The fading channel between each transmit-receive antenna pair may be described as SISO channel. However, modeling only individual SISO channels does not characterize completely the behavior of the MIMO channel. The model must include also the statistical correlations between the elements of the channel matrix.

As already referred, when dealing with MIMO channels space comes as an additional dimension and needs to be modeled on its own in the same way as time and frequency characteristics have been modeled for wideband SISO channels. For example, the angular distribution of energy should be described at both link ends. This leads to the so-called *double-directional* description of the channel: the term directional means that the channel model includes a description of the angular distribution of the energy at the antennas (contrasting to a non-directional model, which deals only with temporal spreading); the term double indicates that the spatial description of the channel concerns the transmitter and receiver sides.

The double-directional channel impulse response, between a transmitter located at $\mathbf{r}_{tx}$ and a receiver located at $\mathbf{r}_{rx}$, is usually given as the sum of contributions of L individual MPCs, expressed as [28]:

$$h\left(\mathbf{r}_{tx},\mathbf{r}_{rx},\tau,\mathbf{\Omega}_{tx},\mathbf{\Omega}_{rx}\right)=\sum_{\ell=1}^{L}h_{\ell}\left(\mathbf{r}_{tx},\mathbf{r}_{rx},\tau,\mathbf{\Omega}_{tx},\mathbf{\Omega}_{rx}\right), \tag{2.29}$$

where τ is the excess delay, $\mathbf{\Omega}_{tx}$ and $\mathbf{\Omega}_{rx}$ are respectively, the DoD and the DoA in 3-D space. The contribution of the ℓ-th MPC is written as

$$h_{\ell}\left(\mathbf{r}_{tx},\mathbf{r}_{rx},\tau,\mathbf{\Omega}_{tx},\mathbf{\Omega}_{rx}\right)=\alpha_{\ell}\delta\left(\tau-\tau_{\ell}\right)\delta\left(\mathbf{\Omega}_{tx}-\mathbf{\Omega}_{tx,\ell}\right)\delta\left(\mathbf{\Omega}_{rx}-\mathbf{\Omega}_{rx,\ell}\right), \tag{2.30}$$

where α_{ℓ} represents the complex amplitude, $\delta(\bullet)$ is Dirac delta function.

When the transmitter and/or the receiver and/or scatterers are moving, the values of τ, $\mathbf{\Omega}_{tx}$ and $\mathbf{\Omega}_{rx}$ are time-variant. A compact notation for the time-variant double-directional channel is given as

$$h\left(t,\tau,\mathbf{\Omega}_{tx},\mathbf{\Omega}_{rx}\right)=\sum_{\ell=1}^{L}h_{\ell}\left(t,\tau,\mathbf{\Omega}_{tx},\mathbf{\Omega}_{rx}\right) \tag{2.31}$$

where all temporal variations were grouped into a unique dependence under the variable t. For this reason $\mathbf{r}_{tx}$ and $\mathbf{r}_{rx}$ were dropped for simplicity. $h_{\ell}\left(t,\tau,\mathbf{\Omega}_{tx},\mathbf{\Omega}_{rx}\right)$ is defined similarly as in equation (2.30).

The double-directional impulse response, now introduced, describes directly the physical propagation channel, whereas the MIMO channel matrix presented in equation (2.1) characterizes the response between all transmit-receive antenna pairs. Yet, the relationship between both points of view is straightforward and the impulse response between the j-th transmitting antenna and the i-th receiving antenna, $h_{i,j}(t,\tau)$, is written as

$$h_{i,j}(t,\tau) = \iint h_{i,j}(t,\tau,\mathbf{\Omega}_{tx},\mathbf{\Omega}_{rx})\, d\mathbf{\Omega}_{tx} d\mathbf{\Omega}_{rx} = \iint h\left(t,\mathbf{r}_{tx}^{j},\mathbf{r}_{rx}^{i},\tau,\mathbf{\Omega}_{tx},\mathbf{\Omega}_{rx}\right) d\mathbf{\Omega}_{tx} d\mathbf{\Omega}_{rx} \,. \qquad (2.32)$$

2.4.3. Model Classification

Literature provides a variety of channel models, many of them based on measurements. These models may be categorized in several ways: *narrowband* (flat fading) or *wideband* (frequency-selective) models; *time-invariant* or *time-variant* models; *deterministic* or *empirical* models. Narrowband MIMO channels can be completely described by characterizing their spatial structure. However, wideband channels additionally require the modeling of the multipath channel properties. For time-varying channels it is furthermore necessary to describe the temporal evolution of the channel.

An alternative categorization of the models may be made by distinguishing *physical models* and *analytical models*. Physical models represent the MIMO channel by characterizing the double-directional multipath propagation between the transmitter and the receiver. These models explicitly describe parameters as complex amplitude, DoD, DoA and delay for the MPCs present in the channel. On the other hand, analytical channel models describe the impulse response (or alternatively, the transfer function) between individual transmit-receive antenna pairs by a mathematical (or analytical) expression, without explicitly take into account the wave propagation. The individual impulse responses are collected in the MIMO channel matrix introduced in equation (2.1). Analytical models are widely used for the synthesis of MIMO matrices in the framework of system and algorithm development and verification. The relationship between physical and analytical models is the same as the one defined by equation (2.32) between wave propagation and the MIMO channel matrix. Notice that a physical model may be easily converted into an analytical model but not the opposite.

Physical models may be additionally classified as *deterministic models*, *geometry-based stochastic models* or *empirical stochastic models*. These subclasses of physical models will be presented with more detail in subsections, 2.4.4, 2.4.5 and 2.4.6, respectively. Analytical models may also be further categorized as *propagation-motivated models* or *correlation-based models*. Propagation-motivated models treat the channel matrix by modeling propagation parameters. Examples of this kind are the virtual channel representation [29], the finite scatterer model [30] and the maximum entropy model [31]. On the other hand, correlation-based models describe the MIMO channel matrix in terms of the correlations between the matrix entries. The well-know Kronecker model [32] is one example of correlation-based models as well as the Weichselberger model [33].

At last, one should also mention *standardized models*. These are reference models which were established by several international organizations in order to compare different MIMO systems under the same channel conditions. Examples of standardized models will be presented in section 2.4.7.

2.4.4. Ray-based deterministic models

Ray tracing is a method based on Geometrical Optics (GO) which has been extensively applied to the mobile terrestrial channel. In fact, if the wavelength is small compared to the size of obstacles, each contribution may be regarded as a narrow beam, generally called ray. The problem consists in calculating the electric field at the receiver, in amplitude, phase and polarization. This field, expressed by a 3-D complex vector, is obtained from the combination of the direct component with several contributions, each resulting from the interaction of the transmitted signal with the surrounding environment.

Nevertheless, in general ray tracing techniques consider only four types of contributions: LoS, components transmitted through obstacles and components due to single or multiple reflections and diffractions. Components due to a combination of these four mechanisms may also be considered. However, ray tracing techniques usually do not handle diffuse scattering since this contribution is non-coherent as its phase is non-deterministic (the wavelength is not small compared to the size or roughness of obstacles).

The application of ray tracing methods to a given propagation problem requires that the given scenario is decomposed into simple geometrical configurations for which the reflection, transmission and diffraction coefficients can be calculated. All rays contributing significantly to the channel description, at an examined position, must be traced and the complex impulse response of the channel is then obtained by adding all these significant contributions in a very similar way as in equation (2.29). The received signal is thus composed by a set of delayed impulses (rays) each corresponding to an attenuated and phase shifted version of the original transmitted impulse. Although ray tracing was introduced in propagation long before the emergence of multi-antenna systems, they are inherently multidimensional. The MIMO channel matrix is then obtained using equation (2.32).

However, the accuracy of ray tracing tools is deeply dependent on:

- the availability of up-to-date and high-resolution databases which describe the propagation scenario;
- the accurate knowledge of electrical parameters for all objects in the scenario (permittivity, conductivity, loss tangent and roughness);

- the efficiency of the computational methods that are required to trace all paths between the transmitter and the receiver, in an reasonable simulation time, with enough resolution and for a sufficient order of reflections and diffractions.

2.4.5. Geometry-based stochastic models

All geometry-based models are specified by the locations of the scatterers. In deterministic geometrical methods, as ray tracing discussed above, the scatterers locations are defined in a database (arising from a rigorous scenario description). In contrast to ray tracing, Geometry-based Stochastic Channel Models (GSCM) assume that scatterers are randomly placed in a region according to a spatial scatterer density function. The channel impulse response is then obtained using a simplified ray tracing method.

GSCM were originally developed for channel simulation in SIMO systems in order to perform considerations either about diversity or smart antennas techniques. The precursor of GSCM presented by Lee in [34] placed scatterers deterministically over a circumference (evenly spaced to be precise) around the mobile station and assumed: a random phase for each scatterer (uniformly distributed); there is no LoS path and only single-bounce scattering occurs. The radius of the circumference where the scatterers are placed may be specified by the desired delay spread. Years later, some groups almost simultaneously proposed to expand this model by using randomly placed scatterers [35] (or [36]), [37-40] and the GSCM concept was created. Although, all of these models, just referred, were proposed for SIMO systems, they can be easily adapted for MIMO systems. Nevertheless, there are a number of GSCM models proposed more recently, already in the context of MIMO systems as [41-44].

GSCMs present some important advantages:

- there is a direct relation to the physical reality since essential parameters (as scatterers locations) may be frequently defined by a geometrical analysis;
- several channel effects are implicitly reproduced as small-scale fading which is created by the superposition of MPCs from individual scatterers; DoA and delay drifts due to the mobile station movement are also implicitly included;
- all information is inherent to the scatterers distribution, thus, dependencies of power delay profile or angular power spectrum do not conduct to a complication of the model;
- effects as the movement of the transmitter, receiver or scatterers and shadowing may be easily included allowing to characterize long-term channel correlations in a straightforward manner.

The random placement of scatterers reflects the physical reality much better. In addition, under the single-bounce scattering assumption the ray tracing process becomes particularly simple: except for the LoS component, all the others are formed by two sub-paths connecting the scatterer to the transmitter and to the receiver, respectively. These two sub-paths, completely characterize, for each MPC, the DoD, DoA, propagation time and complex amplitude (attenuation may be defined according to some power decay law and phase is obtained from the total path length and from the scatterer interaction which introduces a random phase shift).

Even so, for MIMO systems the single-bounce scattering may be restrictive since for a given scatterer, only two parameters among delay, DoD and DoA may be chosen independently (e.g. if DoA and delay are freely selected then DoD will be defined by these two parameters). Nevertheless, many environments reveal multiple-bounce scattering by presenting DoD, DoA and delay, totally uncoupled. Still, in this case, single-bounce scattering is well suited if the directional channel properties must be described for one link end only (as SIMO systems) by using the equivalent scatterer concept (see Figure 2-5). Equivalent scatterers are selected such that they reproduce conveniently multiple-bounce contributions in terms of delay and DoA [45]. In MIMO systems, the equivalent scatterer concept fails because the angular channel properties are described correctly only for one link end. In order to overcome this deficiency multiple-scattering has been included in several existing models as [42-44].

Different versions of GSCMs essentially differ in the proposed scatterer distributions. The simplest GSCM is achieved by assuming that the spatial distribution of scatterers is uniform. Far scatterers contribute with less power as the corresponding MPCs propagate over longer distances and thus arrive more attenuated. However, the presence of far scatters is important as it allows including important propagations effects that lead to increased temporal and angular dispersion.

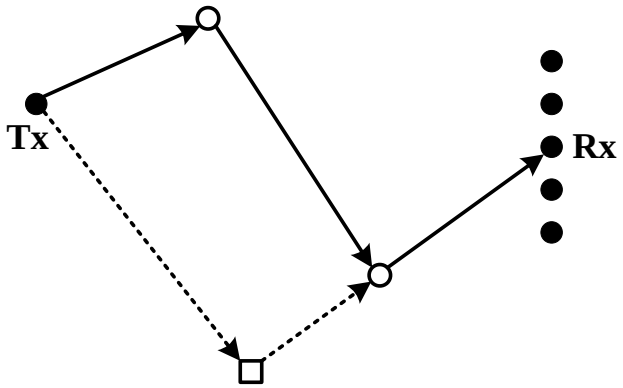

Figure 2-5: Equivalent scatterer (□) concept (true scatterers are represent by ○).

If an outlook is given to the available literature, we may find scatterers randomly placed on:

- one ring around the mobile station [41]; in this MIMO model there is no LoS component and only single-scattering is considered; it represents Rayleigh fading channels and it is valid when the base station is elevated, thus not obstructed by local scatterers; [46] also for MIMO systems, places scatterers on a ring around the mobile station but this model is intended to represent Rice fading situations so a LoS component is considered;
- an arrangement of rings and ellipses as suggested for the MIMO model presented in [42]; under the assumption that scattering mechanisms in macro-cellular scenarios generally consist in two-dimensional processes, scatterers producing components with identical delays are located on ellipses (with the corresponding foci being the transmitter and receiver positions), thus a tapped delay line may be conveniently described by a set of ellipses; however the model includes also a ring of scatterers around the mobile station and a circular area free of scatterers around the base station, the idea is to reproduce the angle-spreads differences seen at both link ends (unlike the base station, which is usually elevated, the mobile station is affected by a larger number of scatters due to its lower height); this model features multiple-bounce scattering;
- inside a circular area around the mobile station as in SIMO models presented in [35] and [40]; these models are intended to describe the uplink in large cell environments where all MPCs lie within a small angular spread; the appropriate radius of the circular scattering area depend on type of environment (urban, dense urban, etc.) and may be parameterized based on measurements; in these models only single-scattering is considered;
- inside an elliptical area whose foci correspond to the transmitter and receiver positions, as proposed in [37]; this single-bounce SIMO model has been developed for microcellular environments, provided that in such environments the antennas heights are both relatively low, and thus, multipath is generated from both link ends; the ellipse size is defined by the maximum excess delay; in [38] a similar approach is presented but here the ellipse is subdivided into several elliptical subregions and inside each subregion are placed a number of scatterers which is given by a Poisson process;
- an arrangement of locations able to reproduce the double-directional characteristics of the channel as proposed by the COST 273 [44] model; it includes local clusters around the transmitter and/or the receiver (with a large angle spread), randomly

placed single-bounce clusters and twin-clusters for multiple-bounce; for single-bounce clusters DoD, DoA and delay are obtained by means of geometrical relationships; multiple-bounce is achieved using the twin-clusters concept where each physical cluster is split into two clusters, one related to the transmitter side, the other related to the receiver side, allowing to model the angular dispersion independently at each link end, so there is no geometrical relationship between DoD, DoA and delay.

2.4.6. Empirical stochastic models

Empirical (or non-geometrical) stochastic models characterize MPCs from transmitter to receiver using statistical parameters only, not considering the geometry of the physical environment. These models are usually based on experimental results and generalize the tap-delay-line concept. MPCs may be treated individually or found to arrive in clusters.

Extended Saleh-Valenzuela model

Saleh and Valenzuela proposed a non-directional propagation model for indoor scenarios [47]. This model is based on measurements which showed MPCs arriving in clusters and also on the tap-delay-line approach. Therefore, the Saleh and Valenzuela (SV) model assumes clusters in the delay domain that are described using a double exponential decay process: one is used to control the power of a multipath cluster and another, presenting a more abrupt slope, is used to describe MPCs within the individual clusters.

In [48, 49] it is further observed that clustering is also present in the angular domain. Thus, the SV model has been extended in order to include also a directional description of the channel, resulting in the following channel impulse response model: [49]

$$h(t,\tau,\phi_{tx},\phi_{rx}) = \sum_{k=1}^{K}\sum_{\ell=1}^{L}\alpha_{k\ell}\,\delta(\tau - T_k - \tau_{k\ell})\,\delta(\phi_{tx} - \Phi_{tx,k} - \phi_{tx,k\ell})\,\delta(\phi_{rx} - \Phi_{rx,k} - \phi_{rx,k\ell}) \qquad (2.33)$$

where T_k, $\Phi_{tx,k}$ and $\Phi_{rx,k}$ are, respectively, the time delay, DoD and DoA of the *k*-th cluster, while $\tau_{k\ell}$, $\phi_{tx,k\ell}$ and $\phi_{rx,k\ell}$ are the relative delay, DoD and DoA of the ℓ-th MPC within the *k*-th cluster.

The MPCs amplitudes, $\alpha_{k\ell}$, are complex Gaussian variables whose mean power (relative to the first MPC) is given by

$$E\left[\left|\alpha_{k\ell}\right|^2\right] = E\left[\left|\alpha_{00}\right|^2\right]\exp\left(-\frac{T_k}{\Gamma}\right)\exp\left(-\frac{\tau_{k\ell}}{\gamma}\right), \tag{2.34}$$

where Γ and γ are power-delay time constants, respectively, for clusters and MPCs within the clusters. This double-exponential decay is illustrated in Figure 2-6.

Variables T_k and $\tau_{k\ell}$ are characterized by independent inter-arrival probability density functions as follows

$$p\left(T_k \mid T_{k-1}\right) = \Lambda\exp\left[-\Lambda\left(T_k - T_{k-1}\right)\right], \tag{2.35}$$

$$p\left(\tau_{k\ell} \mid \tau_{k(\ell-1)}\right) = \lambda\exp\left[-\lambda\left(\tau_{k\ell} - \tau_{k(\ell-1)}\right)\right], \tag{2.36}$$

where, by definition, $T_1 = 0$ and $\tau_{k0} = 0$.

The angular variables, $\Phi_{tx,k}$ and $\Phi_{rx,k}$, are described as uniformly distributed, whereas the relative angles, $\phi_{tx,k\ell}$ and $\phi_{rx,k\ell}$, were experimentally found to follow a Laplace distribution expressed as

$$p\left(\phi_{k\ell}\right) = \frac{1}{\sqrt{2}\sigma_\phi}\exp\left[-\left|\frac{\sqrt{2}\phi_{k\ell}}{\sigma_\phi}\right|\right], \tag{2.37}$$

with σ_ϕ being the angular standard deviation.

Zwick model

In [50] it is stated that for indoor channels clustering does not take place if measurements are performed with a high bandwidth. Therefore, in this stochastic model for indoor environments MPCs are generated individually. A SISO model is applied, using a marked Poisson process for the appearance and the disappearance of non-LoS MPCs. The DoD and DoA are modeled with a Laplace distribution that migrates to a uniform distribution for larger delay times. The model explicitly includes a LoS signal component by modeling the transitions between LoS and obstructed LoS environments applying a Markov process. The SISO model is extended to a MIMO model by applying the plane wave assumption.

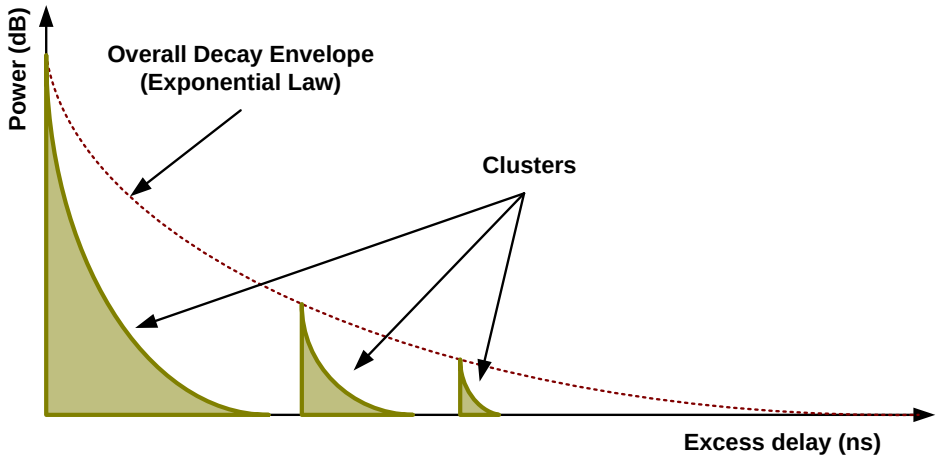

Figure 2-6: Exponential decay of the mean amplitude for clusters and for MPCs within clusters.

2.4.7. Standardized models

In this section it is presented a brief review of some reference models for MIMO systems. As referred, these models are appropriate for comparing different system implementations. However, several of these models do not help to understand the MIMO propagation concepts.

3GPP/3GPP2 Spatial Channel Model

The Spatial Channel Model (SCM) [51] (or [52]) was created by the third-generation partnership project (3GPP and 3GPP2) for outdoor environments and a system bandwidth of 5 MHz at carrier frequency of 2 GHz. The SCM comprises a *link-level* model and a *system-level* model.

The *link-level* model (also known as *calibration model*) is a simplified channel model which is intended for different equipment manufacturers to compare their implementations of the same signal processing algorithms. Comparing the performance of a given algorithm in the calibration model allows concluding, in a straightforward manner, if two implementations are equivalent. However, link-level simulations are not recommended for performance evaluation of different algorithms as they reflect only a single snapshot of the dynamic channel and thus, not allow assessing the general behavior of the system. If this kind of assessment is needed, then system-level simulations should be made.

The link-level SCM may be implemented as a physical model or as an analytical model. The former is a non-geometrical stochastic model which describes the wideband characteristics of the channel using a tapped delay line. Each tap is independently faded

and is characterized by an azimuth power spectrum, assumed to follow a uniform distribution at the mobile station and a Laplace distribution at the base station. The mean direction and angular spread at both link ends are fixed and so the model describes stationary channel conditions. The Doppler spectrum is implicitly accounted for by defining the trajectory and the velocity of the mobile station. The physical model may be converted into an equivalent analytical model by specifying the number and configuration of antennas at the transmitter and the receiver.

The *system-level* model [53] (also referred as *simulation model*) is proposed for performance assessment typically involving multiple links (multiple cells, sectors, base and mobile stations) where each link involves a mobile station and a base station. The system-level SCM is a physical model comprising three different environments: urban macro-cell, suburban macro-cell and urban-cell. The modeling and simulation methodologies are identical for the three environments, but the parameters as delay spread, azimuth spread, shadowing and path loss, are different.

Multipath propagation is assumed and the number of taps with different delays is 6. However, their delay and average power are randomly chosen from a probability density function. Each tap shows angular dispersion at both sides (base station and mobile station) which is introduced by means of describing each tap as a number of sub-paths that have all the same delay, but different DoA and DoD. Physically, this means that each tap corresponds to a cluster with 20 scatterers with the same time of arrival, but slightly different directions. Antenna radiation patterns and geometries may be chosen arbitrarily and when this is done analytical formulations can be extracted from the physical model.

The model also includes some optional features as: a polarization model; far scatterer clusters; LoS component for the micro-cell environment; and a modified angular distribution at the mobile station aiming to describe the propagation in urban street canyons.

IEEE 802.11 TGn models

The TGn channel model of IEEE 802.11 [54] is an enhanced and standardized version of the Saleh-Valenzuela model. The model conception was based on measurements and it has been planned for indoor MIMO wireless LANs in the 2 GHz and 5 GHz bands, for bandwidths up to 100 MHz.

The IEEE 802.11 TGn channel model defines a set of six environments, covering flat fading, residential, small office, typical office, large office and large open spaces. The directional impulse response is defined as a sum of clusters which overlap in the time

domain. For each environment the TGn model indicates a set of representative parameters: the number of clusters, values of DoD, DoA and cluster angular spreads (seen from transmitter and receiver) are fixed for each cluster of the different environments. Usually, each cluster consists up to 18 delay taps (separated at least by 10 ns), the number of clusters varies from 2 to 6 and the power angular profile of each cluster is described using a Laplace distribution (as in the Saleh-Valenzuela model) with angular spread in the range of 20º to 40º. Overall power angular profiles, at the transmitter and the receiver, are assumed to be statistically independent and are then computed separately at each side using the array geometry. The channel correlation matrix is subsequently obtained based on the Kronecker model. Global delay spread varies between 0 ns (corresponding to flat fading) and 150 ns.

IEEE 802.16 models

IEEE working group 802.16 has been central to the development of technical standards for fixed wireless access networks. Broadband wireless access (BWA) technology provides last mile access for high-speed residential and commercial Internet services. It is a promising alternative to digital subscriber line, cable and fiber technologies which are struggling to meet world-wide demand, especially outside metropolitan centers, for Internet services at reasonable cost. The IEEE 802.16 standard for BWA and its associated industry consortium, the WiMAX forum, has the potential to offer broadband access to virtually all users irrespective of location. WiMAX (the Worldwide Interoperability for Microwave Access) is a consortium of telecommunication equipment manufacturers, vendors and service providers, formed to promote the compatibility and interoperability of BWA devices incorporating the IEEE 802.16 and ETSI HiperMAN wireless standards.

IEEE 802.16 was designed for LoS links operating at carrier frequencies between 10 GHz and 66 GHz. The first release of the standard (IEEE 802.16-2001) specifies a set of medium access control (MAC) and physical-layer standards intended to provide fixed broadband access using a point-to-point (PP) or point-to-multipoint (PMP) topology. The standard was revised in January 2003 to include non-LoS links operating at frequencies in both licensed and unlicensed bands between 2 GHz and 11 GHz. A consolidated standard, IEEE 802.16-2004, was issued in 2004. IEEE 802.16e-2005, was issued in December 2005 which includes enhancements for physical and MAC layers that support nomadic and mobile operation in 2 to 11 GHz range. Two channel models are used for fixed and portable systems complying with the IEEE 802.16 standard. The Stanford University Interim (SUI) channel model [55] is used for fixed broadband access and the ITU Tapped-Delay-Line channel model [56] is used for portable broadband access.

The WiMAX forum approved the mobile WiMAX system profile in 2006. Mobile WiMAX, based on 802.16e-2005, enables WiMAX systems to address portable and mobile devices in addition to fixed and nomadic applications. The WiMAX forum Mobile release 1.0 channel model [56] defines the SISO and MIMO channel model requirements for mobile applications governed by the IEEE 802.16e standard. The purpose of the model is to provide a realistic and repeatable channel context for the testing and comparison of portable and mobile WiMAX-enabled devices.

WINNER channel models

The European WINNER (Wireless World Initiative New Radio) project started in 2004 with the purpose of developing an innovative radio access concept, for beyond third generation (B3G) wireless systems. Work Package 5 (WP5) of WINNER project focused on MIMO channel modeling for bandwidths up to 100 MHz and carrier frequencies between 2 and 6 GHz.

In the first stage of the project and due to immediate simulation needs, two existing channel models were selected as starting points: the 3GPP/3GPP2 SCM was selected for outdoor simulation and the IEEE 802.11 TGn model was selected for indoor simulation. As the SCM model had insufficient bandwidth and limited applicability range, in 2005 the SCM was extended to the SCM-Extended (SCME) [57] as follows: the bandwidth was extended for 100 MHz by introducing an intra-cluster delay spread; carrier frequencies of 5 GHz were included by characterizing the corresponding path-loss functions. Additional upgrades to the original model comprise the LoS option for all scenarios, tapped-delay line models and time evolution of small scale parameters and the evolution of shadow fading. A reduced version of this model was adopted for the standardization of the 3GPP long term evolution (LTE).

Despite the enhancements introduced in the SCM, SCME was considered inadequate for the simulation of B3G systems. Therefore, the WINNER Phase I channel model (WIM I) was presented in [58]. WIM I has unified structure for indoor and outdoor environments and is based on double-directional measurements campaigns carried out in the 5 GHz band with bandwidths up to 120 MHz. The novel features of the model are its parameterization, the inclusion of elevation in indoor scenarios, autocorrelation modeling of large-scale parameters (including cross-correlation) and scenario-dependent polarization modeling.

WINNER Phase II channel model (WIM II) [59] evolved from WIM I and also from WIM II interim [60] channel models. In the WIM II the channel modeling work of WIM I was continued and the model features were extended: frequency range (2 to 6 GHz), the

number of scenarios, and a new set of multidimensional channel models were developed. They cover wide scope of propagation scenarios and environments and are based on generic channel modeling approach, which means the possibility to vary the number of antennas, the antenna configurations, geometry and the antenna beam pattern without changing the basic propagation model. This method enables the use of the same channel data in different link level and system level simulations and it is well suited for evaluation of adaptive radio links, equalization techniques, coding, modulation, and other transceiver techniques.

CELTIC[3] project WINNER+ has developed, evaluated and integrated innovative additional concepts based on the WINNER II technologies and LTE standard. Therefore, WIM II has been accordingly updated in order to meet the requirements for these additional concepts. The novel features of the WINNER+ models [61] are the elevation modeling, extension of the model down to 450 MHz. WINNER+ Final channel models can be used in link level and system level performance evaluation of wireless systems, as well as comparison of different algorithms, technologies and products. The models can be applied to any wireless system operating in 450 MHz – 6 GHz frequency range with up to 100 MHz RF bandwidth. The model supports multi-antenna technologies, polarization, multi-user, multi-cell, multi-hop networks and 3D modeling.

[3] Celtic-Plus is an industry-driven European research initiative to define, perform and finance through public and private funding common research projects in the area of telecommunications, new media, future Internet, and applications & services focusing on a new "Smart Connected World" paradigm. Celtic-Plus is a EUREKA ICT cluster and is part of the inter-governmental EUREKA network.

Chapter 3

SIMO Measurements and Estimation of the Directional Channel

This chapter begins with a brief discussion of the wideband *directional channel impulse response* (DCIR) characteristics and then, a description of the SIMO measurement system and of the measurement campaign is presented. Afterwards, the estimation of the radio directional channel impulse response, involving the characterization of the most relevant MPCs (delay, DoA, and complex amplitude), is presented: it starts with a short review of the existing signal processing tools for high resolution estimation and description of the selected tool (SAGE algorithm), proceeds with its performance study with synthetic data and ends with results obtained by entering the measured data into this tool.

3.1. The Wideband Radio Channel Characterization

In the multipath propagation channel, several echoes of the transmitted signal arrive at the receiver due to phenomena as reflection, refraction and scattering. For narrowband systems, the channel may be adequately characterized in terms of shadowing by means a lognormal distribution and multipath fading by means a Rayleigh distribution (or a Rice distribution if a strong path is present) [27].

However, it is important to describe also the channel effect if the signal occupies a wide range of frequencies. Therefore, consider two frequencies belonging to a transmitted signal with a given bandwidth. If these two frequencies are sufficiently close, the received amplitudes and phases of different propagation paths (MPCs) will vary approximately the same way in time. This means that though there is fading caused by multipath, the signal presents a very similar behavior at both frequencies. In other words, if the signal bandwidth is sufficiently small, all frequency components in it will behave analogously corresponding to the *flat fading* condition.

As the frequency separation increases, the fading behavior at these two frequencies tends to be uncorrelated with respect to each other, since the corresponding electric lengths will be considerably different. The correlation level thus depends on the time spreading caused by the environment. This circumstance is termed as *frequency selective fading* and means that the signal will become distorted due to a non-uniform filtering of the transmitted signal (non-flat magnitude and nonlinear phase shift). The minimum bandwidth within which the spectral components present similar behavior (a correlation level higher than a given threshold) is known as *coherence bandwidth*.

The delayed replicas of the transmitted signal can be related with specific scatterers in the environment. Therefore, to completely characterize propagation channel, it is not sufficient to know the powers and delays of the several MPCs being also required to characterize their angles of arrival and departure.

3.1.1. Channel System Functions

The radio propagation channel may be viewed as a linear filter that transforms input signals into output signals. However, since the behavior of the channel is generally time-variant, the transmission characteristics of the equivalent filter must be also considered as time-varying. As the inputs and outputs of a linear filter may be related both in time and in frequency domains, there are four transmission functions that can be used to characterize the propagation channel.

The time domain description of linear system is attained by its time impulse response, which, in the case of time-variant channels is also a time-varying function. For a known input signal, the superposition principle allows obtaining the system output in the time domain. If the low-pass equivalent, time-varying impulse response is $h(t,\tau)$, where τ represents the delay variable, then the complex envelope at the output, $y(t)$, is related to the complex envelope at the input, $x(t)$, by the convolution operator as expressed in the following equation [62]

$$y(t) = \int_{-\infty}^{+\infty} x(t-\tau)h(t,\tau)d\tau\,. \tag{3.1}$$

Physically, $h(t,\tau)$ may be understood as the channel response at the time *t* to an input with delay τ. The convolution can be rewritten as summation offering a physical interpretation of the channel given by a tapped delay line comprising differential delay and modulators [27].

The channel may also be characterized in terms of frequency variables by using a function which is dual of $h(t,\tau)$. This function, denoted by $H(f,\nu)$, relates the output spectrum, $Y(f)$, with the input spectrum, $X(f)$, in a similar way as $h(t,\tau)$ relates the input-output time functions [27, 62]. The transmission characteristics are thus described in terms of frequency – *f* – and frequency-shift – ν – variables by the expression

$$Y(f) = \int_{-\infty}^{+\infty} X(f-\nu)H(f-\nu,\nu)d\nu\,. \tag{3.2}$$

While $h(t,\tau)$ enables the perception of multipath by characterizing contributions from different scatterers having different path lengths, the perception of the time-varying behavior of the channel is given by $H(f,\nu)$, where the frequency-shift variable, ν, may be envisaged as the Doppler shift experienced in these channels.

An alternative way of representing the channel is possible if the output time function, $x(t)$, is expressed in terms of the input spectrum, $X(f)$, to the channel equivalent filter [27, 62]. This function, denoted by $T(f,t)$, is called the *time-variant transfer function* and the input-output relationship is

$$y(t) = \int_{-\infty}^{+\infty} X(f)T(f,t)\exp(\mathrm{j}2\pi ft)df\,. \tag{3.3}$$

Function $T(f,t)$ is the Fourier transform of $h(t,\tau)$ with respect to variable τ and also the inverse Fourier transform of $H(f,\nu)$ with respect to variable ν, as expressed in the following expressions

$$T(f,t) = \int_{-\infty}^{+\infty} h(t,\tau)\exp(-\mathrm{j}2\pi f\tau)d\tau = \int_{-\infty}^{+\infty} H(f,\nu)\exp(\mathrm{j}2\pi\nu t)d\nu\,. \tag{3.4}$$

Functions $h(t,\tau)$ and $H(f,\nu)$ characterize only one aspect of the channel's dispersive nature, respectively, the time delay and the Doppler shift. Another important representation of the channel is achieved by using the *scattering function*, $S(\tau,\nu)$, which includes time-delay and Doppler-shift domains. Function $h(t,\tau)$ may be obtained as the inverse Fourier transform of $S(\tau,\nu)$, i.e.,

$$h(t,\tau) = \int_{-\infty}^{+\infty} S(\tau,\nu)\exp(\mathrm{j}2\pi\nu t)d\nu \tag{3.5}$$

and the corresponding input-output relationship is

$$y(t) = \int_{-\infty}^{+\infty} \int_{-\infty}^{+\infty} x(t-\tau) S(\tau,\nu) \exp(\mathrm{j}2\pi\nu t) d\nu d\tau . \tag{3.6}$$

This equation illustrates that output may be envisaged as the sum of delayed and Doppler-shifted contributions whose differential scattering amplitudes are given by $S(\tau,\nu)d\nu d\tau$. Therefore, $S(\tau,\nu)$ explicitly characterizes the dispersive behavior of the channel in terms of time delays and Doppler shifts [62].

3.1.2. Stochastic Description of the Channel

Real radio channels are in general time-variant, thus, the system functions presented in the previous section become stochastic processes, justifying the use of statistical models to characterize the channel. In stochastic models, the channel is usually described in terms of probabilities. One approach consists in describing the channel by means of autocorrelation functions. For example, the autocorrelation function (ACF) the of the random impulse response, $h(t,\tau)$, is defined as

$$R_h(\tau_1,\tau_2,t_1,t_2) = \mathrm{E}\left[h(\tau_1,t_1) h^*(\tau_2,t_2) \right], \tag{3.7}$$

where $(\bullet)^*$ represents the complex conjugate.

Several random radio channels present a dispersive behavior which is uncorrelated in the time-delay domain and in the Doppler-shift domain as well. In these channels the following assumptions are substantiated [62]:

i. The stochastic process, described by the impulse response, $h(t,\tau)$, is *wide sense stationary* (WSS), meaning that the ACF depends only on $\Delta t = t_2 - t_1$ and not on the absolute time instant t, i.e.,

$$R_h(\tau_1,\tau_2,\Delta t) = \mathrm{E}\left[h(\tau_1,t) h^*(\tau_2,t+\Delta t) \right], \tag{3.8}$$

It can be demonstrated that the WSS assumption gives rise to uncorrelated Doppler shift scattering, i.e., the contributions of elemental scatterers are uncorrelated if they produce different Doppler shifts [27].

ii. The complex amplitudes of different path delays are uncorrelated, condition known as *uncorrelated scattering* (US), implying that the ACF vanishes for $\tau_1 \neq \tau_2$ exhibiting a delta-function behavior for $\tau_1 = \tau_2$.

A channel fulfilling both the above assumptions is designated as a WSSUS channel. Such a description of the channel has proved to be a realistic assumption in several radio channels, being also functional in the case of the mobile multipath channel, at least for short section

of the traveled route. The ACF of the impulse response simplifies to $R_h(\tau,\Delta t)$ and the ACF for $T(f,t)$ simplifies to

$$R_T(f_1, f_2, \Delta t) = R_T(\Delta f, \Delta t), \tag{3.9}$$

which depends only on the frequency separation, Δf, and not on the absolute frequencies.

The time domain characterization of WSSUS channels is achieved by the ACF of the impulse response, $R_h(\tau,\Delta t)$. Moreover, this ACF for $\Delta t = 0$ is denoted as $p_h(\tau) = R_h(\tau,0)$ and known as the *power-delay profile* (PDP). This function describes how the received power is distributed by the different delayed echoes arriving to the receiver and may be envisaged as the average over all Doppler shifts of the scattering function. Two statistical moments of $p_h(\tau)$ are of practical interest: the *average delay* and the *delay spread*. The average delay, D_τ, is the first moment of $p_h(\tau)$ given by

$$D_\tau = \frac{\int_{-\infty}^{+\infty} \tau\, p_h(\tau)\, d\tau}{\int_{-\infty}^{+\infty} p_h(\tau)\, d\tau} \tag{3.10}$$

and the delay spread, S_τ, is the square root of the second central moment, defined as

$$S_\tau = \sqrt{\frac{\int_{-\infty}^{+\infty} (\tau - D_\tau)^2\, p_h(\tau)\, d\tau}{\int_{-\infty}^{+\infty} p_h(\tau)\, d\tau}}\,. \tag{3.11}$$

Delay spread is found to be a significant parameter in the design and evaluation of communication systems as it indicates limits for the system performance due to intersymbol interference.

The *spaced-time correlation function* is achieved by particularizing the ACF of $T(f,t)$, defined in equation (3.9), for $\Delta t = 0$, i.e., $R_T(\Delta f, 0)$. On the other hand, the *spaced-frequency correlation function* is achieved by particularizing the same ACF for $\Delta f = 0$, i.e., $R_T(0,\Delta t)$. These functions provide a measure of how much the transmission characteristics of the channel vary with time and frequency spacing, respectively. From these correlation functions, the values of *coherence time* and *coherence bandwidth* may be computed.

The coherence time is the period, T_c, over which the magnitude of the spaced-time correlation function is above a given correlation level. During this period, it can be assumed that the channel transfer function is roughly kept unchanged. The coherence bandwidth is the maximum frequency difference for which the correlation is maintained

above a given correlation level. It may be assumed that the transfer function is approximately constant for frequency separations smaller than the coherence bandwidth.

3.2. SIMO Setup and Measurement Campaign

The measurement system is shown schematically in Figure 3-1. It consists of a 2D positioning device, driven by stepper motors and equipped with one movable antenna connected to the receiving port of a vector network analyzer (VNA). Another static antenna is connected to the VNA transmitting port. The VNA is used to measure the frequency response of the time-invariant channel at the *M* locations of a virtual rectangular antenna array. A personal computer is used to control the positioning device and the VNA through the use of a commercial stepper motor control card and a GPIB interface, respectively. The software needed to control all equipment, acquire and save experimental data was implemented for this purpose in LabVIEW.

The measurements were performed inside and from outside to inside of a sports hall in the campus of University of Aveiro. A set of nine double-directional channel measurements were acquired. Each double-directional measurement is obtained by placing the transmitter (Tx) and the receiver (Rx) in a given arrangement of positions to acquire a forward direction measurement file and then, by exchanging the transmitter and receiver positions, the reverse direction measurement file is acquired. Figure 3-2 presents the transmitter and receiver measurement positions corresponding to the nine forward measurement points and a photograph of one reverse measurement point. The scenario description is represented in a simplified way by black solid lines, where the larger rectangle represents the walls and the smaller rectangle represents the spectator seats.

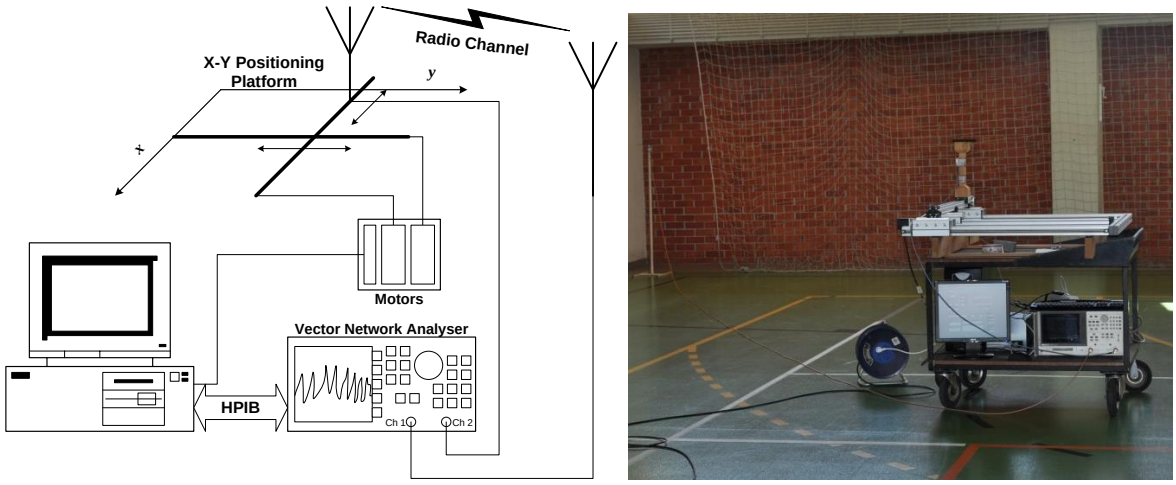

Figure 3-1: Block diagram and a photograph of the SIMO channel measurement system.

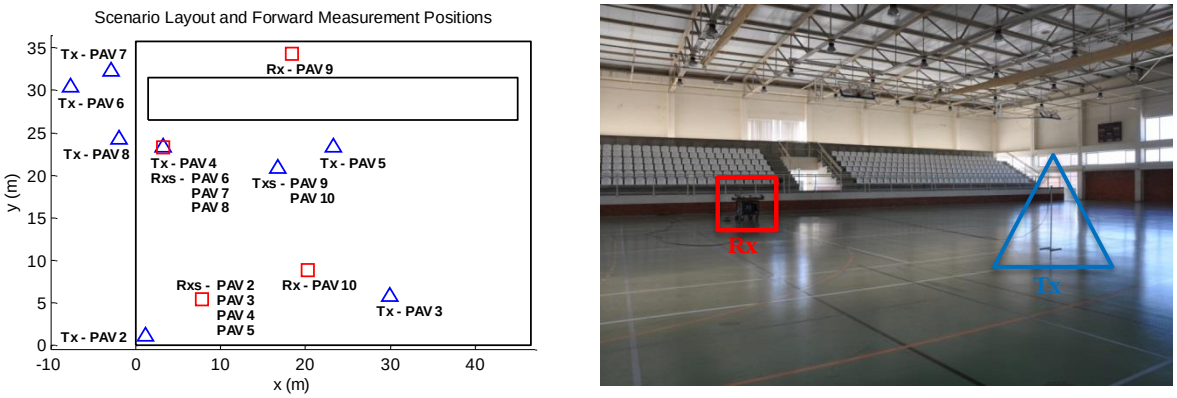

Figure 3-2: Description of the forward measurement positions in the scenario and a photograph corresponding to the reverse measurement position "PAV 10 rv".

For each single-directional measurement position, the (frequency domain) transfer function of the time-invariant channel was measured at $M = 15 \times 15$ receiving positions spaced by $\lambda/8$, in both dimensions. The RF bandwidth used was 200 MHz centered at 2 GHz and comprises 801 frequency sample points. Transmitter and receiver were both equipped with one $\lambda/4$ monopole antenna.

3.3. Estimation of Superimposed Signals

In general terms, the problem involves finding the parameters for a set of L MPCs which acceptably describe the signals observed in a set of M sensors. The signal observed at each sensor is the vector sum result of the several echoes existing in the scenario. A few high resolution algorithms have been proposed and used to estimate the parameters of the impinging waves (MPCs) in mobile radio environments.

3.3.1. High Resolution Algorithms

High resolution techniques developed for these problems are known as *array signal processing* and combine information collected in several sensors. In this context, two kinds of methods may be identified: *spectral estimation* and *parametric estimation* [1]. In the former, a spectral function of the parameters of interest is defined and the maximum locations of this function provide the estimation of the parameters. Spectral-based estimation techniques are computationally attractive but present limited accuracy or even insufficient, especially for scenarios involving highly correlated signals. The so called Multiple Signal Classification (MUSIC) algorithm lies in this kind of techniques [63, 64].

On the other hand, parametric estimation methods exploit more deeply the underlying data model and the estimation of coherent signals imposes no conceptual difficulties to these

methods. The price to pay for this increased efficiency and robustness is that the algorithms typically require a multidimensional search to find the estimates. Parametric estimation may be further classified as *Parametric Subspace-Based Estimation* (PSBE) or *Deterministic Parametric Estimation* (DPE). The method named *Estimation of Signal Parameter via Rotational Invariance Technique* (ESPRIT) and its derivatives fall in the PSBE methods, while *Expectation-Maximization* (EM) and *Space-Alternating Generalized Expectation-Maximization* (SAGE) algorithms belong to DPE.

Standard ESPRIT has been described in [65] and exploits the rotational invariance structure of the signal subspace induced by the translational invariance structure of the corresponding sensor array. Unitary ESPRIT [66-68] constrains the array configuration to those verifying the centro-symmetric[4] property and leads to phase factors lying in the unit circle. The formulation of this extension is similar to the standard ESPRIT but the centro-symmetric property of the array allows real-valued computations providing increased estimation accuracy with a reduced computational burden.

In a wide variety of signal processing applications, the estimate of the unknown parameters can be obtained by maximizing the likelihood function, method known as *maximum likelihood estimation* (MLE). In the case of space-time signal processing, MLE does not impose any constraint to the array configuration. EM and SAGE algorithms are both based on the MLE. In particular, the SAGE algorithm simplifies the complex multidimensional optimization problem, such as estimating the parameters of several waves in a multipath propagation environment, to several separate one-dimensional optimization processes which can be performed sequentially. This algorithm, derived in its general form in [69], is an extension to the EM algorithm [70] and it has been used in areas like image reconstruction [71].

In the context of array signal processing, comparative convergence studies of the EM and SAGE algorithms applied to angle of arrival estimation may be found in [72] using synthetic data, and in [73] using measured sonar data. Concerning the wireless communications context, the SAGE algorithm has been used for joint delay, azimuth and Doppler frequency estimation in time-variant channels [74, 75], as well as, for joint delay, azimuth and elevation estimation in time-invariant channels [76].

EM and SAGE algorithms are presented in the following sections, starting with the underlying signal model. Bearing in mind the nature of the measurements available (section 3.2), the signal model is based on the frequency domain description of the

[4] A sensor array is called centro-symmetric if its elements are symmetric with respect to the centroid and the complex characteristics of paired elements are the same.

channel, i.e., on the transfer function of the channel, justifying why through this work the SAGE algorithm is sometimes referred as (*Frequency Domain*) FD-SAGE algorithm.

3.3.2. Signal Model

In the considered underlying model, a finite number, L, of plane waves are impinging at the receiver antenna array with M elements and the channel is assumed time-invariant. The channel impulse response at the m-th antenna element can be expressed as

$$h_m(\tau,\phi,\beta)=\sum_{\ell=1}^{L}\alpha_\ell \exp\left(\mathrm{j}\frac{2\pi}{\lambda}\langle r_m, e(\phi_\ell,\beta_\ell)\rangle\right)\delta(\tau-\tau_\ell) \tag{3.12}$$

where: τ_ℓ represents the time delay, ϕ_ℓ the incidence azimuth, β_ℓ the incidence elevation (measured with respect to the horizontal plane) and α_ℓ the complex amplitude of the ℓ-th wave; λ denotes the wavelength and $\langle\bullet,\bullet\rangle$ the scalar product; r_m is a row vector containing the m-th antenna element coordinates and

$$e(\phi,\beta)=\left[\cos\beta\cos\phi,\ \cos\beta\sin\phi,\ \sin\beta\right]^{\mathrm{T}} \tag{3.13}$$

is the unit vector in $\mathbb{R}^3$ pointing toward the direction defined by ϕ and β, where $[\bullet]^{\mathrm{T}}$ denotes matrix transposition. In (3.12) the expression

$$c_m(\phi_\ell,\beta_\ell)=\exp\left(\mathrm{j}\frac{2\pi}{\lambda}\langle r_m, e(\phi_\ell,\beta_\ell)\rangle\right) \tag{3.14}$$

accounts for the phase shift, relative to a chosen reference, suffered by the ℓ-th wave due to a small difference in the travelled distance to reach the m-th antenna element. The vector

$$c(\phi,\beta)=\left[c_1(\phi,\beta),\cdots,c_M(\phi,\beta)\right]^{\mathrm{T}} \tag{3.15}$$

is the so called array steering vector. Defining $\theta_\ell=[\tau_\ell,\phi_\ell,\beta_\ell,\alpha_\ell]$ as being the vector which contains the parameters of the ℓ-th wave, the contribution of this wave to the M impulse responses may be expressed as

$$h(\tau;\theta_\ell)=\left[h_1(\tau;\theta_\ell),...,h_M(\tau;\theta_\ell)\right]^{\mathrm{T}}=\alpha_\ell c(\phi_\ell,\beta_\ell)\delta(\tau-\tau_\ell). \tag{3.16}$$

Alternatively, in the frequency domain, the measured channel transfer matrix across the array, possibly corrupted with noise is given by

$$H(f;\theta)=\sum_{\ell=1}^{L}\alpha_\ell c(\phi_\ell,\beta_\ell)\exp(-\mathrm{j}2\pi\tau_\ell f)+N(f) \tag{3.17}$$

with $\theta = [\theta_1, ..., \theta_L]$ and $N(f)$ denoting a *M*-dimensional vector of complex white Gaussian noise, i.e.,

$$N_m(f) = N_{m\Re}(f) + jN_{m\Im}(f), \quad m = 1, \cdots, M \tag{3.18}$$

where $N_{1\Re}(f), N_{1\Im}(f), \cdots, N_{m\Re}(f), N_{m\Im}(f)$ are also random processes of real-valued and independent white Gaussian noise with zero mean and unit spectral power.

The contribution of the ℓ-th wave to the channel transfer function is denoted as

$$S(f;\theta_\ell) = \alpha_\ell c(\phi_\ell, \beta_\ell) \exp(-\mathrm{j}2\pi\tau_\ell f). \tag{3.19}$$

In addition, consider

$$S(f;\theta) = \sum_{\ell=1}^{L} S(f;\theta_\ell). \tag{3.20}$$

The problem to solve is the estimation of the channel parameters, i.e., to obtain the *L* components of vector θ.

3.3.3. Maximum-Likelihood Estimation and the EM Algorithm

The log-likelihood function of θ given an observation $H(f) = y(f)$ over D_{obs} is [74]

$$\Lambda(\theta; y) = 2\int_{D_{obs}} \mathrm{Re}\left\{S^H(f';\theta)\, y(f')\right\} df' - \int_{D_{obs}} \left\| S^H(f';\theta) \right\| df' \tag{3.21}$$

where $\|\bullet\|$ represents the Euclidean norm and $[\bullet]^H$ denotes conjugate transpose operator. The MLE of θ is the value of this vector which maximizes the function $\theta \mapsto \Lambda(\theta; y)$, i.e.,

$$\hat{\theta}_{\mathrm{ML}}(y) \in \arg\max_{\theta} \left\{\Lambda(\theta; y)\right\}. \tag{3.22}$$

Obtaining $\hat{\theta}_{\mathrm{ML}}(y)$ is computationally prohibitive owing to its high dimension when *L* is large and also because there is no closed formula to express the maxima of the log-likelihood function used by the MLE. Even taking into consideration that the values of the complex amplitudes may be expressed as a function of the other parameters, the procedure to obtain the MLE represents a 3*L*-D nonlinear optimization process [74].

The EM algorithm [70] appears as a general method to solve the MLE problem in an iterative way. It has been developed to address this problem when a part of the observations is missing or suppressed. The primary idea is to decompose the observed signal in the several components and in estimating the parameters of each component individually. This algorithm is based on two key concepts: the *complete data* (unobservable) and the *incomplete data* (observable), allowing the decomposition of the

above procedure in L 3-D optimization procedures to estimate the waves' parameters, which may be performed separately and in parallel. Each 3-D optimization procedure aims to obtain the parameters of a given wave only. In our problem, a possible choice for the complete data set is the contribution of each individual wave to the channel transfer function, corrupted by a fraction of the additive noise, i.e.,

$$X_\ell(f) = S(f;\theta_\ell) + \sqrt{\mu_\ell}N(f) \tag{3.23}$$

where, μ_ℓ, $\ell = 1, \ldots, L$, must satisfy

$$\sum_{\ell=1}^{L} \mu_\ell = 1 . \tag{3.24}$$

The vector containing the parameters of the ℓ-th wave, θ_ℓ, constitutes one parameter subset. On the other hand, the measured (observed) channel transfer function, $H(f)$, represents the incomplete data set. Figure 3-3 shows the relation between these data sets.

To understand the rationale principle of the EM algorithm, consider that the complete data may be observed. Taking into account that $X_1(f), \cdots, X_L(f)$ are independent, the components $X_{\ell'}, \ell' \neq \ell$ are irrelevant for the estimation of θ_ℓ. The log-likelihood function for θ_ℓ, given the observation $X_\ell(f) = x_\ell(f)$ over D_{obs} is similar to (3.21), i.e.,

$$\Lambda(\theta_\ell; x_\ell) = 2\int_{D_{obs}} \mathrm{Re}\left\{S^H(f';\theta_\ell)\, x_\ell(f')\right\} df' - \int_{D_{obs}} \left\| S^H(f';\theta_\ell) \right\| df' , \tag{3.25}$$

and the corresponding MLE is

$$\left(\hat{\theta}_\ell\right)_{\mathrm{ML}}(x_\ell) \in \arg\max_{\theta_\ell} \left\{\Lambda(\theta_\ell; x_\ell)\right\} . \tag{3.26}$$

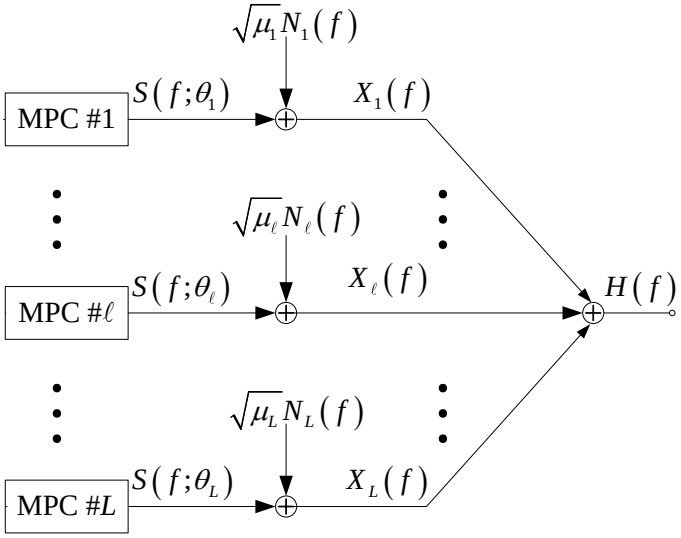

Figure 3-3: Relation between the complete data (unobservable) and the incomplete data (observable).

As $X_\ell(f)$ is not observable, its estimation may be based on the observation $H(f)=y(f)$ of the incomplete data and on the previous estimate, θ', of θ. The most obvious way to proceed is to obtain the conditional expectation of $X_\ell(f)$ given the observation $H(f)=y(f)$ and assuming $\theta=\theta'$, i.e.,

$$\hat{x}_\ell\left(f;\hat{\theta}'\right)=\mathrm{E}_{\hat{\theta}'}\left[X_\ell(f)|y\right],\quad \ell=1,\cdots,L \tag{3.27}$$

where $\mathrm{E}_\theta[\bullet]$ represents the expectation assuming the parameter value θ. The parameters of θ_ℓ may be updated by calculating its MLE given the observation $X_\ell(f)=\hat{x}_\ell\left(f;\hat{\theta}'\right)$ according to

$$\theta_\ell''=\left(\hat{\theta}_\ell\right)_{\mathrm{ML}}\left(\hat{x}_\ell\left(f;\hat{\theta}'\right)\right),\quad \ell=1,\cdots,L\,. \tag{3.28}$$

Operations in equations (3.27) and (3.28) are mentioned, respectively, as E-step (*Expectation*) and M-step (*Maximization*) of the EM algorithm [74]. Starting with an initial estimate $\hat{\theta}(0)$, the algorithm produces a sequence of estimates $\left\{\hat{\theta}(n):n=0,1,\cdots\right\}$ by performing iteratively these two steps. In the *n*-th iteration the assignments $\hat{\theta}'=\hat{\theta}(n)$ and $\hat{\theta}_\ell''=\theta_\ell(n+1)$, for $\ell=1,\cdots,L$ are made.

Figure 3-4 presents the signal flowchart of the EM algorithm and as it evidences, the major advantage of this algorithm is that it enables to decompose the 3*L*-D nonlinear optimization process, essential to jointly estimate the parameters of the *L* MPCs, into *L* 3-D optimization problems, which may be carried out separately, each providing the estimate of a single MPC.

Inserting (3.19) in (3.25) it can be shown that the complex amplitude, α_ℓ, which maximizes $\Lambda(\theta_\ell;x_\ell)$ may be obtained in a closed form as a function of $[\tau_\ell,\phi_\ell,\beta_\ell]$ and approximating the integral by a sample summation, yields to the following procedure for the algorithm's M-step

$$\left(\hat{\tau}_\ell,\hat{\phi}_\ell,\hat{\beta}_\ell\right)_{\mathrm{ML}}(x_\ell)=\arg\max_{[\tau,\phi,\beta]}\left\{\left|z(\tau,\phi,\beta;x_\ell)\right|\right\} \tag{3.29}$$

$$\left(\hat{\alpha}_\ell\right)_{\mathrm{ML}}(x_\ell)=\frac{1}{MN}z\left(\left(\hat{\tau}_\ell,\hat{\phi}_\ell,\hat{\beta}_\ell\right)_{\mathrm{ML}}(x_\ell);x_\ell\right) \tag{3.30}$$

with *N* the number of samples in the frequency domain and

$$z(\tau,\phi,\beta;x_\ell)=c^H(\phi,\beta)\,x_\ell(f)\exp(\mathrm{j}2\pi f\tau)\,. \tag{3.31}$$

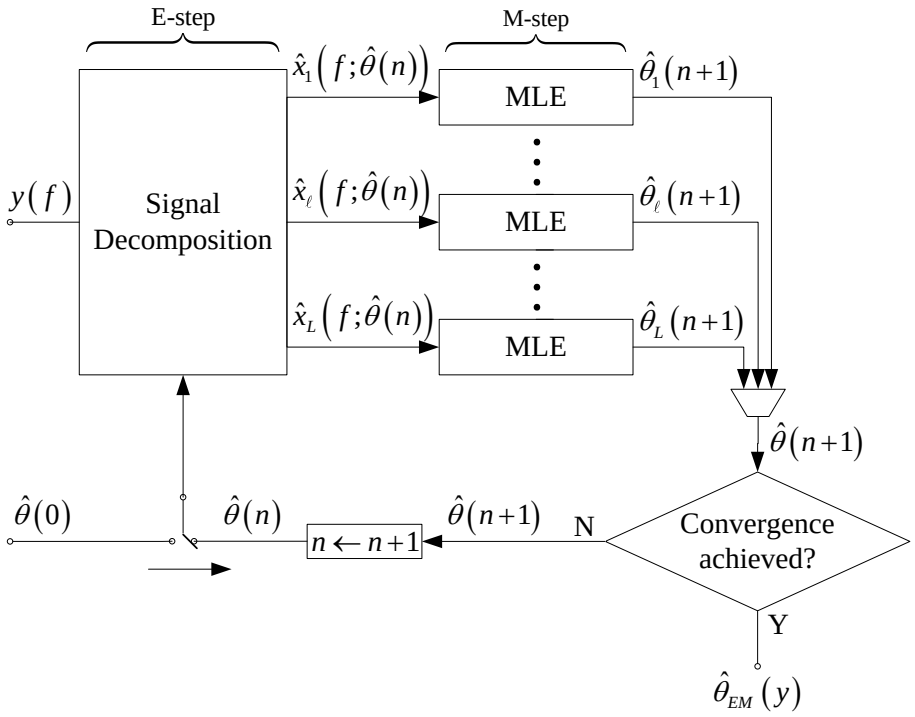

Figure 3-4: Signal flowchart of the EM algorithm.

The estimate, $\hat{x}_\ell\left(f;\hat{\theta}'\right)$, of the complete data set, $X_\ell(f)$, may be obtained by

$$\hat{x}_\ell\left(f;\hat{\theta}'\right) = S\left(f;\hat{\theta}'_\ell\right) + \mu_\ell\left[y(f) - \sum_{\ell'=1}^{L} S\left(f;\hat{\theta}'_{\ell'}\right)\right] \tag{3.32}$$

where the first denotes the contribution of the ℓ-th MPC assuming $\theta_\ell = \theta'_\ell$ and the expression within brackets represents an estimate of the noise assuming $\theta = \theta'$. Given equations (3.30) and (3.32) present low computational effort, the complexity of the EM algorithm is essentially determined by the 3-D optimization procedure in equation (3.29). Taking into account the constraint imposed by equation (3.24), the nonnegative coefficients may be freely chosen in order to maximize the convergence speed of the algorithm.

3.3.4. Description of the SAGE Algorithm

The SAGE algorithm may be viewed as an extension of the EM algorithm: each one of the SAGE iterations is, in fact, an EM iteration to update just a subset of the components of θ, maintaining the parameters of the other components fixed at their previous values. For each of these subsets, an admissible hidden data is defined, such that, it represents a complete data set, if the components belonging the complementary subset are assumed to be known. This way, the algorithm replaces the L 3-D parallel optimization procedures, used in the EM algorithm, by a serial optimization approach. As a result, according to [69]

and [74], in comparison to the EM algorithm, the SAGE algorithm presents faster convergence and lower complexity.

Again, the complete data set is chosen to be the contribution of each wave to the channel transfer function as given in (3.23) but choosing μ_ℓ=1, resulting in the following procedure to obtain the estimate, $\hat{x}_\ell\left(f;\hat{\theta}'\right)$, of the complete data set, $X_\ell(f)$, corresponding to the E-step of the algorithm,

$$\hat{x}_\ell\left(f;\hat{\theta}'\right) = y(f) - \sum_{\substack{\ell'=1 \\ \ell'\neq\ell}}^{L} S\left(f;\hat{\theta}'_{\ell'}\right). \tag{3.33}$$

Figure 3-5 shows the signal flowchart of the SAGE algorithm. Contrasting with the EM algorithm (Figure 3-4), which at each iteration updates the estimates of all MPCs (all components of θ), note that the SAGE algorithm, at the n-th elementary iteration, updates only the parameters of the component $\ell = (n \bmod L)+1$. An *iteration cycle* of the SAGE algorithm is defined as L consecutive elementary iteration steps needed for updating the parameter estimates of all MPCs once. The computational complexity of one iteration step of the EM algorithm is identical to that of one iteration cycle of the SAGE algorithm. Therefore, the rationale leading to the SAGE algorithm is directly based on the EM algorithm but it allows for complexity reduction by simplifying the optimization procedure and also presents faster convergence as each new estimate of θ_ℓ, obtained at the n-th elementary iteration step is immediately used at (n+1)-th elementary iteration step.

Additional complexity reduction may be achieved within the SAGE algorithm framework, by further decomposing the optimization procedure. Each subset θ_ℓ is split into three subsets: $[\tau_\ell,\alpha_\ell]$, $[\phi_\ell,\alpha_\ell]$ and $[\beta_\ell,\alpha_\ell]$ and the MLE is obtained for the parameters in each subset while maintaining the parameters in other sets fixed. As already mentioned, the MLE of α_ℓ may be expressed as a function of $[\tau_\ell,\phi_\ell,\beta_\ell]$, so that the 3-D optimization procedure in equation (3.29) reduces to 3 1-D optimization procedures. The update procedures needed to obtain a new estimate for the parameters of the ℓ-th wave, $\hat{\theta}''_\ell$, given the previous estimates of all waves, $\hat{\theta}'$, can then be written as

$$\hat{\tau}''_\ell = \arg\max_{\tau}\left\{\left|z\left(\tau,\hat{\phi}'_\ell,\hat{\beta}'_\ell;\hat{x}_\ell\left(f;\hat{\theta}'\right)\right)\right|\right\}, \tag{3.34}$$

$$\hat{\phi}''_\ell = \arg\max_{\phi}\left\{\left|z\left(\hat{\tau}''_\ell,\phi,\hat{\beta}'_\ell;\hat{x}_\ell\left(f;\hat{\theta}'\right)\right)\right|\right\}, \tag{3.35}$$

$$\hat{\beta}''_\ell = \arg\max_{\beta}\left\{\left|z\left(\hat{\tau}''_\ell,\hat{\phi}''_\ell,\beta;\hat{x}_\ell\left(f;\hat{\theta}'\right)\right)\right|\right\}, \tag{3.36}$$

$$\hat{\alpha}''_\ell = \frac{1}{MN} z\left(\hat{\tau}''_\ell,\hat{\phi}''_\ell,\hat{\beta}''_\ell;\hat{x}_\ell\left(f;\hat{\theta}'\right)\right), \tag{3.37}$$

where $z(\tau,\phi,\beta;x_\ell)$ is given by (3.31).

Like in the original EM algorithm, the SAGE basic iteration stage that updates the parameters of a given wave comprises two steps: the E-step, given in (3.33), aims to obtain the expected complete data set; and the M-step, given in equation (3.29) and (3.30) [or in (3.34) – (3.37)], performs the MLE estimation of each parameter of the considered wave.

Initialization of the SAGE algorithm

Beginning with the pre-initial setting $\hat{\theta}' = [0,\cdots,0]$, the initial estimates for each $\ell = 1,\cdots,L$ are obtained according to

$$\hat{\tau}_\ell'' = \arg\max_{\tau}\left\{\sum_{m=1}^{M}\left|\hat{X}_\ell\left(f;\hat{\theta}'\right)\exp\left(\mathrm{j}2\pi f\tau\right)\right|\right\} \tag{3.38}$$

$$\left(\hat{\phi}_\ell'',\hat{\beta}_\ell''\right) = \arg\max_{[\phi,\beta]}\left\{\left|z\left(\hat{\tau}_\ell'',\phi,\beta;\hat{X}_\ell\left(f;\hat{\theta}'\right)\right)\right|\right\} \tag{3.39}$$

and (3.37) to obtain $\hat{\alpha}_\ell''$.

In (3.38) the term inside the summation expresses a frequency correlation. It is used as a method to obtain the initial delay estimate since at this point $\hat{\phi}_\ell'$ and $\hat{\beta}'$ are unknown. The 2-D optimization in (3.39) is used instead of (3.35) and (3.36) because according to [76] assuming $\hat{\beta}_\ell' = 0$ may cause an erroneous azimuth estimation.

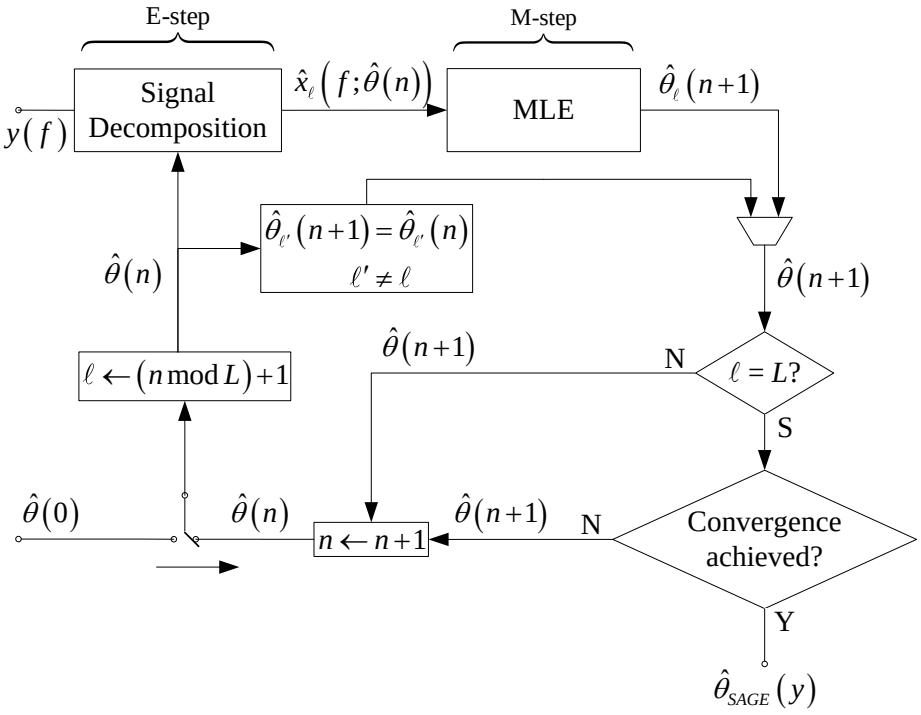

Figure 3-5: Signal flowchart of the SAGE algorithm.

3.4. SAGE Results using Synthetic Data

It is important to investigate the SAGE algorithm capability to retrieve the superimposed signals. For this purpose, a preliminary study has been performed using synthetic data, provided by the extended Saleh-Valenzuela (ESV) model (the available version has been implemented by [77]). As described in section 2.4.6, the ESV model characterizes complex amplitude, time of arrival (ToA), angle of arrival [48] and angle of departure [49] for each multipath component (MPC). This model assumes that rays (or MPCs) arrive at the receiver in clusters and also that they have different statistical distributions for each of the parameters.

In order to study how the number of MPCs in the channel and their relative power influence the quality of the solution obtained, several sets of data have been generated using different combinations for number of clusters (NC) – number of rays in each cluster (NR) and also with different combinations for the time constants controlling the power decay (Γ and γ). The arrival rates were the same for all sets. Three of these sets were selected to present here and the corresponding parameters, used in the ESV model, can be found in Table 3-1.

The output of the ESV model is then used to obtain the transfer function matrix of the channel by using equation (3.17) but considering no added noise. The frequency response of the channel is computed at $M = 11 \times 11$ positions, spaced by 0.5λ in both dimensions, each comprising 801 frequency samples in a 200 MHz bandwidth and centered on 2 GHz. Finally, by providing the SAGE with the frequency responses matrix of each synthetic channel, the corresponding MPCs estimates are obtained for comparison purposes.

Selected results are displayed in Figure 3-6 to Figure 3-11 and were also presented in [78]. Observing the impulse responses of the sets presented here, it can be perceived that in two of them – Figure 3-6 (corresponding to "ch4") and Figure 3-8 (corresponding to "ch9") – although the number of MPCs is very different, they present almost the same amplitude range (from 0 dB to about −30 dB) and in Figure 3-10 the amplitude range is wider (from 0 dB to about −60 dB). Therefore, the first two cases were classified as *"moderate"* power decay and the last one classified as *"pronounced"* power decay, respectively.

Table 3-1: Parameters for the ESV model used to generate the data sets.

Set Name	NC	NR	Γ (ns)	γ (ns)	Comment
ch3	5	10	60	20	"*Pronounced"* power decay
ch4	3	5	90	30	"*Moderated"* power decay
ch9	5	10	120	40	"*Moderated"* power decay

From the results shown it can be concluded that if the channel presents a small number of rays and moderate power decay (Figure 3-6 and Figure 3-7) the SAGE algorithm is able to retrieve a good estimate for almost all the rays. In this particular case, notice that only the last two rays (152 ns and 153 ns), which are simultaneously the ones with lowest power, were not correctly estimated. Instead, two nonexistent rays are placed near one of the first rays (37 ns), which present much higher power. These fictitious rays present delay and azimuth very similar to the real one, but much lower amplitude. Average delay, delay spread, average azimuth and azimuth spread for the considered channel and the respective SAGE retrieval have been computed and compared. For this case errors were less than 1% for all parameters, showing that, despite the failure in the estimation of those two rays, the retrieved waves represent a good description of this channel.

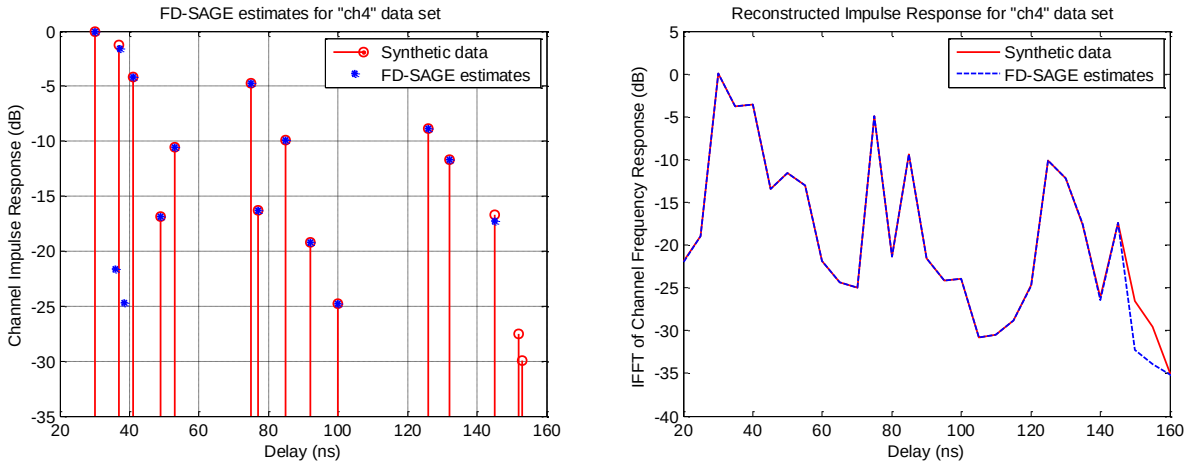

Figure 3-6: SAGE retrieval results (15 estimates requested) for "ch4" (15 rays, "*moderate*" power decay). **Left:** Generated impulse response and SAGE retrieval. **Right:** Reconstructed impulse responses by using IFFT on frequency responses obtained with equation (3.17).

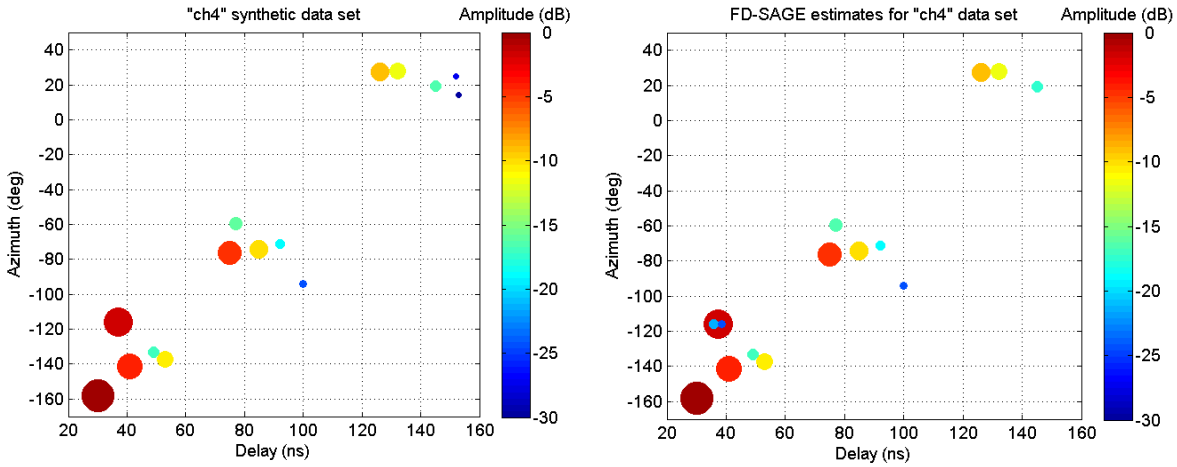

Figure 3-7: Directional impulse responses (time and azimuth domains) for "ch4". **Left:** ESV generated impulse response. **Right:** SAGE retrieved impulse response.

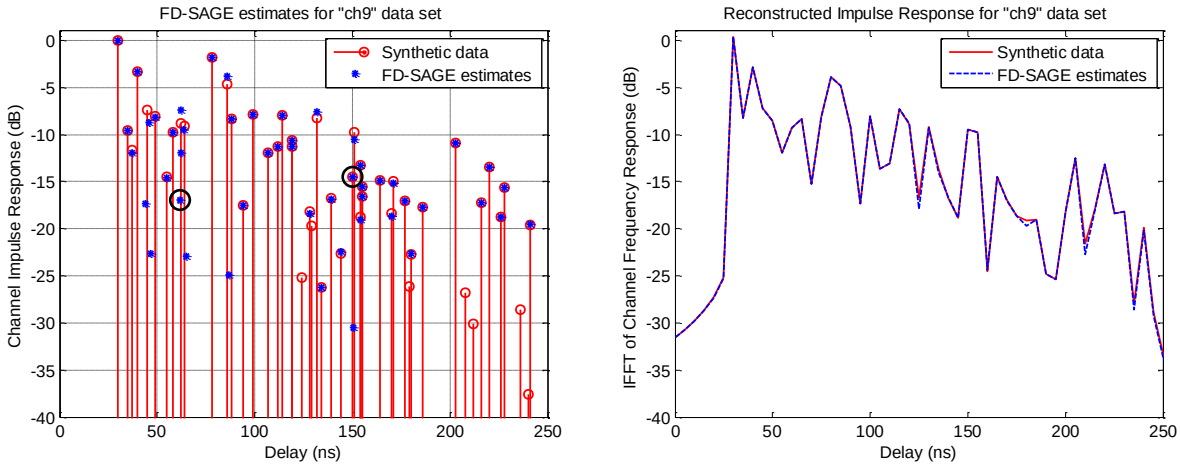

Figure 3-8: SAGE retrieval results (50 estimates requested) for "ch9" (50 rays, *"moderate"* power decay). **Left:** Generated impulse response and SAGE retrieval. **Right:** Reconstructed impulse responses by using IFFT on frequency responses obtained with equation (3.17).

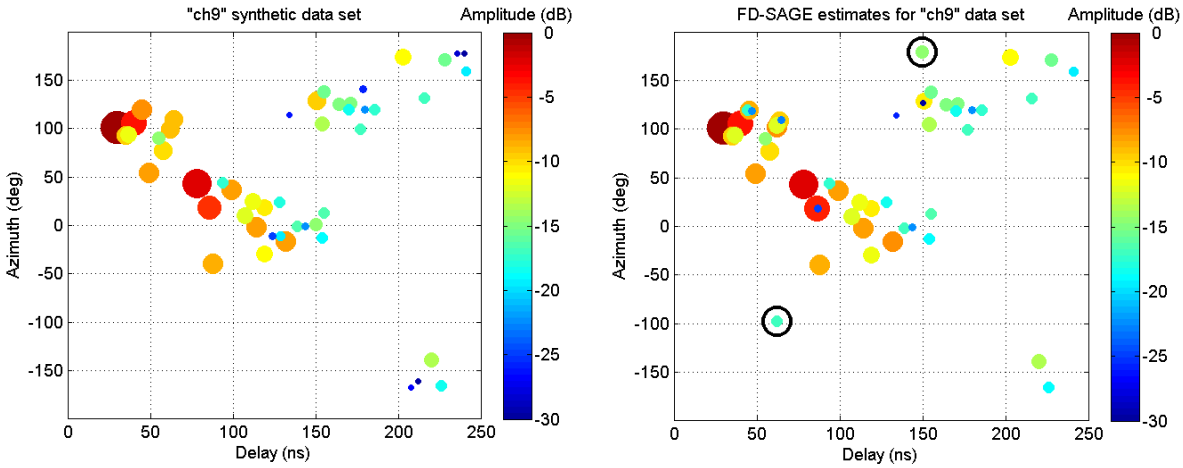

Figure 3-9: Directional impulse responses (time and azimuth domains) for "ch9". **Left:** ESV generated impulse response. **Right:** SAGE retrieved impulse response.

As the number of rays in the channel increases, the number of rays whose estimate is lost increases and therefore, the number of fictitious rays retrieved also increases. In the case of "ch9" (Figure 3-8 and Figure 3-9), although the retrieved rays still provide a good description of the channel (average delay and average azimuth errors less than 1%, delay spread error about 2.4% and azimuth spread error about 2%), SAGE algorithm failed to estimate correctly 8 rays (out of a total of 50) and, obviously, there are 8 fictitious MPCs in the solution given by the algorithm. Like in the previous case, it can be observed, that fictitious rays typically present delay and azimuth similar to an existing one. In addition, it can be perceived that placing these fictitious MPCs near a real one seem to cause a loss in quality of the corresponding estimate.

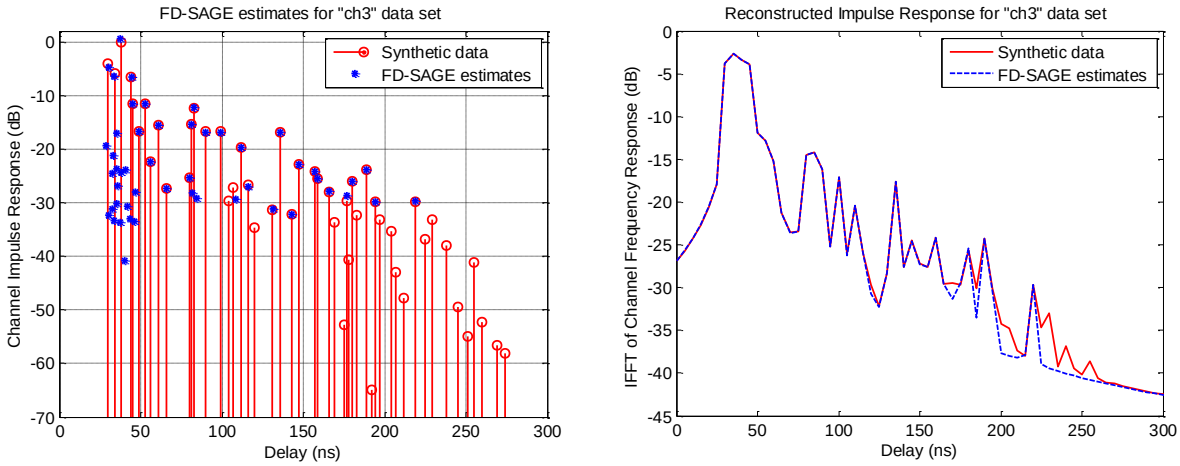

Figure 3-10: SAGE retrieval results (50 estimates requested) for "ch3" (50 rays, *"pronounced"* power decay). **Left:** Generated impulse response and SAGE retrieval. **Right:** Reconstructed impulse responses by using IFFT on frequency responses obtained with equation (3.17).

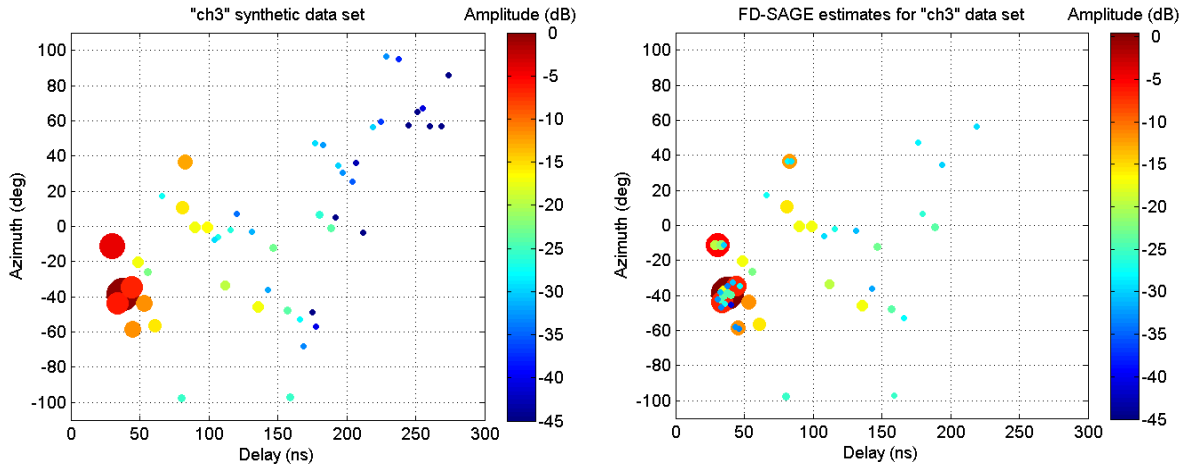

Figure 3-11: Directional impulse responses (time and azimuth domains) for "ch3".
Left: ESV generated impulse response. **Right:** SAGE retrieved impulse response.

If power decay becomes more pronounced the phenomenon also becomes more severe and thus, more evident. In the case of "ch3" (Figure 3-10 and Figure 3-11), the number of failed rays has increased to 20 (40% of the rays in the channel). Nevertheless, in general, the lost rays are the ones presenting lower power, so the impact is not as bad as one could expect at first glance (for this case, average delay error is about 1%, delay spread error about 6%, average azimuth error about 2.5% and azimuth spread error about 3.1%).

However, in "ch9", there are two interesting results highlighted in Figure 3-8 and Figure 3-9 by a black circle. One regards to a real MPC (62 ns, 99.3º) for which it can be identified two estimates with similar parameters (one being fictitious) and a third presenting similar delay but very different azimuth (-97.3º). The other case corresponds to

a real MPC (150ns, 1.05º) for which delay and amplitude are correctly estimated but not the azimuth (178.9º instead 1.05º).

Moreover, this data set enables to conclude also that may not be easy to establish a well-defined criterion for estimation limits as "components with power above a certain threshold" or "maximum delay" as the algorithm seems not to follow a strict order: note that there are MPCs without a corresponding estimate with delays smaller than the last MPC estimated (241 ns) and also with higher power than the MPC estimated presenting the lowest power (-26.3 dB). Consequently, if one tries to reduce the number of MPCs that is requested for estimation by the SAGE algorithm, aiming to reduce the number of fictitious rays, some estimates of real MPCs may be lost (it is even possible to loose only real MPCs without reducing the number of fictitious MPCs). Therefore, the number of rays that is requested for estimation by the SAGE algorithm must be carefully chosen. It is important to be aware that some MPCs provided by the algorithm may be fictitious and if one does not have previous knowledge of the channel properties, one may not distinguish them easily. Nevertheless, fictitious rays are likely to show parameters very similar to their neighbors, as if they were repeated, causing a slight loss in the quality of the real MPC estimate, but maintaining the major properties of the channel (delay and azimuth spreads).

Considering the results on the performance of SAGE algorithm presented in this section, it can be perceived that, sometimes, the algorithm fails to estimate some of the most delayed and lower power MPCs and provides, in their place, some fictitious MPCs. As the number of MPCs in the channel and the power decay increases, the number of MPCs whose estimate is lost increases and therefore, the number of fictitious MPCs retrieved also increases. In general, the lost MPCs are the ones with less power and thus, the impact is not as critical as one could initially expect: mean delay, delay spread, mean azimuth and azimuth spread errors presented are acceptable.

Although observations and conclusions taken from this performance study evidence some failures, the estimate of the directional impulse response is satisfactory, so this tool may, globally, be considered adequate for further use with experimental data in order characterize the directional impulse response of measured channels.

3.5. Experimental DCIRs obtained with SAGE algorithm

As explained in section 3.2, each double-directional measurement comprises two measurement files (forward and reverse directions). In its turn, each measurement file contains the matrix of the channel transfer functions, along with the corresponding sensor

positions. In order to obtain the parameters estimate for a given number of MPCs, each matrix of measured frequency responses has been used as input to the SAGE algorithm.

Figure 3-12 and Figure 3-13 present the results for one of the measurement positions listed in Figure 3-2. In left side of these figures, it can be observed the time domain impulse response of the channel, obtained by IFFT from the measured frequency responses and averaged over all sensors; the corresponding MPCs retrieved by the SAGE algorithm; and the time domain impulse response, obtained by IFFT using the frequency responses reconstructed from the SAGE outputs. In the right side, it can be observed the DCIR estimated by the SAGE algorithm. Directions of arrival (azimuth) are given with respect to the direction defined by the position of the transmitter, i.e., the transmitter presents always zero azimuth ($\phi = 0^o$).

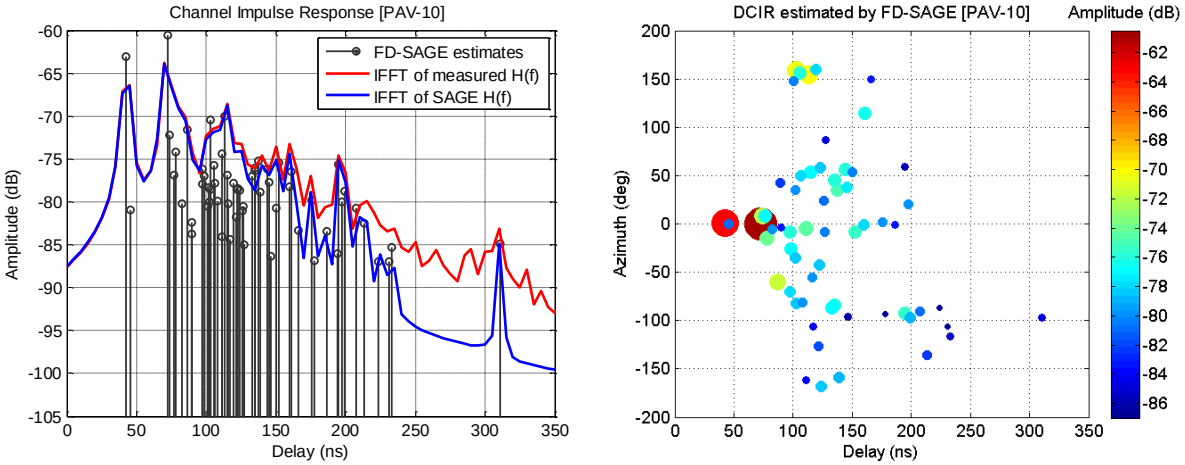

Figure 3-12: Forward measurement results [PAV-10] – **Left:** Average impulse response obtained from measurements and SAGE output. **Right:** DCIR estimated by SAGE.

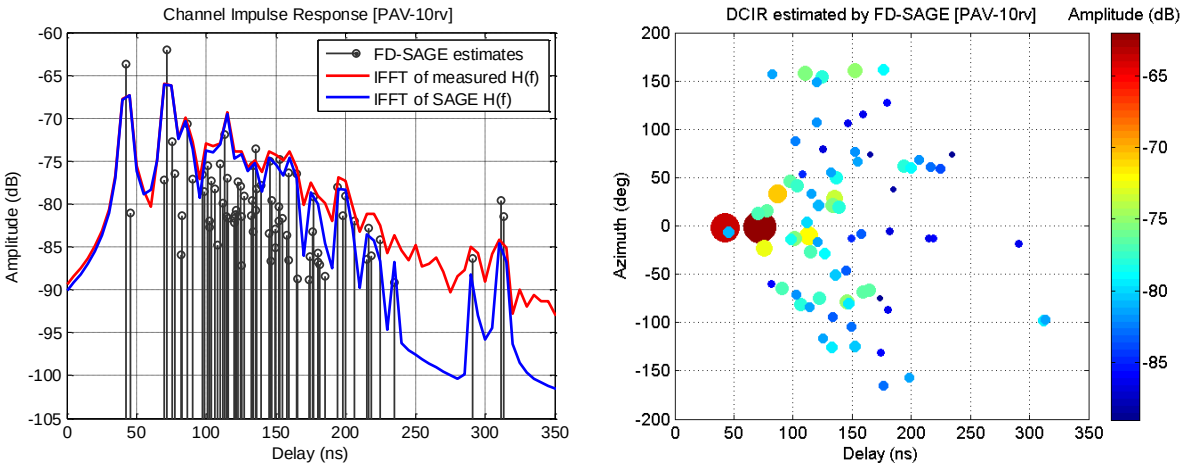

Figure 3-13: Reverse measurement results [PAV-10rv] – **Left:** Average IR obtained from measurements and SAGE output. **Right:** Directional IR estimated by SAGE.

The number of MPCs may be estimated, from observed data, by applying well-known information theoretic criteria, namely, the Akaike information criterion (AIC) and the minimum description length (MDL) [79], for which several performance studies and improvements have been reported [80-82], since when these were first proposed. Nevertheless, one must take into account the behavior presented by the SAGE algorithm in section 3.4, showing that, even in the absence of noise, the algorithm misses some of the rays undergoing longer delays and supplies, in their place, fictitious rays. As a result, the number of rays to be requested from the SAGE algorithm, *L*, has been manually chosen by carrying out several attempts (trying different values) and analyzing the time domain impulse response of the measured channel, averaged over all sensors, and the output results of the SAGE algorithm as shown in the left side of Figure 3-12. For each processed measurement data file, the number of MPCs to be estimated, *L*, has been set to that value above which continuing increasing this value would not provide MPCs in "new" delays, i.e., higher delays than the current maximum delay or not covered delays, as the gap between 250 ns and 300 ns in left side of Figure 3-12.

Again, the average delay and delay spread had been computed, for the measurements and for the SAGE results, both using the averaged (over all sensors) IFFTs of the frequency responses. In general, results were within a maximum error of 10% by considering IFFT contributions which are within a minimum dynamic range of 19 dB below the highest peak. In some measurement files, it was possible to increase this dynamic range to more than 25 dB (especially in non-LoS measurements). In the particular case of the measurement files presented in Figure 3-12 and Figure 3-13 (respectively, forward and corresponding reverse measurement) the dynamic range considered is 19 dB, resulting in about 3% for average delay error (both measurements); 8.6% for forward measurement delay spread error and 0.3% for reverse measurement delay spread error.

Chapter 4

Exploratory Study of the Directional Channel Information

Several of the existing physical channel models [25, 47, 49] assume that MPCs arrive in clusters, i.e., groups of MPCs showing analogous parameters such as delay, DoA and DoD. In fact, results from measured channels show that MPCs often appear in clusters [48, 83] and normally, this may be confirmed by a simple visual inspection. Therefore, it is essential that cluster-based channel models be able to describe the relevant characteristics of the clusters. Such models may be parameterized by extracting the information needed from experimental data.

Obviously, visual inspection is not suitable, thus more rigorous and objective methods are required to perform clustering. In this context, a wide range of options to perform classification of data may be found in the literature [84, 85]. In this work, the K-means algorithm which belongs to the group of partitioning algorithms has been used. In [86] this algorithm has already been successfully applied to the problem of clustering the radio channel parameters and there it is referred as *KPowerMeans* (KPM) because it also considers the power of the MPCs when performing the clustering.

This chapter starts with a brief review of the clustering algorithms, focusing mainly on the selected algorithm. Contents in section 4.1 are widely based in [84] and [85]. The cluster validation subject is also addressed, i.e., attention is paid to the problem of estimating the number of clusters in multipath radio channel data sets. Cluster validity indices allow comparing and ranking several clustering solutions, with different number of clusters, thus enabling the selection of the best solution. Results on the performance evaluation of the chosen clustering framework using synthetic data are presented. Subsequently, the clustering output solutions for experimental DCIRs estimated in chapter 3, with the SAGE algorithm, are given. Finally, this chapter closes with a physical analysis relating each cluster with the obstacles present in the scenario: clusters are further classified according to the type of interaction which they represent (direct ray, single interaction, higher order interaction). Moreover, clusters from each double-directional measurement, are linked at this step also.

4.1. Brief Review of Clustering Algorithms

The purpose of any clustering tool is to evaluate the relationships among patterns, usually vectors in the multidimensional space, in order to organize these patterns into groups, or clusters, based on the principle of *maximizing the intra-cluster similarity and minimizing the inter-cluster similarity*. That is, patterns in the same cluster are more *similar* to each other and patterns belonging to different clusters are more *dissimilar*. Similarities or dissimilarities are assessed based on the attributes values describing the patterns. Often, distance measures are used.

Typical pattern clustering activity involves the following steps:

i. Pattern representation (optionally including feature extraction and/or selection);
ii. Definition of a pattern proximity measure appropriate to the data domain;
iii. Clustering or grouping;
iv. Data abstraction;
v. Assessment of output.

Pattern representation refers to the number of available patterns, the number, type, and scale of the features available to the clustering algorithm. *Feature selection* is the process of identifying the most effective subset of the original features to use in clustering. *Feature extraction* is the use of one or more transformations of the input features to produce new salient features. Either or both of these techniques can be used to obtain an appropriate set of features to use in clustering.

Pattern proximity or *similarity* is usually measured by a distance function defined on pairs of patterns. To help avoid dependence on the choice of measurement units, the data should be standardized. Standardizing measurements attempts to give all features (variables) an equal weight. However, in some applications, users may intentionally want to give more weight to certain feature than to the others. The most popular distance measure is Euclidean distance. If each feature is assigned a weight according to its perceived importance, the weighted Euclidean distance may be expressed as

$$d_{ij} = \sqrt{w_1 \left| x_{i1} - x_{j1} \right|^2 + w_2 \left| x_{i2} - x_{j2} \right|^2 + \cdots + w_m \left| x_{im} - x_{jm} \right|^2} , \tag{4.1}$$

where patterns $\mathbf{x}_i$ and $\mathbf{x}_j$ are single data items consisting in vectors which contain *m* features, i.e., $\mathbf{x} = [x_1, \cdots, x_m]$ and $w_1, \cdots, w_m$ are feature the weights. Minkowski distance is a generalized metric defined as

$$d_{ij} = \left(\left| x_{i1} - x_{j1} \right|^p + \left| x_{i2} - x_{j2} \right|^p + \cdots + \left| x_{im} - x_{jm} \right|^p \right)^{\left(1/p \right)} , \tag{4.2}$$

where *p* is a positive integer. It represents the Euclidean distance for $p = 2$ and for $p = 1$ such distance is known as the Manhattan distance. Weighting can also be applied to the Minkowski distance.

The *grouping* step can be performed in a number of ways. In general, the output clustering can be *hard* or *fuzzy*: a *hard clustering* algorithm allocates each pattern to a single cluster during its operation and in its output; a *fuzzy clustering* method assigns degrees of membership in several clusters to each input pattern. A fuzzy clustering can be converted to a hard clustering by assigning each pattern to the cluster with the largest measure of membership.

It is difficult to provide a crisp categorization of clustering methods because these categories may overlap, so that a method may integrate ideas of several categories. Nevertheless, it is useful to present a relatively organized picture of the different clustering methods. The major clustering methods may be classified into the following categories:

- **Partitioning methods:** For a database of *N* objects or data patterns, a partitioning method constructs *K*, partitions of the data, where each partition represents a cluster and $K \leq N$. A problem accompanying the use of partitioning algorithms is the choice of the number of desired partitions to construct, *K*. But given *K*, a partitioning method creates an initial partitioning and then uses an iterative relocation technique that attempts to improve the partitioning by moving objects from one group to another. The general criterion of a good partitioning is that

objects in the same cluster are *close* or related to each other, whereas objects of different clusters are *far apart* or very different.

To achieve global optimality in partitioning-based methods clustering would require the exhaustive enumeration of all of the possible partitions. Combinatorial search of the set of possible partitions for an optimum value of a criterion is clearly computationally prohibitive. Instead, most applications adopt heuristic methods, such as the K-means algorithm, where each cluster is represented by the mean value of the objects in the cluster. In practice, therefore, the algorithm is typically run multiple times with different starting states, and the best configuration obtained from all of the runs is used as the output clustering.

- **Hierarchical methods:** These methods create a hierarchical decomposition of the given set of data objects. A hierarchical method can be classified as being either *agglomerative* or *divisive*, based on how the hierarchical decomposition is formed. The *agglomerative approach*, also known as *bottom-up* approach, starts with each object forming a separate group. It successively merges the objects or groups that are closer to one another, until all of the groups are merged into one (the topmost level of the hierarchy), or until a termination condition holds. The *divisive approach*, also called the *top-down* approach, starts with all objects in the same cluster. In each successive iteration, a cluster is split up into smaller clusters, until eventually each object is one cluster or until a termination condition holds.

  Hierarchical methods suffer from the fact that once a step (merge or split) is done, it can never be undone. This rigidity is useful in that it leads to smaller computation costs by not having to worry about combinatorial number of different choices. However, such techniques cannot correct erroneous decisions.

- **Density-based methods:** Most partitioning methods cluster objects are based on the distance between objects. Such methods can find only spherical-shaped clusters and encounter difficulty at discovering clusters of arbitrary shapes. Other clustering methods have been developed based on the notion of *density*. Their general idea is to continue growing the given cluster as long as the density (number of objects or data points) in the *neighborhood* exceeds some threshold; that is; for each data point within a given cluster, the neighborhood of given radius has to contain at least a minimum number of points. Such a method can be used to filter out noise (outliers) and discover clusters of arbitrary shape.

- **Grid-based methods:** Grid-based methods quantize the object space into a finite number of cells that form a grid structure. All the clustering operations are performed on the grid structure (i.e., on the quantized space). The main advantage

of this approach is its fast processing time, which is typically independent of the number of data objects and dependent only on the number of cells in each dimension in the quantized space.

- **Model-based methods:** Model-based methods attempt to optimize the fit between the given data and some mathematical model. Such methods are often based on the assumption that the data are generated by a mixture of underlying probability distributions.

Data abstraction is the process of extracting a simple and compact representation of a data set. A cluster of data objects (patterns) can be treated collectively as one group and so may be considered as a form of data compression. In the clustering context, a typical data abstraction is a compact description of each cluster, usually in terms of cluster prototypes or representative patterns such as the centroid.

Cluster validity analysis, is the assessment of a clustering procedure's output. Often, this analysis uses a specific criterion of optimality. One approach is based in relative tests which compare two structures and measures their relative merit, aiming to find the best clustering solution that a clustering algorithm can define. The idea is the evaluation of a clustering structure by comparing it to other clustering schemes, resulting by same algorithm (and the same input data) but with different parameter values.

4.2. Clustering of the Multipath Radio Channel Parameters

With respect to the problem of clustering the radio channel parameters, each MPC is seen as a pattern or data object. In this context, the K-means algorithm has been used frequently. As mentioned in section 4.1, this algorithm belongs to the group of the so-called partitioning algorithms. As also mentioned before, in [86] a version of this algorithm is referred as *KPowerMeans* (KPM) because it also considers the power of the multipath components when performing the grouping. In [87] the Fuzzy-c-means algorithm is investigated as an alternative to the K-means and also the performance of different initialization approaches. This study concludes that under random initialization the Fuzzy-c-means algorithm outperforms the KPM algorithm, but if deterministic initialization is used both algorithms perform in a similar manner.

Throughout this section and the next, the required tools for the establishment of a complete clustering framework are presented. Performance evaluation and eventual adjustments are presented in section 4.4.

4.2.1. MPC Distance

As discussed above (section 4.1), clustering algorithms require a measure to evaluate pattern similarity or dissimilarity between a given pair of patterns, MPCs in this context. Therefore, a measure for distance calculation between two MPCs is required. The data set is multidimensional and data in different dimensions presents distinct units (as time and angles, the latter presenting also the periodicity problem). This problem has been efficiently solved in [88] introducing the multipath component distance (MCD) which normalizes and scales the data in each dimension and also solves the angular ambiguity problem. MCD is computed as the Euclidean norm of a vector having as coordinates the normalized distances in each domain: delay and angle.

For delay, the distance between two MPCs is defined as the normalized absolute distance between the corresponding delays, scaled by the normalized standard deviation of the delays and an additional *delay scaling factor* (DSF), ζ, which is used to control the importance of the delay domain on the overall MCD.

The delay distance is thus given by

$$\mathrm{MCD}_{\tau,ij} = \zeta \frac{\left|\tau_i - \tau_j\right|}{\Delta\tau_{\max}} \frac{\tau_{\mathrm{std}}}{\Delta\tau_{\max}}, \tag{4.3}$$

where $\Delta\tau_{\max} = \max_{ij}\left\{\left|\tau_i - \tau_j\right|\right\}$ and τ_{std} is the standard deviation of the delays [88].

The angular distance between two MPCs is defined as

$$\mathrm{MCD}_{\mathrm{DoA},ij} = \frac{1}{2}\left\| \begin{bmatrix} \sin(\beta_i)\cos(\phi_i) \\ \sin(\beta_i)\sin(\phi_i) \\ \cos(\beta_i) \end{bmatrix} - \begin{bmatrix} \sin(\beta_j)\cos(\phi_j) \\ \sin(\beta_j)\sin(\phi_j) \\ \cos(\beta_j) \end{bmatrix} \right\|. \tag{4.4}$$

Note that $\mathrm{MCD}_{\mathrm{DoA},ij}$ is vector-valued and that the length of the vector, i.e, $\left\|\mathrm{MCD}_{\mathrm{DoA},ij}\right\|$, is proportional (one half) to the distance between the two associated unit vectors pointing towards the directions defined by each MPC. The maximum that $\left\|\mathrm{MCD}_{\mathrm{DoA},ij}\right\|$ may present is 1 unit for the case of two collinear DoAs pointing in opposite directions.

The overall MCD is expressed as

$$\mathrm{MCD}_{ij} = \sqrt{\left(\mathrm{MCD}_{\tau,ij}\right)^2 + \left\|\mathrm{MCD}_{\mathrm{DoA},ij}\right\|^2}. \tag{4.5}$$

The delay-part of this measure is in the interval $[0,\zeta]$ and the angular-part is in the interval $[0,1]$, but do not necessarily touch these boundaries. All parameter dimensions are

normalized, therefore this distance metric is suitable for joint clustering of the multipath radio channel parameters.

4.2.2. KPM Algorithm

Regarding the clustering of multipath radio channel parameters, the inputs to the chosen algorithm are the desired number of clusters, *K*, and the parameters of all multipath components. The data can be structured in an $L \times N$ matrix where L is the number of multipath components and N is the number of parameters available for each component: *delay*, *azimuth*, and *power*. The algorithm's output is a class label vector containing a cluster index for each channel component.

Consider the following notation: L is the total number of MPCs; each single MPC is characterized by its power, P_ℓ and a parameter vector $s_\ell = [\tau_\ell, \phi_\ell]$ containing the delay, τ_ℓ and the azimuth ϕ_ℓ; K represents the number of clusters; k is the index of a given cluster; L_k is the number of MPCs belonging to cluster k and c_k is the centroid position of k-th cluster.

For fuzzy schemes, the output of the cluster algorithm is a membership matrix denoted as $\mathbf{U} = [u_{k\ell}]$, $k = 1, \cdots, K$ and $\ell = 1, \cdots, L$, where $u_{k\ell} \in [0,1]$ represent the degree of membership of the ℓ-th MPC to the k-th cluster and verify the following condition

$$\sum_{k=1}^{K} u_{k\ell} = 1 . \tag{4.6}$$

The output of a hard partitioning scheme may also be expressed by the membership matrix, **U**, if the following condition holds

$$u_{k\ell} = \begin{cases} 1 & \ell\text{-th MPC in } k\text{-th cluster} \\ 0 & \text{otherwise} \end{cases} ; \tag{4.7}$$

meaning that in hard clustering each MPC may belong to only one cluster.

For a given number, *K*, of desired clusters the KPM algorithm runs as follows:

1- *Initialization*: calculate the starting positions of the clusters' centroids.

2- For *i* = 1 to *MaxIterations*

   a. Create the data partition by assigning each MPC to the nearest cluster (centroid).

   b. Update each cluster's centroid as being the center of the group of MPCs belonging to the given cluster (**power weighted average** in each dimension).

   c. If no movement of clusters' centroids Go To step 3.

3- Return the class label vector.

The KPM algorithm determines, iteratively, the cluster centroids in order to minimize the total sum of distances of each multipath component to the respective centroid. The *k*-th cluster centroid (computed in step 2-b) is denoted as $c_k = [\tau_{ck}, \phi_{ck}]$, where

$$\tau_{ck} = \frac{\sum_{\ell \in c_k} P_\ell \cdot \tau_\ell}{\sum_{\ell \in c_k} P_\ell}, \tag{4.8}$$

and

$$\phi_{ck} = \frac{\sum_{\ell \in c_k} P_\ell \cdot \phi_\ell}{\sum_{\ell \in c_k} P_\ell}. \tag{4.9}$$

Therefore, the centroid can be seen as the center of mass of a given cluster as it is computed as the **power weighted average**, in each dimension, of the components composing the cluster.

Note that when calculating the azimuth of the cluster centroid, attention should be paid on the angles ambiguity [89]. For this purpose, consider ϕ_k being the vector containing the azimuths of MPCs belonging to the *k*-th cluster, expressed in the interval $[-\pi, \pi]$. Let this vector to be split into: ϕ_{kn} containing $\phi_k < 0$ and ϕ_{kp} containing $\phi_k \geq 0$. The azimuth power weighted average, expressed in equation (4.9), may be conveniently computed by

$$\phi'_{ck} = \frac{\sum_{\ell \in kn} P_{kn} \cdot \phi_{kn} + \sum_{\ell \in kp} P_{kp} \cdot \phi_{kp}}{\sum_{k=\{\ell \in c_k\}} P_k} = \mu_{kn} \frac{\sum_{\ell \in kn} P_{kn}}{\sum_{k=\{\ell \in c_k\}} P_k} + \mu_{kp} \frac{\sum_{\ell \in kp} P_{kp}}{\sum_{k=\{\ell \in c_k\}} P_k}, \tag{4.10}$$

where

$$\mu_{kn} = \frac{\sum_{\ell \in kn} P_{kn} \cdot \phi_{kn}}{\sum_{\ell \in kn} P_{kn}} \text{ and } \mu_{kp} = \frac{\sum_{\ell \in kp} P_{kp} \cdot \phi_{kp}}{\sum_{\ell \in kp} P_{kp}}. \tag{4.11}$$

Therefore, μ_{kn} and μ_{kp} are, respectively, the power weighted averages of negative and nonnegative angles. In order to solve the ambiguity, which arises if $\mu_{kp} - \mu_{kn} > \pi$, let

$$\mu'_{kn} = \begin{cases} \mu_{kn} + 2\pi & \text{if } \mu_{kp} - \mu_{kn} > \pi \\ \mu_{kn} & \text{otherwise} \end{cases}. \tag{4.12}$$

Thus, ϕ'_{ck} comes

$$\phi'_{ck} = \mu'_{kn} \frac{\sum_{\ell \in kn} P_{kn}}{\sum_{k=\{\ell \in c_k\}} P_k} + \mu_{kp} \frac{\sum_{\ell \in kp} P_{kp}}{\sum_{k=\{\ell \in c_k\}} P_k}. \tag{4.13}$$

Finally, to ensure ϕ_{ck} in the interval $[-\pi, \pi]$,

$$\phi_{ck} = \begin{cases} \phi'_{ck} & \text{if } \phi'_{ck} \le \pi \\ \phi'_{ck} - 2\pi & \text{otherwise} \end{cases}. \tag{4.14}$$

Depending on the selected criteria to evaluate the distance between one MPC and a given centroid, the algorithm may reach different solutions. MCD is used as the basic distance measure, but when computing distances seeking the assignment of a given MPC to a cluster (step 2-a), the distance measure is the result of **MCD weighted with the corresponding MPC power**, i.e, the cost function given by

$$d_{\ell,ck} = P_\ell \cdot \mathrm{MCD}(s_\ell, c_k), \tag{4.15}$$

when minimized determines the allocation of the ℓ-th MPC to the *k*-th cluster. Inclusion of power into the distance function is advantageous as clusters focus on and try to distinguish the strongest MPCs, usually the most relevant in the channel behavior and description.

Concerning the KPM initialization, it is common to choose the first set of centroids randomly from the data. Nevertheless, random initialization requires running the clustering algorithm several times, for the same desired number of clusters, *K*, in order to obtain the best solution. In [90] a deterministic approach, is proposed which is also used in [87]. This method uses log-power weighted MCD to compute distances and also tries to identify, at this stage, the number of clusters present in the data set, K_{opt}. However, as will be discussed below (section 4.4.1), this procedure prevents placing initial centroids in

multipath components with less power and, thus, even when K is the actual number of clusters in the data set, K_{true}, the KPM is unable to reach the correct solution. In this work, at initialization stage MCD is not power weighted, therefore, the initialization procedure consists:

1- choose the MPC having the strongest power to be the first centroid,

2- repeat:

   a. for each MPC, obtain the minimum distance to the centroids available (here **MCD is not power weighted**)

   b. choose the MPC having the maximum distance to be next centroid

   until the desired number of centroids, K, is reached.

The idea is to spread the centroids over all the data. After the first round of MPCs assignment, due to the power weighted average used to compute the centroids locations (step 2-b of KPM) they move rapidly to places where the strongest MPCs are located.

Furthermore, the number of clusters, present in a given data set, is not estimated in the initialization step. Instead, as explained bellow, it is estimated by running the clustering algorithm for several candidate numbers of clusters and then, by employing cluster validity indices.

4.3. Clustering Validation

As discussed above, the KPM algorithm requires, as input, the desired number of clusters, K, to perform the data partition. The number of clusters is naturally known if we are considering synthetic data. However, if we are dealing with experimental data we must find out the number of clusters present in the data using an objective criterion. The best solution (K_{opt}) may be selected by a Cluster Validity Index (CVI). A CVI should be able to rank the different clustering solutions in terms of their *goodness*: it measures numerically, for each solution, properties as *compactness* or *clusters separation*.

Nevertheless, each cluster validity index captures a particular feature of the solution while other features may be disregarded or given less importance. Thus, depending on the chosen index different solutions may be reached. There are many indices available in the literature, and several studies on performance comparison [91] show that there is no index which outperforms all the others. Therefore, improvements on the estimation of K_{opt} may

be achieved if several indices are combined as suggested in [92]. The idea is to reach a trade-off solution, potentially more robust.

4.3.1. Validation Indices

This section presents four well-known CVIs among the community of clustering practitioners: *Xie-Beni*, *Calinski-Harabasz*, *PBM* and *Generalized Dunn's* indices, which will be defined afterwards. Mathematical formulations presented below consider the notation introduced in section 4.2.2 and assume also the MCD as the distance measure.

Xie-Beni (XB) index: *XB* index has been presented in [93] and for a given clustering solution, it represents the ratio of the clusters' compactness to the clusters' separation. Mathematically, this index is expressed as

$$v_{XB} = \frac{\sum_{k=1}^{K}\sum_{\ell=1}^{L} u_{k\ell}^2 \left(\mathrm{MCD}\left(s_\ell, c_k\right)\right)^2}{L \times \left[\min_{k1,k2}\left(\mathrm{MCD}\left(c_{k1}, c_{k2}\right)\right)\right]^2}. \tag{4.16}$$

By including the membership matrix, **U**, this index has been proposed to be suitable for cluster validation on fuzzy partitions, but it if $u_{k\ell}$ verifies equation (4.7) it is adequate to be used on hard partitions, as well [94, 95].

The optimal partition, K_{opt}, is obtained by minimizing the index. As *XB* is defined by a quotient, this corresponds to minimize the numerator and maximize the denominator. Note that numerator represents the sum of each MPC distance to the corresponding centroid that it belongs (assuming hard portioning of data), thus the smaller this sum is the more compact are the clusters. On the other hand, note that for a specific data set, *L* is a constant value and the remaining part of the denominator represents the minimum distance between two centroids (inter cluster distance), therefore the higher this minimum distance is the more separated the clusters are. Hence, *XB* index tries to identify the solution which presents the more compact and separated clusters.

Generalized Dunn's index: This index has been proposed in [96] as a generalization of the original Dunn's index with the objective of improving its sensitivity to aberrant data for the case when clusters are expected to be volumetric clouds (as opposed to boundaries or surfaces) in the feature space.

In a similar way as the original Dunn's index, its generalized version is defined as the quotient between a minimum distance involving two clusters (*set distance* – δ) and a maximum distance involving one cluster (*cluster diameter* – Δ), but considers several

alternative definitions for distance metric (six possibilities for set distance and three for cluster diameter). Using δ_i and Δ_j the generalized Dunn's index is defined by

$$\nu_{Dij} = \frac{\min\limits_{\substack{k1,k2 \\ k1 \neq k2}} \delta_i\left(k1,k2\right)}{\max\limits_{k} \Delta_j\left(k\right)} \tag{4.17}$$

where $1 \leq i \leq 6$ and $1 \leq j \leq 3$. Depending on the functional forms used to define δ_i and Δ_j it may present 18 different forms. Results presented in [96] show that one of the most successful forms is D_{53}, with δ_5 and Δ_3 defined as

$$\delta_5 = \frac{1}{L_{k1} + L_{k2}} \left(\sum_{\ell=1}^{L_{k1}} \mathrm{MCD}\left(s_\ell, c_{k1}\right) + \sum_{m=1}^{L_{k2}} \mathrm{MCD}\left(s_m, c_{k2}\right) \right) \tag{4.18}$$

and

$$\Delta_3 = 2\left(\sum_{\ell=1}^{L_k} \mathrm{MCD}\left(s_\ell, c_k\right) \right) \tag{4.19}$$

respectively. Likewise the *XB* index, D_{53} also attempts to recognize clustering solutions that are compact, i.e., presenting small cluster diameters and well separated, i.e., high set diameters. Thus, contrasting with *XB*, K_{opt} is specified by the maximum value of the D_{53} index.

Calinski-Harabasz (CH) index: It is formulated as [94]

$$\nu_{CH} = \frac{\left[\dfrac{\sum_{k=1}^{K} L_k \left(\mathrm{MCD}\left(c_k, c_0\right) \right)^2}{K-1} \right]}{\left[\dfrac{\sum_{k=1}^{K} \sum_{\ell=1}^{L_k} \left(\mathrm{MCD}\left(s_\ell, c_k\right) \right)^2}{L-K} \right]}, \tag{4.20}$$

where c_0 is the global centroid of the entire data set, which may be computed using equations (4.8) to (4.14).

The numerator of *CH* index represents a *between-cluster scatter measure*, i.e., a function involving inter-cluster parameters which measures the spreading (separation) of the clusters; while the denominator represent a *within-cluster scatter measure*, i.e., a function involving only MPCs and the centroid of a given cluster aiming to quantify the clusters compactness. Thus, the solution exhibiting the more compact and separated clusters maximizes *CH* index and specifies K_{opt}.

PBM index: This index has been developed in [94] for hard clustering and is formulated as

$$v_{PBM} = \left(\frac{1}{K} \times \frac{\max_{k1,k2} \left(\mathrm{MCD}\left(c_{k1}, c_{k2} \right) \right)}{\sum_{k=1}^{K} \sum_{\ell=1}^{L_k} \mathrm{MCD}\left(s_\ell, c_k \right)} \right)^2 . \tag{4.21}$$

K_{opt} is indicated by maximum value of *PBM* index. A formulation suitable for fuzzy partitioning methods is presented in [95].

PBM index may be viewed as the product of two factors. The first factor decreases with increasing *K*. The numerator of the quotient representing the second factor, measures the maximum separation between a pair of clusters and increases with *K*. It is desirable to increase this contribution as possible in order to have the best inter-cluster separation. Note that this value is bounded up by the maximum separation between two points in the data set. The denominator of the same quotient represents the sum of all intra-cluster distances. It is desirable to minimize this measure in order to provide compact clusters. This may be achieved by increasing *K*. Thus the second factor increases with *K*, and supports solution with higher values of *K*. However, while the second factor is increasing with *K*, the first factor is diminishing, leading to the identification of the data partition which presents increased cluster compactness and cluster separation while keeping the number of clusters as small as possible.

4.3.2. Fusion Techniques

Given a set of data partitions, each cluster validity index tries to identify which one is the best. Nevertheless, each index uses a different strategy, thus depending on the chosen index a different solution may be selected. As mentioned before, improvements on the estimation of K_{opt} may be achieved if several indices are combined trying to attain a trade-off solution, potentially more robust. In this work, two strategies taken from [92], have been considered to accomplish the fusion of indices: *score* and *decision rank* fusion methods.

A *score fusion* method is defined as a mathematical operation involving several independent indices (e.g., their arithmetic mean), resulting in a combined score. Thus, to obtain sensible results, it is necessary to normalize the indices involved to a common range of values, before computing the score. The selected scheme for normalization was min-max[5], which scales each index to the [0,1] range. Moreover, as presented in the

[5] Given an observation vector $\mathbf{x} = [x_1, \cdots, x_N]$, min-max normalization of $\mathbf{x}$ is obtained by $\mathbf{x}' = \frac{\mathbf{x} - x_{\min}}{x_{\max} - x_{\min}}$.

previous section, the *XB* index specifies K_{opt} by minimization, whereas the other three show a maximum for the best solution. To achieve index consistency, after min-max normalization, $1-\nu_{XB}$ has been used for fusion purposes (to ensure that *XB*, as other indices considered, indicates the best clustering partition through a maximum value).

Score Fusion Methods: Assuming that *M* indices are available, the following combined measures defined in [92] were considered

$$\text{SF-A}(k) = \frac{1}{M}\sum_{i=1}^{M} \nu_i(k), \tag{4.22}$$

$$\text{SF-G}(k) = \left(\prod_{i=1}^{M} \nu_i(k)\right)^{1/M}, \tag{4.23}$$

and

$$\text{SF-Med}(k) = \text{median}\left(\{\nu_1(k),\ \nu_2(k),\ \ldots,\ \nu_M(k)\}\right). \tag{4.24}$$

These combined measures represent, respectively, the arithmetic mean, the geometric mean and the median of the indices selected to be combined. In [92] a scheme defined by using the harmonic mean is also presented.

Decision Rank Fusion Method (Kr): In addition to the fusion methods above, a rank-based scheme is now introduced which is similar to a voting scheme: each index creates a ranking for the available clustering solutions where the worst solution gets one point, then each solution in the rank gets one point more than the previous one and, finally, the best solution gets two points more than the previous one. After that, the scores given to each clustering solution, by each index, are summed to obtain the combined score. The solution exhibiting the highest score indicates K_{opt}.

4.4. Clustering Results using Synthetic DCIRs

This section presents results on the performance evaluation of the KPM algorithm and also of the cluster validity indices. First, preliminary results were convenient to validate the clustering scheme, namely the initialization procedure and the distance metric used by the algorithm (a similar study has been presented in [97]). Afterwards, a more detailed and structured study has been carried out in order to assess the quality of the clustering solution which has been reached when the algorithm is provided with $K=K_{true}$ and also, to assess the accuracy of the cluster validity methods (individual indices and fusion schemes).

For this purpose, synthetic data were generated using the Extended Saleh-Valenzuela model [48]. For preliminary tests a few data sets were generated while for the subsequent

studies several sets of data were generated with the actual number of clusters, K_{true}, ranging from 3 to 10: for each value of K_{true}, 1000 data sets were generated and for each set, a set of possible clustering solutions were obtained by running the KPM algorithm with K varying from 2 to 11.

4.4.1. Preliminary Evaluation of the Clustering Framework

KPM Algorithm and Initialization

Figure 4-1 shows one of data sets generated (among the few sets generated for preliminary tests). This particular data set presents 7 clusters (i.e., K_{true}=7), which are distinguished by different markers. A set of possible data partitions were collected by running the KPM algorithm for K varying from 2 up to 11.

Figure 4-2 compares the final clustering solutions obtained, by the KPM algorithm for K=7 (i.e., K=K_{true}), for two different initialization approaches: in the left-side of Figure 4-2 MCD is not power weighted as proposed in section 4.2.2 and in the right-side of the same figure MCD is power weighted as suggested in [90] (also used in [87]).

As it may be observed, the solution in left-side of Figure 4-2 is very similar to the real data set. Only 2 MPCs were incorrectly assigned to the yellow cluster (left triangles in Figure 4-1) that should belong to the green cluster (diamonds in Figure 4-1). These two MPCs are less distant to the yellow cluster than to the green one, thus more similar to MPCs that belong to the yellow cluster. Therefore, the solution is perfectly acceptable. In addition, if the data partition obtained for K=8 is inspected, it can be concluded that the new cluster is composed only by the squared-shaped MPC (Figure 4-1), that is remotely isolated from the others in the same cluster. Given this particularity of the data set, at least visually, this solution seems to be equally acceptable.

On the other hand, by observing the clustering solution in the right-side of Figure 4-2, which used power weighted MCD at the initialization, it may be concluded that for K=K_{true} (7 in this case), the KPM algorithm is unable to reach the correct solution: clusters with several strong components are subdivided into smaller clusters and clusters composed by components with less power are grouped into macro-clusters.

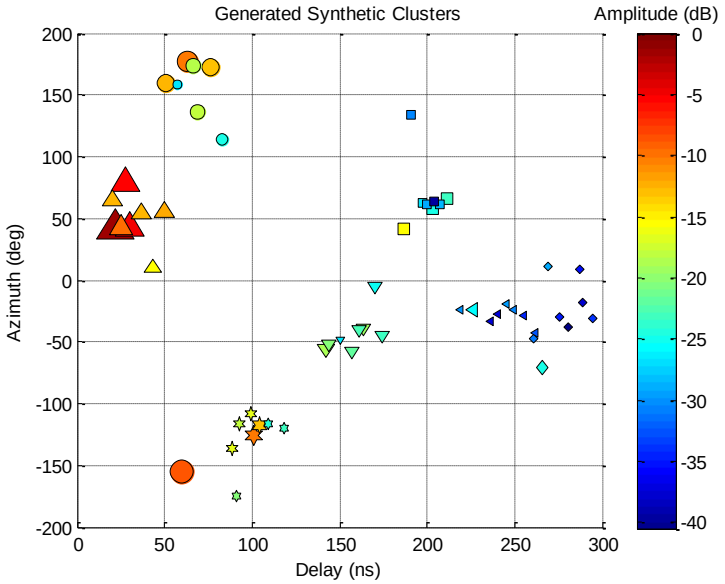

Figure 4-1: Sample of a synthetic channel generated, using the ESV model, with 7 clusters and 8 MPCs per cluster.

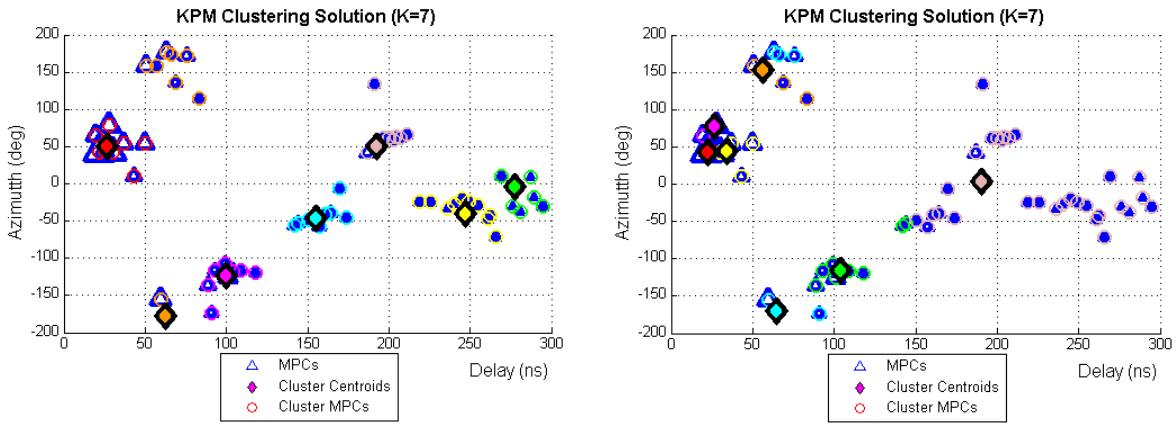

Figure 4-2: Comparison of final KPM partitions for K=7 using different initialization strategies. **Left:** MCD without power weight. **Right:** MCD with power weight.

To understand these results, the initial states used by the KPM algorithm provided by each initialization scheme are compared in Figure 4-3. It is apparent, that the initialization scheme proposed in [90], which uses MCD power weighted (right-side of Figure 4-3), prevents placing initial centroids in MPCs with less power, as is the case of the diamond and left triangle shaped clusters in Figure 4-1. Contrariwise, initial centroids tend to be concentrated on the MPCs with more power, and as a consequence, the KPM performance is substantially affected because once the centroids are placed in those stronger MPCs, these components will hold the centroids nearby and they cannot move near to MPCs with less power.

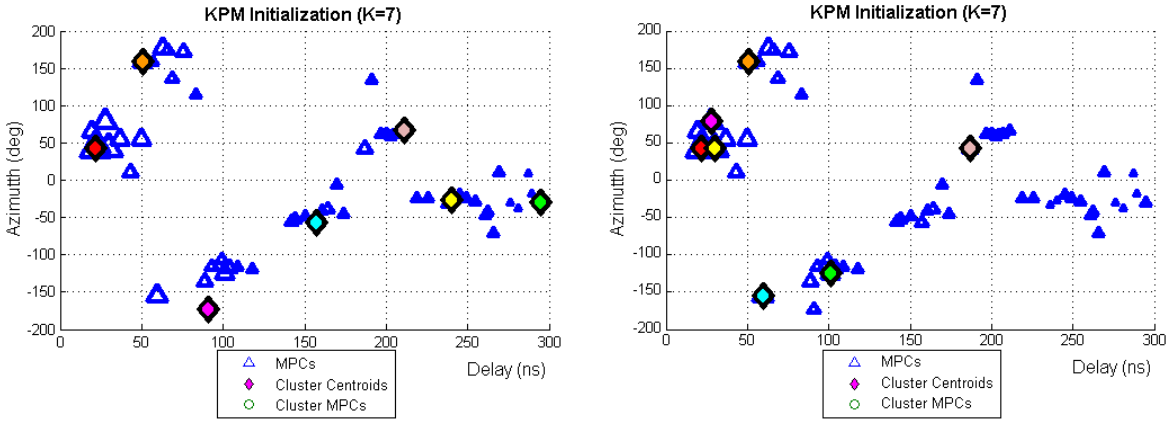

Figure 4-3: Comparison of initialization strategies.
Left: MCD without power weight. **Right:** MCD with power weight.

In contrast, if, in the initialization, MCD is not power weighted (left-side of Figure 4-3), initial centroids are more spread over all the data. Afterwards, within a few iterations, the centroids are dragged to near the components having more power (due to the power weighted average used in the centroids update). These results lead to the conclusion that this initialization procedure is the most adequate.

Cluster Validation

Figure 4-4 presents the results of validation indices (in the left-side) and of combined techniques (in the right-side) for each KPM clustering solution, still considering the data set of Figure 4-1. For each measure, the selected K_{opt} is highlighted by a red circle.

In this case, only *CH* index is able to identify K_{opt} correctly, but for D_{53} index solutions with K=7 or K=8 present almost the same score meaning that are both equally good. For *PBM* index K=7 is identified as the second best solution and for *XB* index it scores the fourth place. As for the contemplated fusion techniques, results show that all techniques were able to identify K_{opt}=7, which is correct number of cluster in the data set, despite not all individual indices estimated in this value for K_{opt}. These results show that combining individual validation indices is a viable way of increasing the robustness and accuracy on the estimation of the number of clusters, when compared to the use of a single validation index.

Furthermore, it may be observed (right-side of Figure 4-4) that all the three score fusion-based methods studied (SF-A, SF-G and SF-Med) present very similar behavior and thus, very similar results. Consequently, in the structured study presented below only SF-G, based in the geometric mean, has been considered.

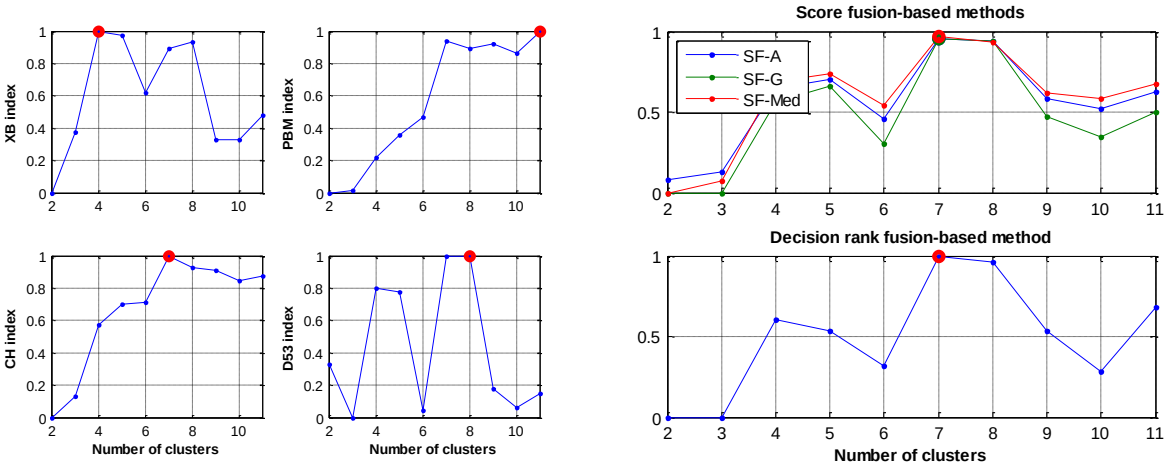

Figure 4-4: Cluster Validation for the data set of Figure 4-1 (K_{true}=7) with K_{opt} highlighted by a red circle. **Left:** Individual indices results. **Right:** Fusion techniques results.

4.4.2. Structured Evaluation of the Clustering Framework

Generate and analyze just a few data sets is useful to have a valuable and perhaps indispensable visual picture on the behavior and on the internal functioning mechanisms of the algorithm. However, such a study may not reflect rigorously the accuracy of methods under evaluation.

In order to accomplish a more structured study, a large number of data sets should be generated and analyzed. With this objective, 8×1000 data sets were generated: 1000 data sets for each K_{true}, with K_{true} ranging from 3 to 10. For each data set 10 possible clustering solutions were obtained by running the KPM algorithm with K varying from 2 to 11. During the data generation process, some preventive measures were introduced to avoid the creation of data sets presenting overlapping clusters or multipath components identified as outliers.

Yet, analyzing a large number of data sets by examining each one individually is not practicable, thus such a task must be mechanized. The analysis approach is explained below.

KPM Algorithm Accuracy

The KPM algorithm accuracy has been assessed by evaluating if, for K=K_{true}, it is able to find correct solution, i.e., if the KPM solution found (with K=K_{true}) acceptably resembles the real data partition. This verification has been made by comparing the position of the centroids in the data set with those presented in the KPM solution obtained for K=K_{true}: if

position match for all centroids is achieved it is considered that KPM had succeeded in finding the correct solution.

Figure 4-5 presents KPM success rates for all K_{true} values considered. It can be observed that, as K_{true} increases the KPM accuracy slightly decreases. This may be explained because, as K_{true} increases, the complexity of the problem also increases (more degrees of freedom). Nevertheless, the success rate was always higher than 70% and, thus, it may be concluded that KPM accomplishes the clustering task suitably.

Performance of Individual Indices (CVIs)

Each validation index analyses, compares and selects one solution among all candidate solutions found by the KPM algorithm. A given index has succeeded in finding the correct number of clusters if the selected solution, K_{opt}, matches the actual number, K_{true}. However, to guarantee a fair evaluation of each index, the success or failure rates (presented below) were obtained considering only the cases where KPM succeeded in finding the correct solution.

Figure 4-6 shows the success rate for the indices presented above (section 4.3.1). From this figure we can conclude that *PBM* shows a poor performance, particularly for the smaller values of K_{true}: the average success rate for *PBM* was 9.6%. We can also see that *CH* presents a very good performance for K_{true}=10, but not so good performances for smaller values of K_{true} with an average success rate of 28%. Both these two indices include a penalty factor with increasing *K*, to prevent the overestimation of *K*, however it seems not to be working in this kind of data sets.

On the other hand, *XB* and *D53* present stable performances, almost independent of K_{true}, with average success rates of 55.3% and 53.1% respectively. According to these results, it has been decided to use only these two indices in further investigations involving the fusion techniques mentioned above (section 4.3.2).

In addition, the type of failure, i.e., under or overestimation, has also been investigated. Thus, Figure 4-7 characterizes the underestimation and overestimation rates, for *XB* and *D53* only. We can observe that both indices present a similar behavior: the underestimations (average rate of 40.0% for *XB* and 42.9% for *D53*) are always more frequent than the overestimations (4.7% for *XB* and 4.0% for *D53*).

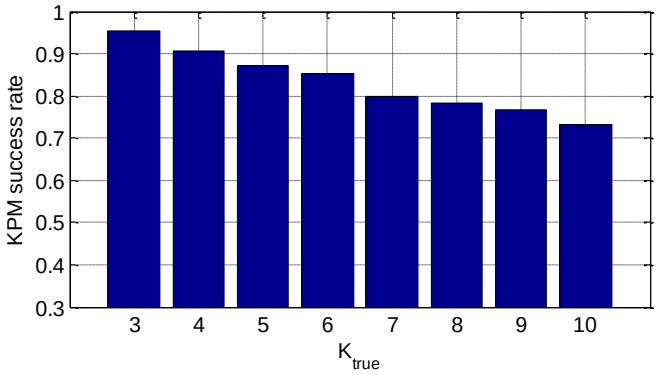

Figure 4-5: KPM success rate.

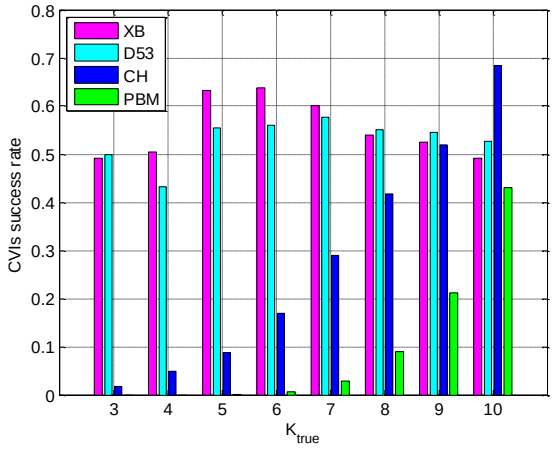

Figure 4-6: CVI success rates.

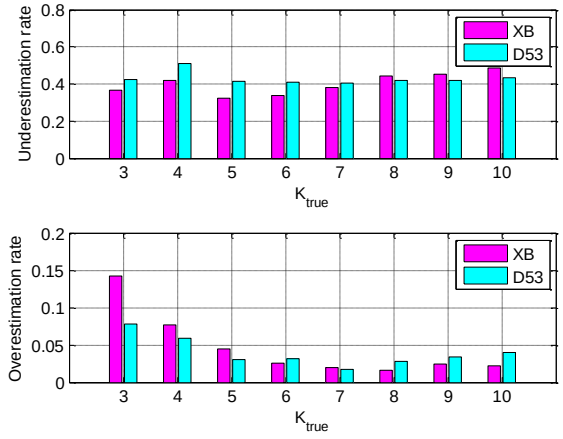

Figure 4-7: Underestimation and overestimation rates for XB and D53.

Performance of Fusion Techniques

According to the results of individual validation indices, presented in the previous section, *XB* and *D53* indices were selected to employ with the fusion methods under investigation.

Figure 4-8 presents the success rates of the considered fusion techniques together with those for the *XB* and *D53* indices (for ease of comparison). Observing this figure, we may conclude that the *score fusion* method considered, SF-G, is always better than that of, at least one of the individual indices (better than *D53* for K_{true}=[4, 5, 6] and better than both for the remaining cases). However the improvement is not very significant.

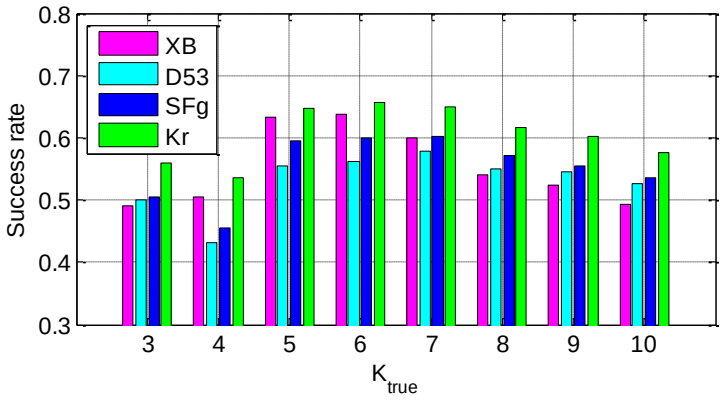

Figure 4-8: Fusion techniques success rate.

Regarding the suggested *decision rank fusion* method, we can conclude that this method always outperforms all individual indices and also outperforms SF-G. Performance improvement is particularly evident and significant for K_{true}=[3, 7,..., 10], representing the majority of the cases studied.

4.5. Summary of the Clustering Framework

In the previous section an evaluation of the several clustering related tools, presented throughout sections 4.2 and 4.3, has been carried out. Frequently, several alternate options were available and sometimes some adjustments had been introduced. In this section the clustering framework, thereby achieved, is briefly summarized. Though potentially independent, four interrelated steps play an important role in the global framework and consequently influence substantially the final results: clustering approach, distance function, initialization of the algorithm, clustering validation.

The KPM algorithm is used as the underlying clustering algorithm with the power weighted MCD distance to measure distances between MPCs and centroids (both presented in section 4.2).

The initialization procedure uses MCD distance to measure distances between MPCs, but, as explained, in this step MCD is not power weighted. This scheme has the advantage of spreading centroids over all the data, letting power pull the centroids near to the MPCs with more power at the stage of centroids updating. In data sets analyzed, this procedure has revealed to be more adequate allowing the KPM algorithm to find the right solution when the requested number of clusters matches the true number of clusters. Otherwise, the

clusters having several strong MPCs are subdivided in smaller clusters and clusters composed of MPCs with less power are grouped together in a macro-cluster.

The actual number of clusters was known as the data was synthesized using a cluster-based propagation model, but, for experimental data the number of clusters need to be found. Four cluster validity indices, available in the literature, were investigated. These indices address the problem by comparing data partitions with different number of clusters. Results show that none of the indices is able to always predict correctly the desired number of clusters. From the four indices studied, *XB* and *D53* presented the best results with similar performances. Two fusion techniques were also presented. Results confirmed that improvements over those of single indices can be achieved. The best seems to be the decision rank fusion scheme (Kr) proposed in this work and already published in [98]. Therefore, *XB* and *D53* indices and the Kr fusion scheme were selected to employ in the analysis of experimental data.

By congregating all, a framework has been envisaged which is suitable to be applied to experimental DCIRs estimated from measured data, as those presented in chapter 3. This framework may be schematized as follows in two main steps:

1- For the given data set, run the KPM algorithm for $K = K_{\min},...,K_{\max}$, i.e., for several candidate numbers of clusters.

2- Apply clustering validity (*XB* and *D53* indices and *Kr* fusion scheme) to support the selection of the best data partition.

4.6. Clustering Results using Real DCIRs

A clustering framework has been presented and evaluated throughout sections 4.2 to 4.5. This section provides sample results obtained by this framework on the experimental DCRIs acquired in chapter 3. To establish a link with results presented in that chapter the clustering results for same measurement point will be presented.

Therefore, Figure 4-9 and Figure 4-10 show results which are corresponded with those in Figure 3-12 and Figure 3-13, respectively. Results of the selected cluster validity metrics appear on the left-side of these figures. The selected clustering solution, in the delay-azimuth plane, appear on the right-side of the same figures, where each MPC is represented by a blue triangle whose size is ruled by its power, circles with the same color

represent MPCs belonging to a given cluster and the diamond shaped marker with the same color represents the centroid of this cluster.

In the forward measurement (Figure 4-9) we can see that, for *XB* K_{opt}=6, for *D53* K=[5, 6] are equally good solutions and the rank fusion also suggests that K_{opt}=6. In the reverse measurement (Figure 4-10), all cluster validity metrics indicate K_{opt}=5, but, in order to establish a physical interpretation which links results from the forward and reverse measurements files, the clustering partition with K=6 clusters has also been the one which was chosen (see section 4.6).

In the next section a physical explanation for the clusters identified in each forward and reverse measurement pairs is attempted.

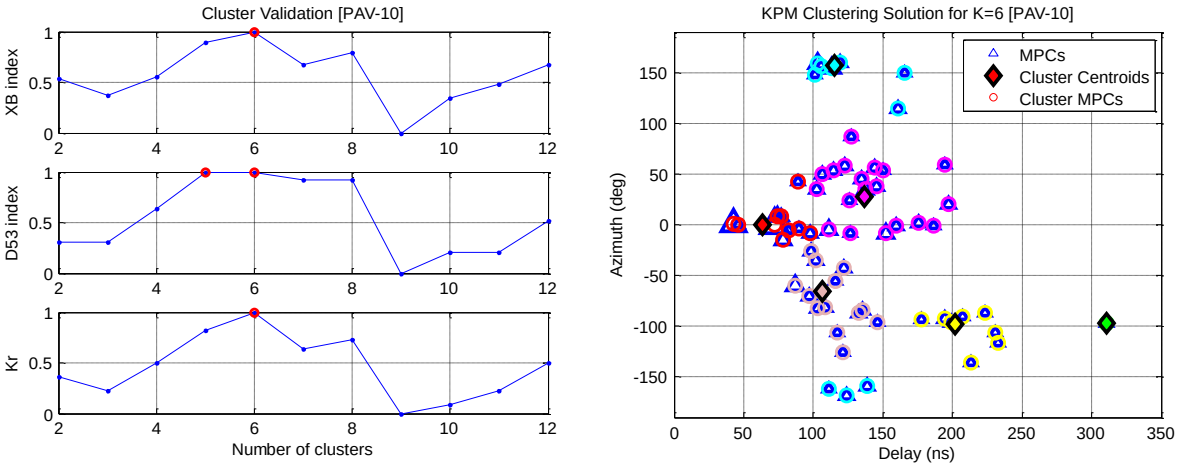

Figure 4-9: Forward Measurement [PAV-10] – **Left:** Cluster validity results for each KPM solution. **Right:** Clustering solution that was selected for this experimental data set.

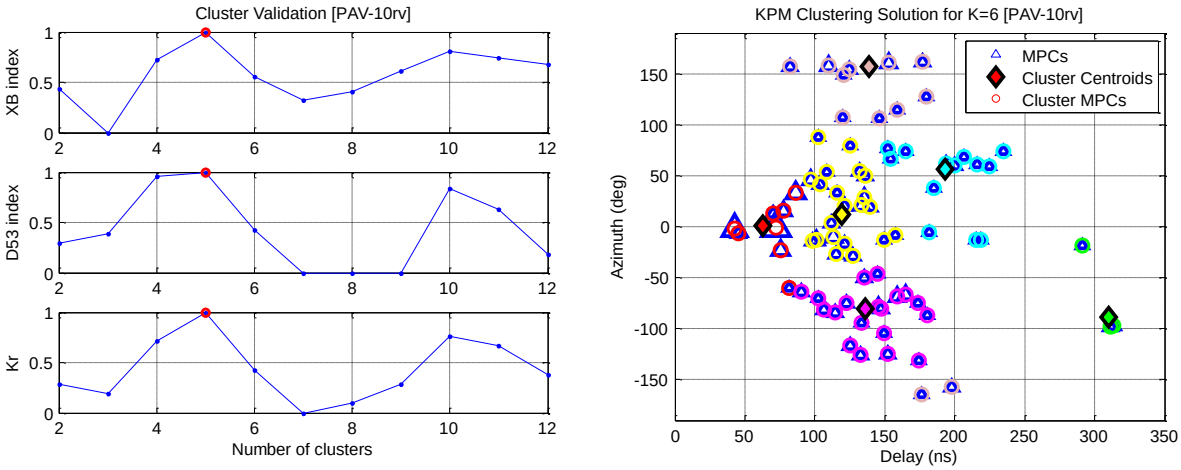

Figure 4-10: Reverse Measurement [PAV-10rv] – **Left:** Cluster validity results for each KPM solution. **Right:** Clustering solution that was selected for this experimental data set.

4.7. Physical Analysis of Clustered DCIRs

Trying to provide a physical interpretation for the clusters identified in each experimental DCIR and also to establish a linkage between each forward and reverse measurement pairs, further classification of the clusters was accomplished. This classification has been achieved by relating each cluster delay and azimuth to the objects in the scenario and by combining simultaneously the information of the two single-directional measurements, which compose one double-directional measurement.

This way, each cluster has been classified into one of the following types:

- **Type 0:** corresponds to the first cluster which contains the direct ray (possibly attenuated if non or obstructed line-of-sight conditions exist);
- **Type 1:** corresponds to clusters that represent a single interaction, i.e., clusters that present delay coincidence in both measurements and, in addition, the azimuth of these clusters matched to the same specific objects in the scenario;
- **Type 2:** corresponds to clusters that represent a higher order interaction, i.e., when reversing the measurement direction the channel also presents a contribution with the same delay but an azimuth match is not found with any specific object in the scenario;
- **Type 3:** corresponds to unexplained clusters, i.e., a delay contribution that is shown only in one direction of the double-directional measurement.

An illustration of the method employed for cluster classification is given bellow, but, similar results were also presented in [99].

In order to identify clusters (from the forward and reverse measurements) belonging to each of the types above, Figure 4-11 shows, overlaid in the scenario layout, the delay of each cluster (centroid), represented by an ellipse whose foci are the positions of the transmitter and the receiver, and the corresponding azimuths, represented by a line departing from the respective transceiver node to the intersection with the ellipse. Near this intersection there is a label to identify the cluster number and if it is a cluster from the forward measurement (e.g., F2) or from the reverse measurement (e.g., R2). Moreover, the same color has been used to represent similar delays. Azimuths of forward measurements correspond to DoAs and azimuths of reverse measurements correspond to DoDs (indeed, these were obtained as DoAs with the receiver placed in transmitter position and vice versa). The simplified scenario description (sports hall) is represented by black solid lines, where the larger rectangle represents the walls and the smaller rectangle represents the spectator seats.

The smaller ellipses (red: F1-R1) represent the first cluster, which includes the direct ray, are identified as type 0. These clusters correspond to the first ones represented, also in red, in Figure 4-9 and Figure 4-10, respectively.

The ellipses in magenta (R5-F5) – yellow cluster in Figure 4-9 and blue cluster in Figure 4-10 – despite a slight delay mismatch, correspond undoubtedly to a single interaction in the scenario wall, and, hence, these clusters are classified as type 1.

The larger ellipses (light green: F6-R6) – the most delayed clusters (also in green in Figure 4-9 and Figure 4-10) – illustrate the identification process for clusters type 2, where it is clearly shown that despite the delay of contributions present in forward and reverse direction is very similar, the corresponding DoD and DoA do not match only one specific object in the scenario, suggesting a higher order interaction. In this particular case, it may be easily confirmed that these clusters correspond to a double-bounce interaction in the scenario walls.

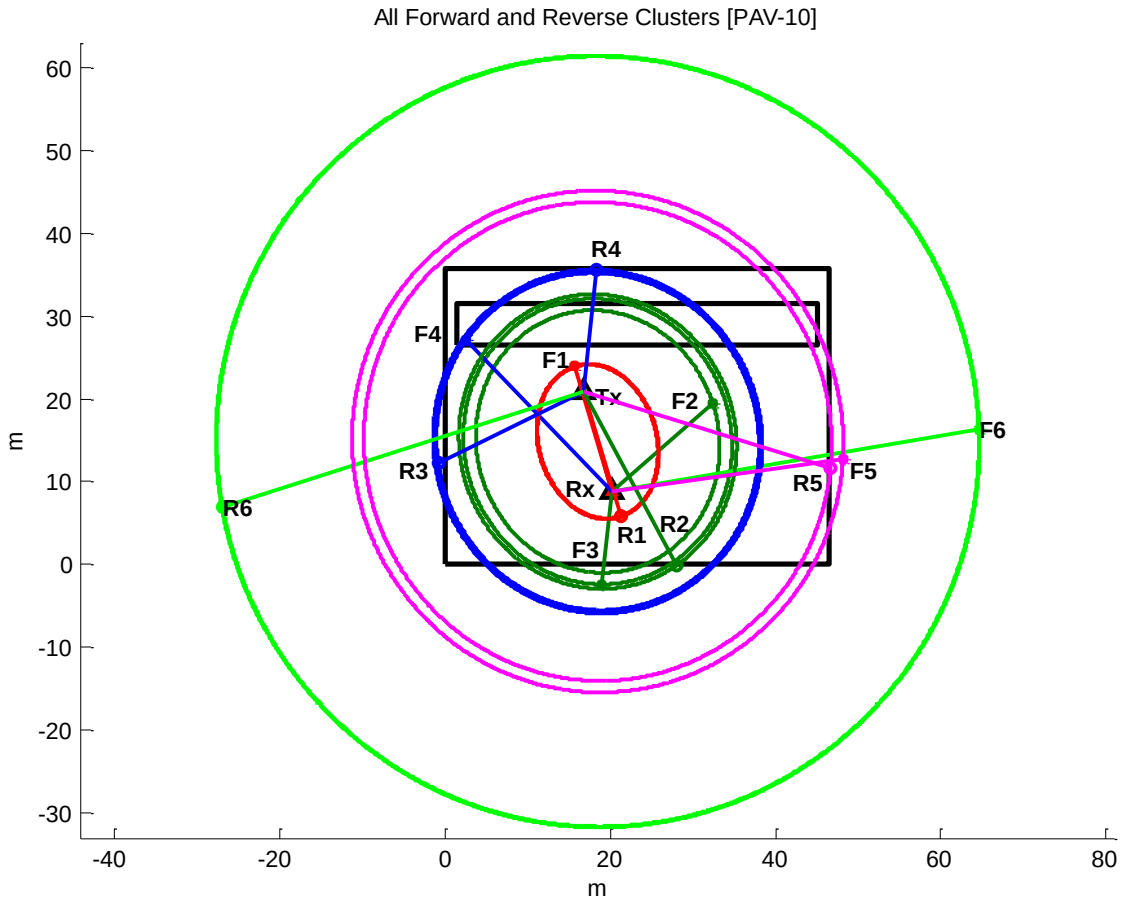

Figure 4-11: Clusters linkage and relation with the scenario objects for a forward and reverse measurement pair [PAV-10]--[PAV-10rv].

Regarding ellipses in blue (corresponding delays from 136 ns to 139 ns) there is only one contribution (cluster) in the forward measurement (F4) and in the reverse measurement two contributions (R3 and R4) appear for the same delay, but none matches the forward contribution in the same angular point. This would suggest that perhaps there is any undetected cluster or maybe some mechanism splits a DoD into two DoAs, thus corresponding to higher order interactions (type 2 or type 3). However, a more careful inspection reveals that the direction by F4 is roughly the mean direction defined by R3 and R4, suggesting that, for the reverse measurement, the clustering algorithm has erroneously split a single cluster into two clusters. Then, the KPM clustering solution with K=5, for the reverse measurement, has been examined and observed that, for this solution, R2 and R5 appear merged together (instead of R3 and R4 as would be desirable). Therefore, it was decided to (manually) force the merging of R3 and R4, to verify if the DoD of the merged cluster matches the DoA corresponding to F4.

Similarly, for ellipses in dark green (corresponding delays from 106 ns to 119 ns) there are two clusters in the forward measurement (F2 and F3) and in the reverse measurement only one cluster (R2) appears for approximately the same delay, but none of the forward clusters matches the reverse contribution in the same angular point. Again, the KPM clustering solution with K=5, but for the forward measurement, has been examined and perceived that, for this solution, F5 and F6 come merged together (instead of F2 and F3 as would be desirable). Over again, it was decided to (manually) force the merging of F2 and F3, to verify if the DoA of the merged cluster matches the DoD corresponding to R2.

Figure 4-12 presents the cluster type 1 already identified (magenta) and clusters which, in the meanwhile, have been merged ([F2+F3] to compare with R2 and F4 to compare with [R3+R4]). As it can be perceived, by organizing clustered data this way allows identifying plus two single interaction contributions corresponding to type 1 clusters. However, the delay matching and the DoA-DoD matching is not perfect in some cases (especially in the case [F2+F3]-R3), but in the contribution of type 1 identified previously (magenta: F5-R5), where it was not necessary any post processing of the clustering solution, the delay and azimuth matching were not perfect either.

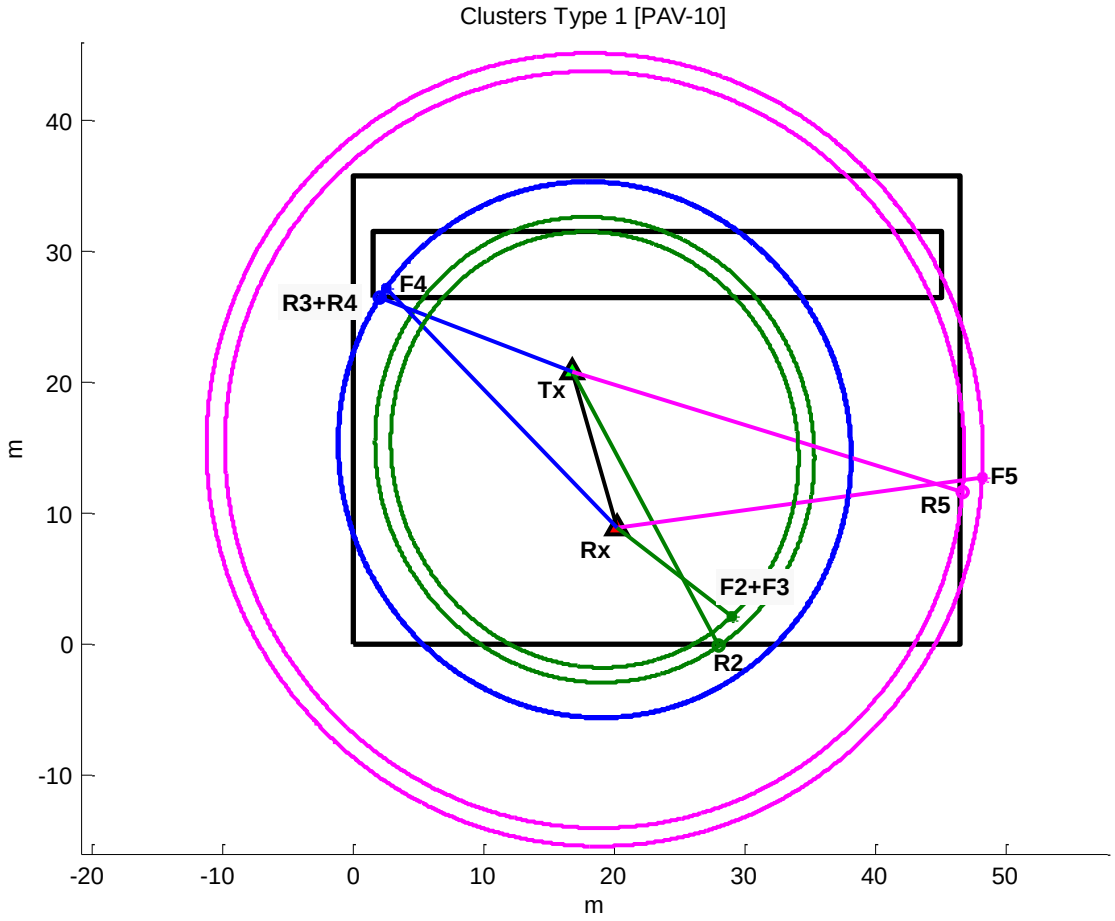

Figure 4-12: Clusters type 1 identified for the measurement pair [PAV-10]--[PAV-10rv].

It should be mentioned that, despite these manual adjustments on the clustering solutions, the global clustering framework (clustering algorithm plus cluster validation) applied has revealed to be a valuable tool, either in obtaining the several candidate partitions for the data set as in the selection of a particular partition. Nevertheless, as the data samples presented throughout this section illustrate, it is important to have a (human) look and some criticism into the outputs of supposedly automatic and systematized tools, so that corrective measures are applied, if needed.

As a final conclusion, given the physical analysis of the data centroids has been able to identify meaningful interactions with the propagation scenario, it may be said that results presented here confirm that the assumption of MPCs arriving in clusters is adequate to describe the channel macro-structure. Small-scale effects are introduced by the superposition of individual MPCs.

Chapter 5

MIMO Modeling and Measurements

This chapter describes the MIMO modeling approach followed. To start, the underlying modeling assumptions are defined; then the gathering of statistical data, extracted from the categorized experimental data collected in the previous chapters, is accomplished; finally, the channel simulator is explained. MIMO channel measurements are also presented and then used for validation purposes.

5.1. Modeling Assumptions

The modeling methodology proposed in this work can be classified as a geometry-based stochastic channel model (GSCM) and therefore, falls within the physical models category. The option for a clustered modeling approach may be justified by remembering the results concerning the physical analysis of clustered DCIRs, presented in chapter 4. These results demonstrated the adequacy of the assumption that MPCs arrive in clusters, because when analyzing the cluster centroids, meaningful interactions with the propagation scenario were identified, which, probably would not be recognized so clearly, if individual MPCs were instead analyzed.

Nevertheless, unlike several of the GSCMs mentioned in section 2.4.5 (and also unlike the work presented in [100]), in this approach scatterers are not directly placed in the scenario according to a spatial scatterer density function. As an alternative, parameters of individual

MPCs, describing the physical channel, are generated from a set of assumed underlying statistical distributions. Subsequently, the scatterers positions are determined from the parameters of the MPCs. In this way, this method combines empirical stochastic channel modeling and geometry-based stochastic channel modeling.

At last, similarly to all geometry-based models, if the radio link properties are defined, the physical model may be converted into the equivalent analytical model, i.e., the transfer matrix of the channel can be computed. The radio link description involves defining: the number of antennas at the transmitter and receiver arrays; the arrangement of the antenna arrays (including the antenna separation distance and the array spatial orientation) and the transmitter and/or the receiver route(s). By this way, it is possible to evaluate different radio link arrangements for the same physical channel structure.

The model should be able to generate MPCs that reproduce the clusters properties observed in experimental data: delays, azimuths and power. In this context, one must take into account rules that govern inter-cluster properties (i.e., centroids properties) and rules that govern intra-cluster properties (MPCs inside clusters).

The proposed model consists of:

- **One Cluster Type 0** containing:
    - The direct ray (first MPC) possibly attenuated if non- or obstructed line-of-sight condition is assumed. Time of arrival of the first MPC is settled by the distance between the transmitter and the receiver.
    - In LoS conditions, a second component deterministically placed may exist, with same power as LoS, in order to reproduce situations where a strong specular reflection with small excess delay occurs (i.e., belonging to the first cluster), as a reflection on the floor or on the ceiling.
    - Several equal powered random MPCs whose excess delay is assumed to be exponentially distributed and the DoA is assumed to follow a Laplace distribution.
- **A few Clusters Type 1** where only delay and DoA are random (as these clusters represent single interactions DoD is defined by the corresponding delay and DoA pair). These clusters consist of:
    - Random centroids whose excess delay is assumed follow an exponential distribution, while DoA is assumed to be uniformly distributed.
    - In each cluster, a number of equal powered random MPCs whose excess delay is assumed to follow a Gaussian distribution around the respective

centroid delay and the DoA is assumed to follow a Laplace distribution, also, around the corresponding centroid DoA.

- **A few Clusters Type 2** similar to clusters type 1, but where delay, DoA and DoD of centroids and MPCs are all random variables, because these represent higher order interactions.

Moreover, it is proposed to use LoS power as the reference level and additional parameters are introduced to specify the power ratio between the reference level and the total power of MPCs in each cluster type. Furthermore, complementary parameters are also introduced in order to control the centroids power decay vs delay.

The assumptions presented in this section envisage a methodology suitable for MIMO channel modeling. Although, to actually being able to model and simulate a particular channel it is necessary to parameterize the assumed statistical distributions and other proposed variables. This can be achieved by carrying out a statistical analysis on the structured data available. Besides, it should also be mentioned that, in addition to the statistical distributions and strategies suggested above, to describe each feature of the model, other have also been investigated. Results from this statistical analysis are given in the next section.

5.2. Statistical Analysis of Clustered DCIRs

As explained in the previous section, the channel modeling approach followed is driven by empirical data: a set of MPCs are generated according to statistical distributions which rule the parameters characterizing each MPC. This section presents the extraction of the statistical parameters which tune each assumed distribution.

The data available consists in a *set of MPCs* (each one is characterized by its delay, azimuth and complex amplitude), a class label vector for MPCs containing a *cluster index* for each MPC, the *centroids position* of each cluster (i.e., the center of the group of MPCs belonging to a specified cluster, given by a power weighted average in each dimension of the delay-azimuth domains) and a class label vector for clusters containing the respective *cluster type* (0, 1, 2 or 3, according to the classification introduced in section 4.7).

The analysis of data has been split into inter- and intra-cluster study: the former deals with centroids (each one representing a group of MPCs) and the latter deals with individual MPCs. Clusters type 0 were treated differently: only intra-cluster analysis has been performed and besides, delays of individual MPCs in this cluster type are referred to the delay of the direct ray, which in turn, is established by the distance between the transmitter

and the receiver. For the remaining clusters, the intra-cluster delay of individual MPCs are referred to the delay of corresponding cluster centroid (allowing for negative excess delays).

5.2.1. Inter-Cluster Analysis

The left-side of Figure 5-1 displays the centroids power vs time of arrival, of all clusters available from the several measurement files and the right-side displays centroids azimuth vs time of arrival. Represented clusters are distinguished in a twofold way: LoS clusters are represented by circles and Obstructed LoS (OLoS) clusters are represented by asterisks; while each cluster type is distinguished by one color. Legend in the left-side figure also applies to the right-side figure.

Number of Clusters

Typical values for the number of clusters have been extracted. Obviously, the number of type 0 clusters will be set to one. Therefore, the number of clusters of type 1 and type 2 for each measurement file has been considered. Characterization is achieved by computing some statistical measures whose results are collected in Table 5-1.

Either for type 1 as for type 2, the most representative value seems to be 2 clusters. The maximum number of clusters observed was 4 for type 1; 5 for type 2, while for these two types together, the observed maximum was 6 and the observed minimum number was 3. Hence, the observed total number of clusters, i.e., type 0 (1) plus type 1 plus type 2, varies from 4 to 7.

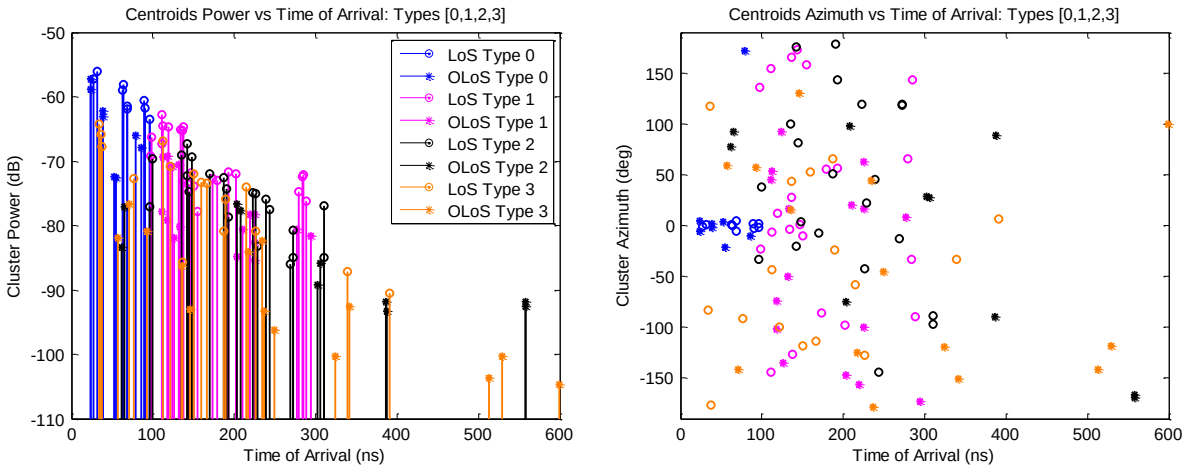

Figure 5-1: Available clusters from all measurement files.
Left: Centroids power vs time of arrival. **Right:** Centroids azimuth vs time of arrival.

Table 5-1: Number of clusters type 1 and type 2.

Cluster ID	Range	Mean	Mode	Median
Type 1	[0, 4]	1.9	2	2
Type 2	[0, 5]	2.0	1	2
Type 1 + Type 2	[3, 6]	3.9	3	4

Delay and Azimuth Analysis

The experimental Cumulative Density Functions (CDFs) of *excess delay* and *inter-arrival delay* for centroids of the several clusters were fitted to an exponential distribution. Initially, cluster delays of all measurement files were collected all together as a data ensemble, but obviously, centroids of type 0 were excluded from this the data set in the excess delay analysis, because it would create an erroneous probability at zero excess delay and in the inter-arrival analysis, they are naturally excluded by computing the inter-arrival between the first two clusters. As explained before, time of arrival for cluster zero is not statistically drawn, as it is implicitly defined by the distance between the transmitter and the receiver. Both CDFs (for cluster excess delays and cluster inter-arrival delays) present a reasonable adjustment to the exponential distribution. The chi-square goodness-of-fit test[6], at significance level of 1%, has been used to verify the suitability of the exponential distribution [101].

Nevertheless, as clusters of type 1 represent single-bounce interactions, it is expected that the corresponding excess delays are smaller than excess delays for clusters of type 2, which represent higher order interactions, and accordingly represent, potentially, higher path lengths. This assumption may be visually confirmed in Figure 5-1, where it can be clearly seen that the maximum time of arrival for clusters type 1 is about 300 ns, while for clusters type 2 is about 550 ns. Additionally, clusters of type 3 (those whose delay contribution was identified in only one direction of the double-directional measurement) present times of arrival covering the entire range of estimated times. These contributions may arise from an inability of the SAGE algorithm in estimating the equivalent

[6] The chi-square goodness-of-fit test is used to test if a sample of data comes from a population with a specific distribution. It evaluates how likely it is that any observed difference between the sets arose by chance. The test consists in computing a normalized sum of squared deviations between observed and theoretical frequencies. If the probability (given by a χ^2 distribution) of observing such a deviation is higher than the specified significance level the hypothesis that the data come from a population with the specified distribution cannot be rejected.

contribution in the inverse direction measurement file (this has been clearly observed in the contributions with higher times of arrival); or may also arise from an inadequate recognition of clusters (i.e., splitting of a single existing cluster or merging of different existing clusters) in one direction of the measurement, associated with a correct identification in the opposite direction of the measurement. Any of these reasons, contribute to the inability of performing the linkage of each of these clusters with another cluster in the measurement made in the opposite direction.

Therefore, in a second analysis step, three data collections were composed: one comprising clusters of type 1 together with clusters of type 2 and the other two comprising clusters of these two types separately. Hence, in this analysis, clusters of type 3 were not considered. Each data collection has also been fitted to an exponential distribution and Figure 5-2 depicts the CDFs obtained and the corresponding fitting to the exponential distribution. In the legend it can be read the survival parameter, β, (corresponding to the mean delay) of each adjusted exponential distribution. Again, by using the chi-square goodness-of-fit test (significance level of 1%) has been concluded that the hypothesis of data coming from an exponential distribution cannot be rejected. Indeed, Figure 5-2 confirms that the parameter which characterizes the exponential is considerably different if clusters type 1 and clusters type 2 are examined individually. In contrast, the behavior of the inter-arrival delay seems to be independent of the type of cluster considered, since no substantial difference has been perceived by splitting the clusters based on their type.

Regarding the azimuth analysis, the data ensemble comprising clusters of type 1 together with clusters of type 2 has been subjected to the chi-square goodness-of-fit test (significance level of 1%) and it sustained that the assumption of centroids azimuth being uniformly distributed in $[-\pi, \pi]$ is acceptable.

Power Analysis

The delay analysis conducted evidenced that either the excess delay as the inter-arrival delay may be adequately modeled by an exponential distribution appropriately parameterized, but, to extract rules for power-delay decay it is more convenient to employ the excess delay which, hereafter, is simply referred as *delay*. Once more, clusters of type 1 and clusters of type 2 were analyzed separately, in order to scrutinize if the power-delay behavior of these two types of clusters is significantly different. Additionally, centroids of each cluster type were further split into centroids from LoS and OLoS measurements. The left-side of Figure 5-3 displays results for clusters of type 1 and the right-side results for clusters of type 2. In the legend of this figure it can be read the slopes obtained for each data set.

Results in Figure 5-3 indicate that if LoS and OLoS data is considered together as a data ensemble, the global power decay slopes for clusters type 1 and clusters type 2 are roughly similar. Analogously, for clusters type 1, LoS and OLoS centroids also present similar slopes (note that the two lines in magenta look almost parallel). On the other hand, for clusters type 2, LoS and OLoS centroids reveal very different slopes: a much higher slope for LoS centroids and a significantly lower slope for OLoS clusters).

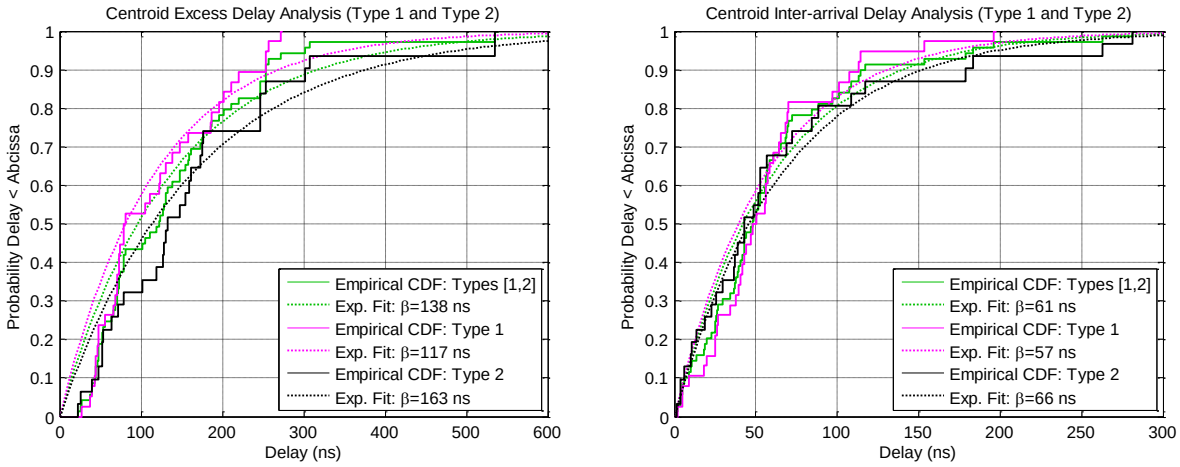

Figure 5-2: Experimental CDFs (solid lines) and adjusted exponential CDFs (dotted lines). **Left:** Excess delay analysis. **Right:** Inter-arrival delay analysis.

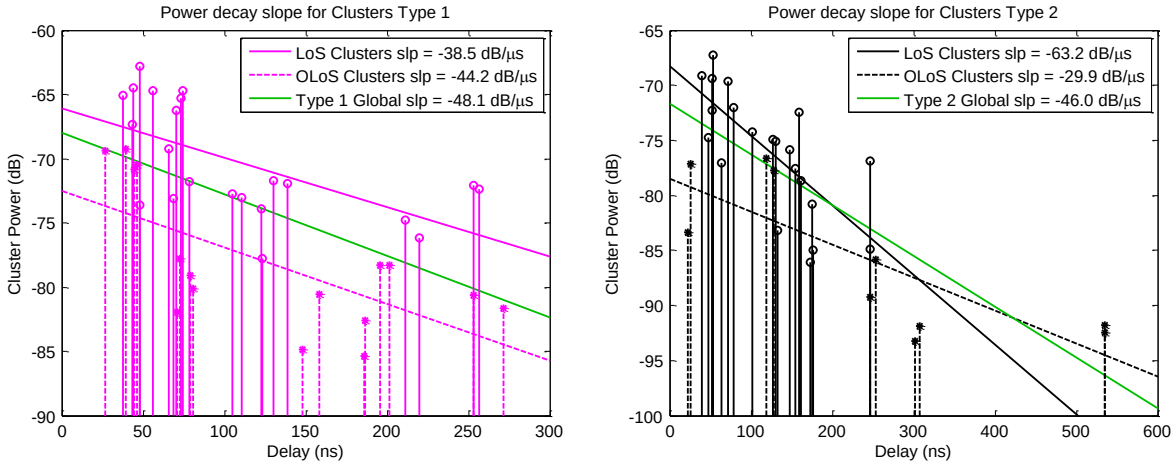

Figure 5-3: Power decay slope vs. delay. **Left:** Clusters type 1. **Right:** Clusters type 2.

In order to attain a comprehensive power characterization, the first MPC has been established as the power reference. This MPC corresponds to the direct ray, which under LoS conditions presents the highest power. Furthermore, the ratio between the power of this MPC, $|\alpha_D|^2$, to the power sum of all MPCs in each cluster type has been computed. These quotients represent the power relation between the direct ray to the multipath power belonging to each cluster type, *T*, and may be denoted by

$$K_T = \frac{|\alpha_D|^2}{\sum_i |\alpha_i|^2}, \quad i:\ \alpha_i \in C_T, \quad T = \{0,1,2\}. \tag{5.1}$$

Once again, as for the power decay slope, typical values for these power ratios have been identified for clear LoS and OLoS situations. Moreover, taking into account the behavior shown by the measurements under LoS condition and concerning to the power ratio for cluster type 0, K_0, two situations have further been distinguished: direct ray only (D) plus multipath or direct ray and strong specular reflection (D+R) plus multipath. In this cluster type, the multipath power excludes the direct ray (first MPC) and also, if existing, the strong specular reflection, since these are viewed as deterministic components. For clusters type 1 and 2, the multipath power represents the power sum of all components belonging to these cluster types.

Measurements displayed in Figure 3-12 and Figure 3-13 correspond to a D+R case: notice the two big, dark red circles at initial delays. These two circles belong both to cluster 0 (cf. with Figure 4-9 and Figure 4-10, respectively). Yet, not all LoS measurement files show this behavior.

In addition, for OLoS measurements the obstruction loss has been investigated by comparing the power of the first MPC (i.e., the reference level) of these measurement files with the power of the first MPC in LoS measurements. The four OLoS measurements provided distinct values for the *obstruction loss* parameter, as just defined, because each measurement has been carried out in different conditions. Available measurements cover OLoS situations created by: a red brick wall (inside-outside); a door with some parts made of glass; a combined version of the previous two situations; and by the spectators' seats (in this last case more than one wall may be traversed and/or possibly concrete parts). It has been found that the first two cases show very similar obstruction losses (about 3 dB) which correspond also to the lowest observed losses.

Final Remarks

The reader, who takes a reading from one end to the other, may, at this moment, be wondering about the lack of values for all features and different situations mentioned (namely, for identified power ratios). In this section, it is intended to put the emphasis on the followed methodology allowing the gathering of data which will be used for parameterization of the envisaged channel simulator. When explaining the simulator it will be obligatory to enumerate all relevant features, its characterization and numeric values. If all data is presented as the methodology is being explained, data becomes spread across several subsections. It is the author's opinion that, if the information is congregated all together it may be easier to attain the global picture. Hence, a global summary of data made available either by the present inter-cluster analysis, as by the intra-cluster analysis described in section 5.2.2, is given in section 5.3, when explaining the channel simulator.

Data gathered during this inter-cluster analysis characterizes the channel macro-structure completely. For an assumed number of clusters (of type 1 and type 2) present in the channel, this data allows to draw the excess delay for each cluster centroid, the respective azimuth and to compute each cluster total power.

5.2.2. Intra-Cluster Analysis

Intra-cluster analysis has been accomplished in a very similar way as already done for inter-cluster analysis: typical values for the number of MPCs in each cluster; statistical distributions and the corresponding parameters, for intra-cluster delay and azimuth, are given in this section.

Number of MPCs per Cluster

Figure 5-4 shows the number of MPCs in each cluster. Again, each cluster type is differentiated by one color, whereas LoS clusters are represented by circles and OLoS clusters are represented by asterisks. In this figure, it may be observed that the number of MPCs seems to be related with the cluster type. Also, a relation with the cluster delay seems to exist, but this behavior may the caused by the inability of the SAGE algorithm in estimating MPCs with higher delays and less power (as described in chapter 3). Taking this into account and with the purpose of not to complicate the model assumptions, only the connection with the cluster type is studied.

Thus, by computing again some statistical measures, for each cluster type, representative values for the number of MPCs per cluster have been identified. Mode is not presented

because some parameters presented several modes. Additionally, the total number of MPCs, present in the channel, has also been computed. Table 5-2 summarizes the data collected by this study.

Delay Analysis

For clusters of type 0, the first MPC (corresponding to the direct ray delay) has been established as the delay reference. Intra-cluster delays and the corresponding empirical CDF have then been computed. As for centroid delays (inter-cluster), the exponential distribution appropriately parameterized, may be used to characterize the intra-cluster delay for clusters of type 0.

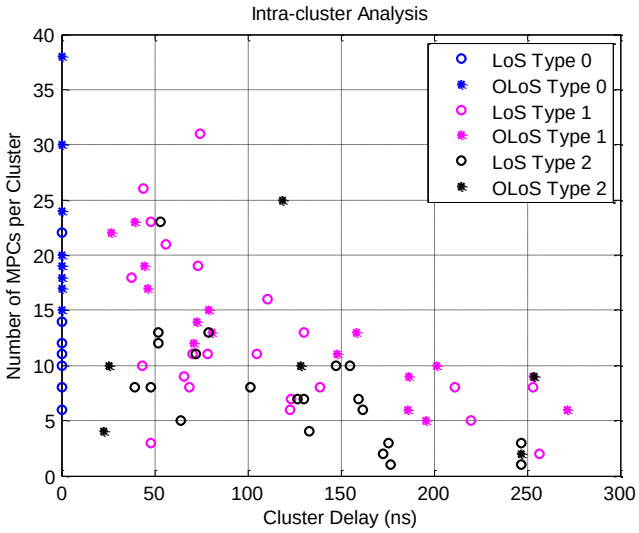

Figure 5-4: Number of MPCs per cluster: each cluster type is differentiated by one color, whereas LoS clusters are represented by circles and OLoS clusters by asterisks.

Table 5-2: Typical values for the number of MPCs per cluster and for the total number of MPCs.

Attribute		Range	Mean	Median
N.º of MPCs per Cluster	Clusters T0	[6, 38]	17.2	16
	Clusters T1	[2, 31]	12.6	11
	Clusters T2	[1, 25]	7.3	7
	Global: T[0,2]	[1, 38]	11.6	10
Total N.º of MPCs		[48, 82]	65.3	66.5

In contrast, the delay reference for clusters of types 1 and 2 is given by the corresponding cluster centroid. This intra-cluster delay signifies the delay deviation of a given MPC from the corresponding centroid. For this reason, it is expected that intra-cluster delays may be conveniently described by a statistical distribution that shows symmetry around the mean value (expected to be zero). The left-side of Figure 5-5 displays, this delay deviation for MPCs belonging to clusters of type 1 and type 2, but in separate charts for LoS and OLoS clusters. At least visually, the expected symmetry is reasonably confirmed. Besides, it can be observed that OLoS delays appear to be more spread than LoS delays. Hence, besides the global data set, CDFs for LoS and OLoS delays were also considered individually.

Among several symmetric statistical distributions that could be used to characterize intra-cluster delay, the Laplace and the Gaussian distributions were studied. The chi-square goodness-of-fit test evidenced that either the Laplace or the Gaussian distribution may represent the data sets analyzed. Thereby, the Gaussian distribution has been chosen. The right-side of Figure 5-5 presents the three empirical CDFs and the respective fitting to the Gaussian distribution. As expected, the standard deviation of LoS intra-cluster delays is smaller than for OLoS delays.

Azimuth Analysis

In the same way, for azimuth intra-cluster statistics, the azimuth reference for a given MPC is established as the respective cluster centroid. When computing the azimuth deviation of a given MPC to the corresponding centroid, attention must be paid to the angles ambiguity: note that any angle difference cannot be greater than 180º. Additionally, in this case, the sign information is also relevant.

The left-side of Figure 5-6 shows the intra-cluster azimuth distinguished by each cluster type. In this figure and unlike the delay behavior, it is obvious that for higher centroid delays the data spread tends to diminish. Therefore, two data sets were formed: one with azimuth data corresponding to centroids whose delay, τ_c, is not greater than 150 ns and the other one corresponding to centroids whose delay is greater than 150 ns. The respective empirical CDFs and fitting to the Laplace distribution are given in the right-side of Figure 5-6.

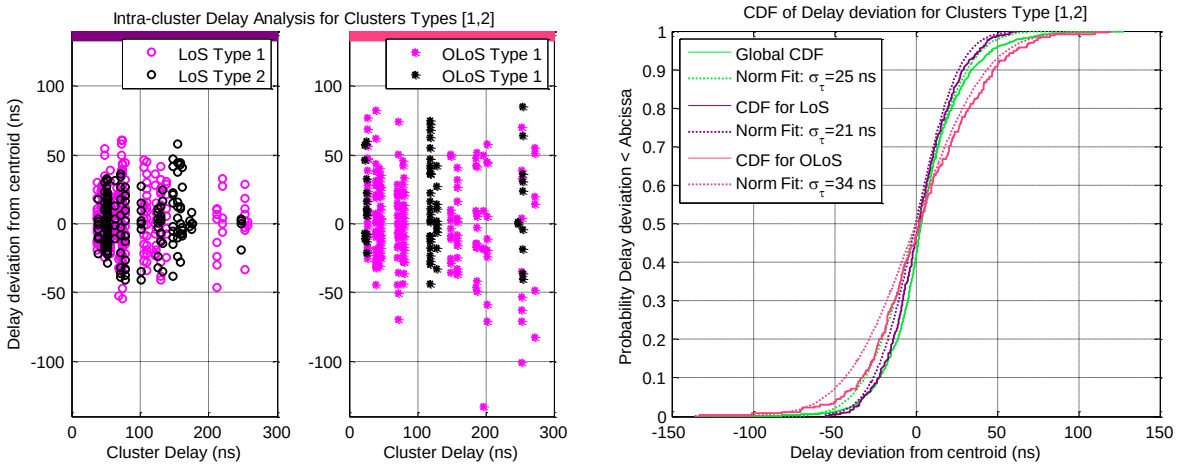

Figure 5-5: Intra-cluster delay analysis. **Left:** LoS and OLoS delays for clusters of types 1 and 2. **Right:** Empirical CDFs and fitting to the Gaussian distribution.

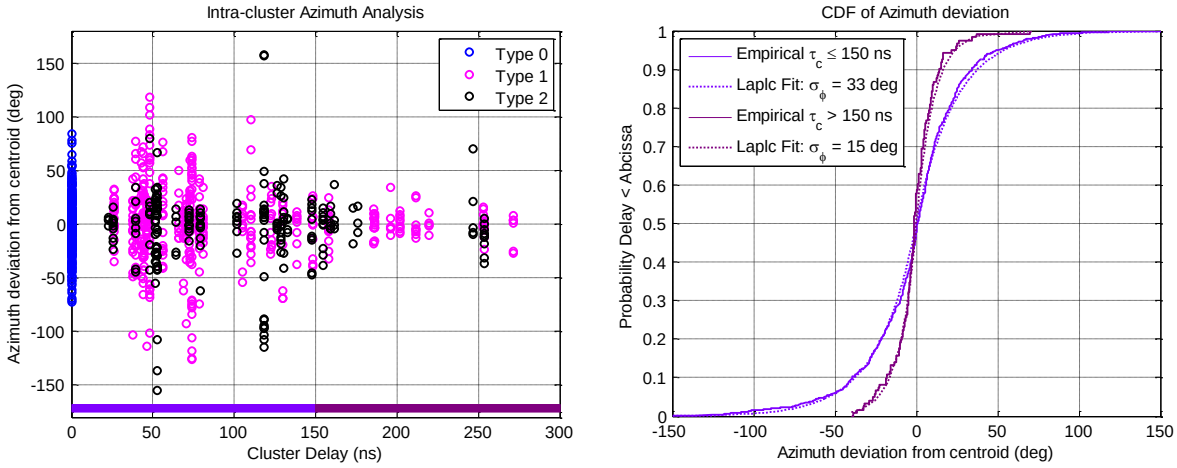

Figure 5-6: Intra-cluster azimuth analysis. **Left:** Azimuth deviation from centroid. **Right:** Empirical CDFs and fitting to the Laplace distribution.

Final Remark

The parameters extracted through the intra-cluster analysis will enable to draw the intra-cluster delays and also, the intra-cluster azimuths, for MPCs in each cluster (except for the first MPC in cluster 0). The effective delay and azimuth of a given MPC may be obtained by adding the intra-cluster delay and azimuth, respectively, to the delay and azimuth of the corresponding centroid, which in turn are dictated by inter-cluster characterization, presented in section 5.2.1. The power of each cluster, which may also be computed from these parameters (power ratio and power decay slope), is assumed to be equally distributed by the MPCs belonging to the given cluster.

5.3. Channel Simulator Description

The fundamental modeling assumptions (presented in section 5.1) and the statistical analysis just carried out (in section 5.2) enable the channel characterization by means of simulation. Figure 5-7 displays the flowchart of the developed channel simulator: rectangular shaped objects represent software routines and oval shaped objects represent data input/output.

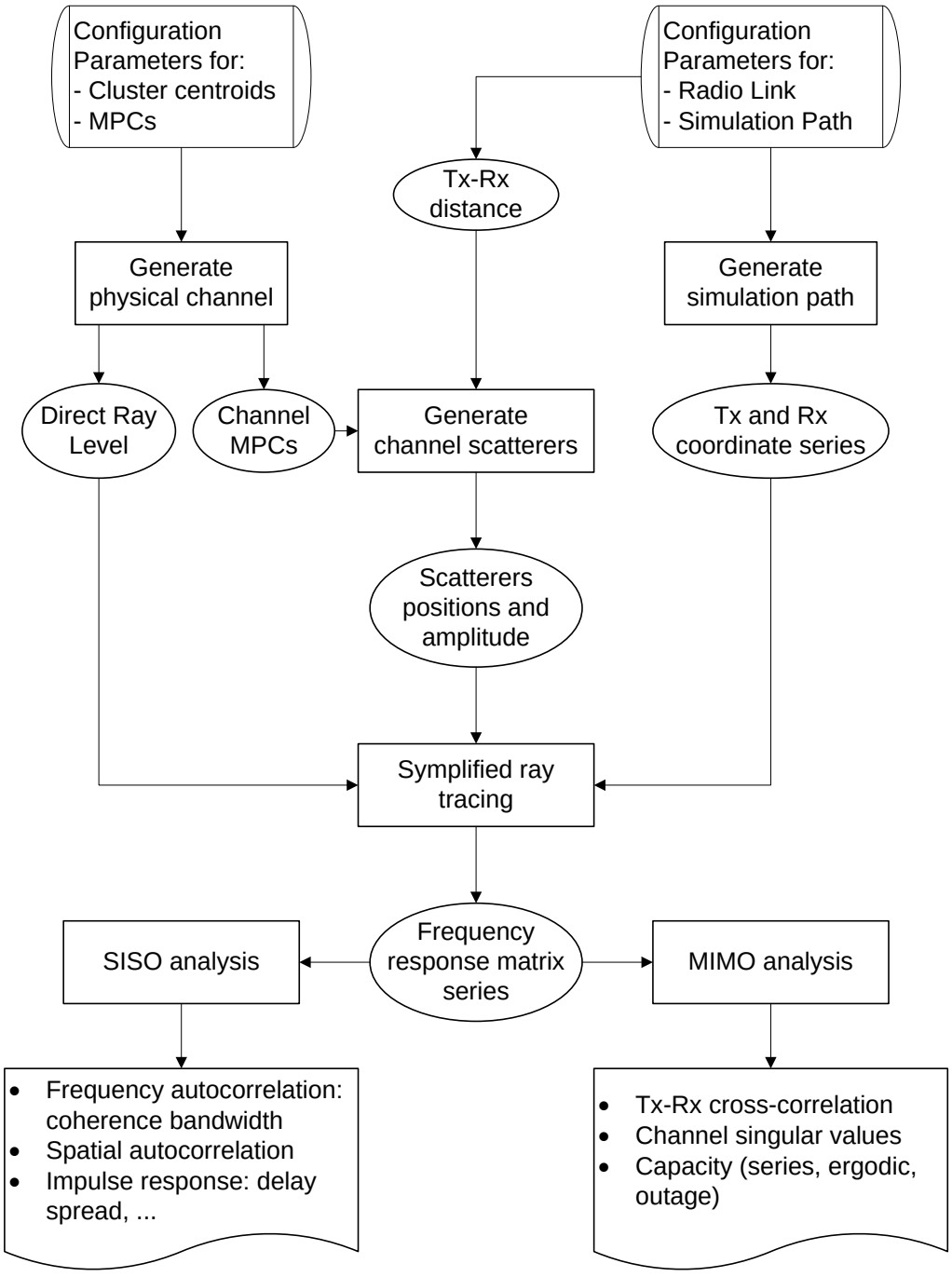

Figure 5-7: Flowchart of the channel simulator: rectangular shaped object represent software routines and oval shaped objects represent data input/output.

As Figure 5-7 shows, the channel simulator comprises the following main steps:

1- Configuration:
   a. Specify all parameters for the underlying statistical distributions and for the assumed rules that govern inter- and intra-cluster properties.
   b. Characterize the radio link (carrier frequency, bandwidth, transmitter- receiver distance); the transmitter and receiver arrays arrangements; the transmitter and/or the receiver travelled paths.

2- Generation of the channel MPCs from the previously configured parameters.

3- Generation of the coordinates (positions) and complex amplitudes of scatterers in the channel.

4- Generation of the coordinates of the transmitter and receiver arrays along the corresponding travelled path.

5- By means of simplified ray tracing obtain the matrix series of the channel frequency responses.

The most relevant implementation aspects of the channel simulator are explained in the following subsections. At the same time, the achievements and outputs at each step are illustrated using a generated sample channel.

In the flowchart a supplementary step is represented which regards the channel analysis: some of the common evaluation measures are mentioned, but this list is not closed. The matrix series of the channel frequency responses may be manipulated (analyzed) so it provides the features whose assessment is in target. Some results of these evaluation measures, for the same generated sample channel, are given in section 5.3.5.

5.3.1. Generation of Channel Centroids and MPCs (Step 2)

Table 5-3 and Table 5-4 recapitulate all data, gathered in the previous section, which allows the parameterization of the simulator concerning the inter- and intra-cluster channel properties (step 1-a.). This data enables to generate every channel cluster and MPCs belonging to it, according to the assumptions enumerated in page 88. Besides, the program writing for the construction of the physical channel also follows the sequence established in page 88 and this will be, as well, the sequence followed here.

Table 5-3: Inter-cluster characterization parameters used by the channel simulator.

Attribute		Characterization	Parameterization			
Excess delay		Exponential distribution - survival parameter: β	Cluster T1: β_1 [ns]			117
			Cluster T2: β_2 [ns]			163
Azimuth		Uniform distribution - interval limits	Global [T1+T2]: [deg]			[–180, 180]
Power	Power Decay	Linear slope in dB per time delay unit	Cluster T1 [dB/μs]	LoS		–38.5
				OLoS		–44.2
				Global [LoS+OLoS]		–48.1
			Cluster T2 [dB/μs]	LoS		–63.2
				OLoS		–29.9
				Global [LoS+OLoS]		–46.0
	Power Reference	First MPC → $\lvert\alpha_D\rvert^2$ - If LoS → 0 dB - If OLoS → $-L_{OBST}$ (obstruction loss)	L_{OBST} for OLoS [dB]	Red brick wall or Door		3
				Red brick wall + Door		12
				Several walls / Concrete		20
	Power Ratio	$K_T = \frac{\lvert\alpha_D\rvert^2}{\sum_i \lvert\alpha_i\rvert^2}$ where $\lvert\alpha_D\rvert^2$ direct ray power $\lvert\alpha_i\rvert^2$ *i*-th MPC power	Cluster T0 K_0 [dB]	LoS	D	2.5
					D+R	–0.8
				OLoS		–17
			Cluster T1 K_1 [dB]	LoS		3.5
				OLoS		-14
			Cluster T2 K_2 [dB]	LoS		10
				OLoS		-7
Number of Clusters			Cluster T0			1
			Cluster T1			2
			Cluster T2			2

Nevertheless, some aspects are shared among different features (clusters types and/or centroids) and one of these is the generation of random variables with prescribed distributions. Delays and azimuths (for centroids and also for individual MPCs) are randomly drawn from the underlying statistical distributions. According to the feature considered, different distributions were envisaged and parameterization data for these distributions has been extracted in section 5.2. In addition to the uniform and Gaussian distributions, the exponential and Laplace distributions were also the contemplated.

Table 5-4: Intra-cluster characterization parameters used by the channel simulator.

Attribute	Characterization	Parameterization		
Delay	Exponential distribution - survival parameter: β	Cluster T0: β_0 [ns]		24
	Normal distribution - mean: $\mu_c = \tau_c$ - standard deviation: σ	Clusters T[1,2] σ [ns]	LoS	21
			OLoS	34
			Global	25
Azimuth	Laplace distribution - mean: $\mu_c = \phi_c$ - scale parameter: b $b = \sigma/\sqrt{2}$ where σ is the standard deviation	Standard deviation σ [deg]	$\tau_c \leq$ 150 ns	33
			$\tau_c >$ 150 ns	15
Number of MPCs		Cluster T0	m_0	15
		Cluster T1	m_1	15
		Cluster T2	m_2	10

Regularly, programming languages or environments for numerical computation offer tools for generating random variables that follow the uniform distribution. Frequently, also the Gaussian distribution and maybe others are contemplated. But, naturally, not all distributions are provided and a method must be employed for generating random variable with a desired (generic) CDF. In the main, methods for generating random variables with a given CDF are based on the availability of random numbers that are uniformly distributed. One of these methods has been employed and it is presented in appendix A.

Cluster 0

Cluster 0 consists of m_0 MPCs. As explained before, the first MPC belonging to cluster 0 is not randomly drawn: total delay (or time of arrival) is defined by the distance between the transmitter and the receiver; the azimuth is zero and its power is given by the obstruction loss parameter (0 dB for LoS condition). Azimuths of MPCs belonging to cluster 0 correspond to DoAs and are referred to the line from the receiver to the transmitter, thus, the azimuth of the transmitter is always zero.

Still for LoS situation, if the simulator is run with the option for a strong specular reflection, a second equal powered MPC is placed: the excess delay of this MPC is uniformly distributed in the interval [15, 25] ns and the azimuth is zero as well.

The delays and azimuths (DoA) for the remaining $m_0 - 2$ or $m_0 - 1$ MPCs (respectively, if the strong reflection exists or not) are then randomly drawn from the underlying statistical distributions: an exponential distribution (with parameter β) for delays and a Laplace distribution with zero mean (μ) and standard deviation (σ) for azimuths. The generation of random variables uses the CDF transformation method presented in appendix A.

Let m_0' denote the number of MPCs in cluster 0 which are randomly drawn. The amplitude of these MPCs is defined by the power ratio, K_0, according to

$$|\alpha_{i0}| = \frac{|\alpha_D|}{\sqrt{m_0' K_0}} . \tag{5.2}$$

Clusters Type 1 and Type 2

Aside from specific parameterization values, clusters Type 1 and Type 2 present several similarities and just a few differences. For this reason, here they are discussed conjointly and every difference is evidenced, but, in the channel simulator they are treated separately.

For these clusters types the centroids are drawn first where delays follow an exponential distribution; azimuths are uniformly distributed and power is established by the power ratio, K_1 (or K_2) and by the power decay slope, S_1 (or S_2) parameters.

Azimuths of MPCs belonging to clusters type 1 correspond to DoAs, as in cluster 0, but for clusters type 2 two azimuths are drawn for each centroid, one being the DoD and the other being the DoA. This is because each MPC in clusters of type 1 will be associated to only one scatterer position (representing a single-bounce interaction), while each MPC in clusters type 2 will be associated with two scatterer positions (allowing to represent double- or multiple-bounce interactions).

The power of each centroid represents the power sum of individual MPCs in the corresponding cluster. The following exemplary formulas are given for clusters type 1, but identical ones are used for clusters type 2, which may be obtained simply by replacing K_1 by K_2 and S_1 by S_2. The power (in dB) of clusters follows a linear decay law, given by

$$P_{ck}^{\mathrm{dB}} = S_1 \tau_{ck} + P_0^{\mathrm{dB}} , \tag{5.3}$$

where *ck* denotes the cluster index; P_{ck}^{dB} and τ_{ck} the power and delay of this cluster, respectively, and P_0^{dB} represents the *y*-axis intercept. Note however that, the intercept does not correspond to the power of cluster 0. Indeed, the following condition must be satisfied

$$K_1 = \frac{\left|\alpha_{\mathrm{D}}\right|^2}{\sum_i \left|\alpha_i\right|^2} = \frac{\left|\alpha_{\mathrm{D}}\right|^2}{\sum_{ck} P_{ck}}, \tag{5.4}$$

where $|\alpha_i|$ denotes the amplitude of individual MPCs belonging to a given cluster type, while P_{ck} represents the power sum of individual MPCs belonging to a specific cluster, *ck*. By inserting

$$P_{ck} = 10^{\frac{\left(S_1\tau_{ck} + P_0^{\mathrm{dB}}\right)}{10}}, \tag{5.5}$$

in (5.4), P_0^{dB} may be expressed as

$$P_0^{\mathrm{dB}} = 10\log_{10}\left(\frac{\left|\alpha_{\mathrm{D}}\right|^2}{\sum_{ck} 10^{S_1\tau_{ck}/10}}\right) - K_1^{\mathrm{dB}}. \tag{5.6}$$

With each cluster centroid specified, the individual MPCs may now be generated. Inside clusters, a number of equal powered MPCs are placed whose delays follow a Gaussian distribution, with mean $\mu = \tau_{ck}$ and standard deviation specified in Table 5-4.

Azimuths follow a Laplace distribution, with mean defined by the corresponding centroid azimuth and standard deviation specified also in Table 5-4. Analogously to the centroids, the azimuth of each MPC belonging to clusters of type 1 represents DoA, while each MPC belonging to clusters of type 2 has a DoA and also a DoD.

Regarding the delay generation, and taking into account that the Gaussian distribution is, theoretically, unbounded, there is a chance that a negative delay is drawn (especially if the centroid delay is small). In case of having drawn a negative delay, a new centroid delay and corresponding MPCs delays are drawn. For this reason and because the cluster power depends on its delay, the exact processing order is:

1- Generate delay and azimuth(s) for every cluster centroid.
2- Generate delay and azimuth(s) for every MPC.
3- Check for negative delays

   Yes:

   a. Generate new centroid delay for problematic cluster(s).
   b. Generate new delay for MPCs belonging to these clusters.
   c. Go to step 3.

4- Obtain each cluster power by using equations (5.6) and (5.3).
5- Distribute (equally) the power of each cluster among MPCs belonging to it.

Figure 5-8 displays a sample of a generated channel for the case of LoS plus a strong reflection. In the left-side of this figure, the channel impulse response is shown, where individual MPCs are represented by *stems* ending in point-shaped markers and cluster centroids are represented by *stems* ending in diamond-shaped markers. In addition, cluster types are distinguished by color. In the right-side of this figure, the DCIR is presented which achieves a more complete channel representation, i.e., a representation covering delay, DoA and amplitude domains.

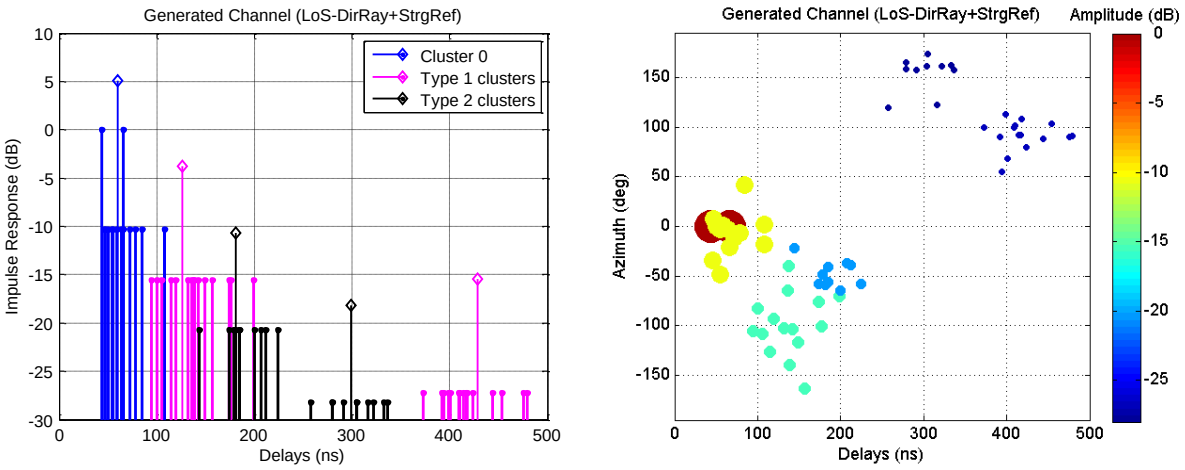

Figure 5-8: Sample of a generated channel for LoS plus strong reflection condition. **Left:** Channel MPCs (points) and cluster centroids (diamonds). **Right:** Directional channel impulse response.

5.3.2. Generation of the Channel Scatterers (Step 3)

With exception of the direct ray, MPCs generated in the previous step, are then represented by scatterers in the propagation scenario whose positions are computed from the respective delays and azimuth(s). The MPC amplitude is assigned to the associated scatterer. In addition, a random phase, φ, is attached to each scatterer.

Figure 5-9 illustrates the method employed [62] to find the scatterer position corresponding to a given MPC: the transmitter and receiver, separated by 2*d*, are assumed to be placed on the foci of an ellipse (centered at the origin and with the major axis along the *x*-axis) which is defined by the MPC delay and the respective azimuth(s) define(s) the scatterer position in this ellipse. The general equation of an ellipse is expressed by

$$\frac{x^2}{a^2}+\frac{y^2}{b^2}=1, \tag{5.7}$$

where, a and b are the semi-major and semi-minor axes, respectively, which verify $d^2=a^2-b^2$. The ellipse eccentricity is $e=\frac{d}{a}$ and also of interest are

$$r_1=a+ex \text{ and } r_2=a-ex. \tag{5.8}$$

The path length associated to the delay of a given MPC, created by means of a reflection on a scatterer, defines one ellipse verifying $r_1+r_2=2a=c\tau$, where c is the speed of light. Therefore, each ellipse (with parameters a_i and b_i) is specified by the delay of a given MPC, τ_i, and by the distance between the transmitter and receiver, 2*d*, as follows

$$a_i=\frac{c\tau_i}{2} \text{ and } b_i=\sqrt{a_i^2-d^2}. \tag{5.9}$$

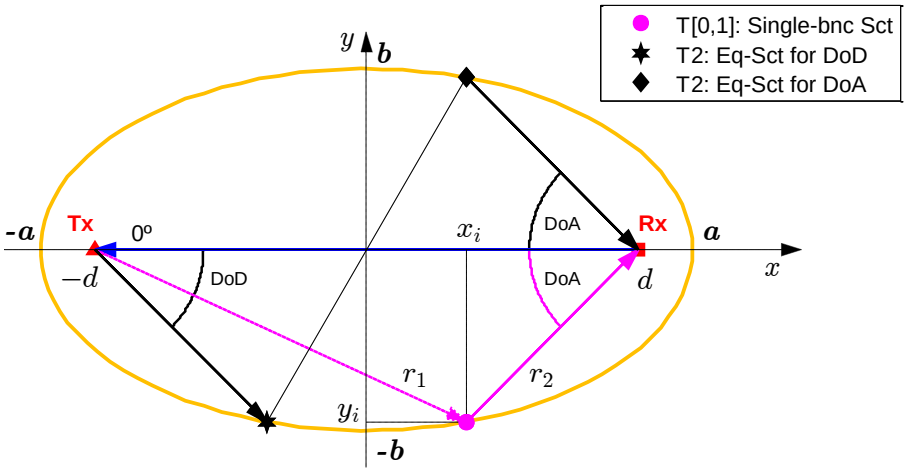

Figure 5-9: Single-bounce scatterers (magenta) and multiple-bounce scatterers (black).

The azimuth information allows to obtain the scatterer position, (x_i, y_i), on the ellipse *i*, where the *x*-*y* axes are assumed to define the horizontal plane. As explained before, for single-bounce scatterers (representing MPCs belonging to cluster type 1) the azimuth corresponds to DoA and (in conjunction with delay) suffice for completely determine its position. Observing the geometry of the problem (Figure 5-9) it can be easily concluded that there is a single solution which satisfies a given path length (defined by delay) for a given DoA. Thus, the scatterer position is given by

$$x_i = d - r_2 \cos(\phi_{\mathrm{DoA}}) = \frac{d - a_i \cos(\phi_{\mathrm{DoA}})}{1 - e\cos(\phi_{\mathrm{DoA}})} \tag{5.10}$$

$$y_i = (a_i - e\,x_i)\sin(\phi_{\mathrm{DoA}}). \tag{5.11}$$

With exception of the direct ray, MPCs belonging to cluster 0 also represent a single-bounce reflection. However, the characteristics of the propagation scenario (sports hall) may justify, besides reflections in the floor, also reflections in the ceiling or, as well, the combination of these two. Therefore, for these MPCs the corresponding single-bounce scatterers were assumed to be positioned in ellipses placed in the vertical *x*-*z* plane, so $y_i = 0$ and equations (5.10) and (5.11) give, respectively, the x_i and z_i coordinates.

Regarding multiple-bounce scatterers (representing MPCs belonging to clusters type 2), these are additionally characterized by a DoD and it may exist several solutions that satisfy a given path length (delay) for the DoD/DoA pair. Therefore, it has been decided to employ the equivalent scatterer concept, but, in order to conveniently reproduce the channel properties at both link-ends, each MPC is represented by two equivalent scatterers as shown in Figure 5-9. Similarly to single-bounce scatterers, the equivalent scatterer for arrival (represented by a diamond shaped marker) is obtained using equations in (5.10) and (5.11), but, to obtain the equivalent scatterer for departure (represented by a hexagram shaped marker) these equations must be updated as follows

$$x_{i\mathrm{DoD}} = -\left(d - r_1 \cos(\phi_{\mathrm{DoD}})\right) = \frac{a_i \cos(\phi_{\mathrm{DoD}}) - d}{1 - e\cos(\phi_{\mathrm{DoD}})} \tag{5.12}$$

$$y_{i\mathrm{DoD}} = (a_i + e\,x_i)\sin(\phi_{\mathrm{DoD}}). \tag{5.13}$$

The total path length, associated with each pair of two equivalent scatterers, is defined by the corresponding MPC delay and they are assumed to be (jointly) represented by only one amplitude coefficient, corresponding to the MPC amplitude.

Figure 5-10 displays the channel scatterers for the sample channel presented in Figure 5-8, where: blue scatterers represent MPCs of cluster 0 (with exception of the direct ray);

magenta scatterers describe contributions from clusters type 1; while black scatterers are associated with clusters type 2. For the latter, each contribution is characterized by one pair of scatterers: one represented by a hexagram shaped marker plus another represented by a diamond shaped marker.

5.3.3. Generation of the traveled route(s) (Step4)

In this work it is suggested to achieve the channel characterization by means of simulation, providing for this purpose, synthetic series of channel realizations. To produce these series, the transmitter and/or the receiver are assumed to travel along a straight route, which is closely sampled. Each sampling point in the route corresponds to one value in the simulated series, i.e., a snapshot. If velocity is known, the generated series may be represented either in the traveled distance domain or in the time domain.

The transmitter and receiver are assumed to be equipped with linear antenna arrays. Table 5-5 offers sample parameters that stipulate the arrangement, at the transmitter and receiver, of the *antenna arrays*: number of antennas, antenna separation and array orientation. This table includes also parameters that specify the *transmitter and receiver routes* (direction, length and inter-samples separation) and the radio link (carrier frequency and bandwidth). Figure 5-11 explains the geometry and the physical interpretation of these parameters.

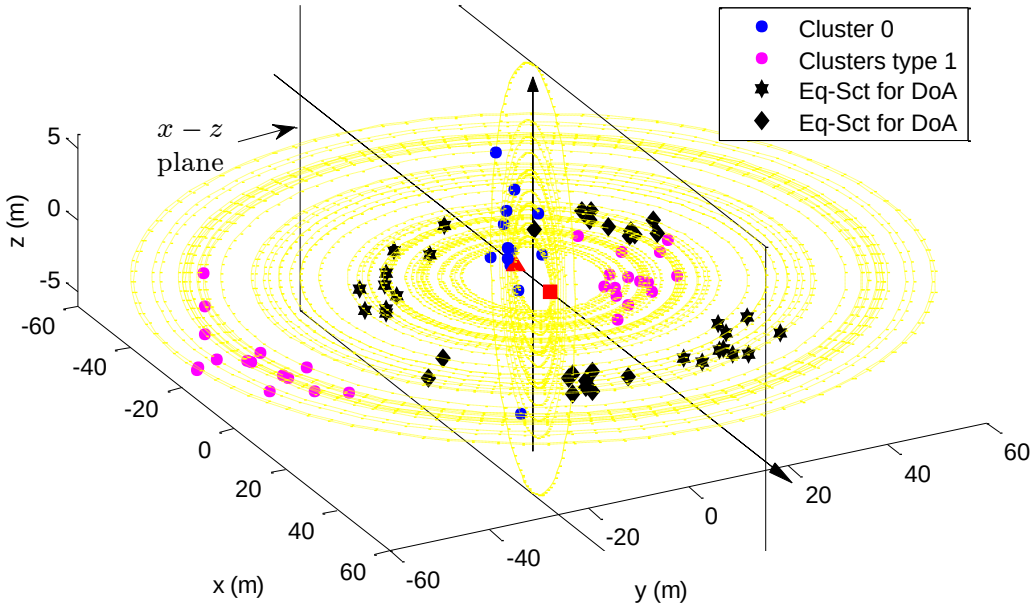

Figure 5-10: Scatterers for the sample channel presented in Figure 5-8.

Table 5-5: Configuration parameters for: the radio link and the transmitter and receiver arrays and routes.

Attribute	Parameter	Description	Sample value
Radio Link	`Fc`	Carrier frequency [GHz]	2
	`BW`	Frequency bandwidth [MHz]	200
	`Nf`	Number of frequency points	801
	`dTxRx`	Transmitter to receiver distance	13
Tx/Rx antenna array	`Nt/Nr`	Number of antennas	2
	`dTx` (Δ_{Tx}) `dRx` (Δ_{Rx})	Distance between antennas [wavelengths]	0.5
	`Tx_ang` (Ψ_{Tx}) `Rx_ang` (Ψ_{Rx})	Array orientation referred to *x*-axis [rad]	$\pi/2$
Tx/Rx route	`TxRt_dr` (Φ_{Tx}) `RxRt_dr` (Φ_{Rx})	Route direction referred to *x*-axis [rad]	$\pi/2$
	`TxRt_step` (δ_{Tx}) `RxRt_step` (δ_{Rx})	Route step (inter-snapshots space) [wavelengths]	0.25
	`TxRt_lgth` `RxRt_lgth`	Route length [wavelengths]	5

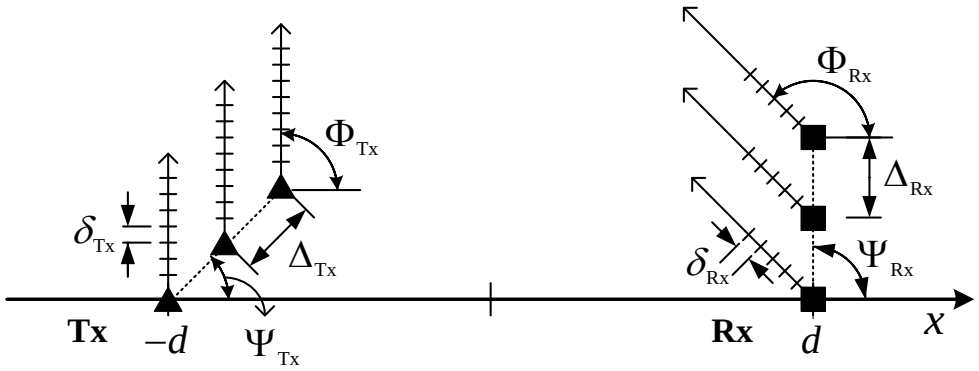

Figure 5-11: Geometry and physical interpretation for parameters in Table 5-5 specifying the transmitter and receiver antenna arrays and routes.

The simulation route is generated as follows: for each position of the transmitter, the receiver performs an entire scan of its path; then, the transmitter advances one position in its route and the receiver performs another scan in the opposite direction; until the transmitter reaches all considered simulation positions. This provides approximately $N_S^{Tx} \times N_S^{Rx}$ channel realizations, where N_S^{Tx} and N_S^{Rx} are, respectively, the number of

samples in transmitter and receiver routes (these correspond roughly to the route length divided by the route step – cf. Table 5-5). Nevertheless, if other route schemes should be considered, this can be done by updating only the routine which generates the simulation paths.

5.3.4. Obtaining the Frequency Responses Matrix Series (Step 5)

The channel frequency response is computed, at each sampling point and for each possible combination of input and output antennas, by means of simple ray tracing mechanism, considering the direct ray and every scatterer contribution, which is expressed as

$$h_{ij}(n) = \underbrace{\alpha_{\mathrm{D}} \exp\left(-\mathrm{j}\frac{2\pi}{\lambda}\mathrm{d}_0^{ij}(n)\right)}_{\text{Direct ray}} + \underbrace{\sum_{\ell=1}^{Ls} \alpha_\ell \exp\left(-\mathrm{j}\frac{2\pi}{\lambda}\left(\mathrm{d}_1^{\ell j}(n) + \mathrm{d}_2^{i\ell}(n)\right) + \varphi_\ell\right)}_{\text{Scatterers contributions}}, \tag{5.14}$$

where, $h_{ij}(n)$ designates the frequency response from the *j*-th transmit antenna to the *i*-th receive antenna, at the *n*-th sampling point; *Ls* denotes the number of scatterers; α_ℓ and φ_ℓ are, respectively, the amplitude and phase of the ℓ-th scatterer. In addition, $\mathrm{d}_0^{ij} = \mathrm{d}_{\mathrm{Tx}j-\mathrm{Rx}i}$ represents the distance from the *j*-th transmit antenna to the *i*-th receive antenna; $\mathrm{d}_1^{\ell j} = \mathrm{d}_{\mathrm{Tx}j-\mathrm{ScDoD}\ell}$ denotes the distance from the *j*-th transmit antenna to the ℓ-th scatterer and $\mathrm{d}_2^{i\ell} = \mathrm{d}_{\mathrm{ScDoA}\ell-\mathrm{Rx}i}$ designates the distance from the ℓ-th scatterer to the *i*-th receive antenna; all at the *n*-th sampling point.

For single-bounce scatterers (those corresponding to cluster 0, excluding the direct ray, and to clusters type 1), $\mathrm{d}_1^{\ell j}$ and $\mathrm{d}_2^{i\ell}$ are computed using the same scatterer. Yet, for multiple-bounce scatterers $\mathrm{d}_1^{\ell j}$ is calculated using the equivalent scatterer found from DoD, while $\mathrm{d}_2^{i\ell}$ is obtained using the equivalent scatterer established from DoA.

In the left-side of Figure 5-12 is illustrated the assumed propagation mechanism for clusters type 1 (single-bounce): $\mathrm{d}_1^{\ell j} + \mathrm{d}_2^{i\ell}$ is represented by gray solid lines departing from the transmitter and reaching the receiver through one scatterer.

In the right-side of Figure 5-12, is exemplified the propagation process for cluster type 2 (multiple-bounce): $\mathrm{d}_1^{\ell j}$ corresponds to the gray solid line departing from the transmitter to one hexagram shaped scatterer, while $\mathrm{d}_2^{i\ell}$ corresponds to gray solid line departing from one diamond shaped scatterer to the receiver. Each channel contribution is described by using two linked equivalent scatterers: this one-to-one association is represented by a gray dotted line.

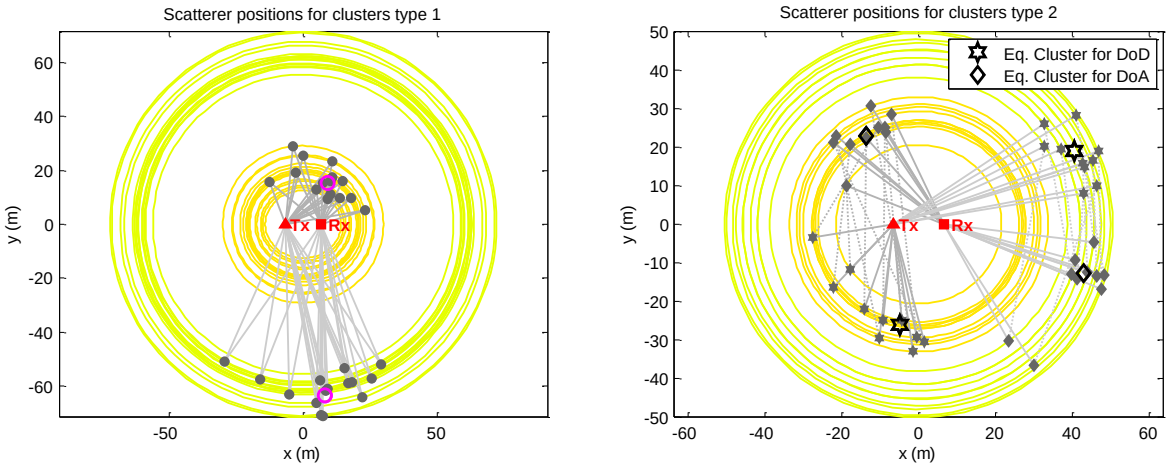

Figure 5-12: Propagation mechanism for single-bounce (right) and multiple-bounce scatterers (left). Scatterers generated for the sample channel presented in Figure 5-8.

5.3.5. Simulator Sample Results

This section presents some output results obtained for the channel being used as example in the previous sections (corresponding to Figure 5-8 and Figure 5-10). Simulation parameters for the radio link and for the transmitter and receiver arrays and routes were used as indicated in Table 5-5. Chosen results are divided into SISO outputs and MIMO outputs.

In addition, simulator outputs for one OLoS sample channel are offered in appendix B. This simulation has also used the parameters specified in Table 5-5.

SISO outputs

In the left-side of Figure 5-13 it is presented the received amplitude, for all channel realizations and frequencies, corresponding to one transmit-receive antenna pair (h_{11}). In the right-side of this figure it can be observed the channel series only for f =2 GHz, while in the left-side of Figure 5-14 it is shown the frequency response obtained for one single channel realization (one sampling position or snapshot). Additionally, in the right-side of Figure 5-14 it is displayed the channel impulse response corresponding to this channel realization, which has been obtained by using the IFFT algorithm.

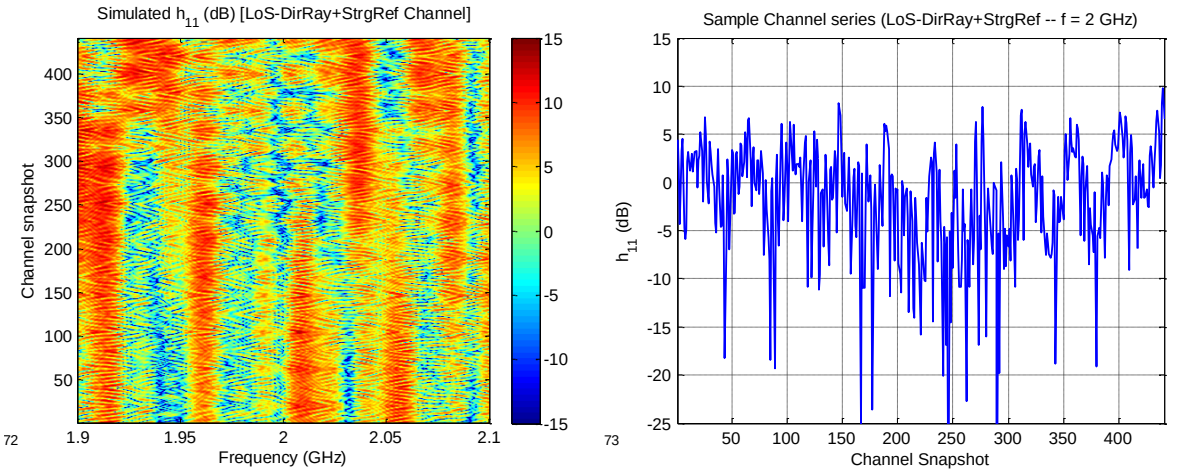

Figure 5-13: Received amplitude for the generated sample channel. **Left:** Complete data set generated. **Right:** Channel realization series for f =2 GHz.

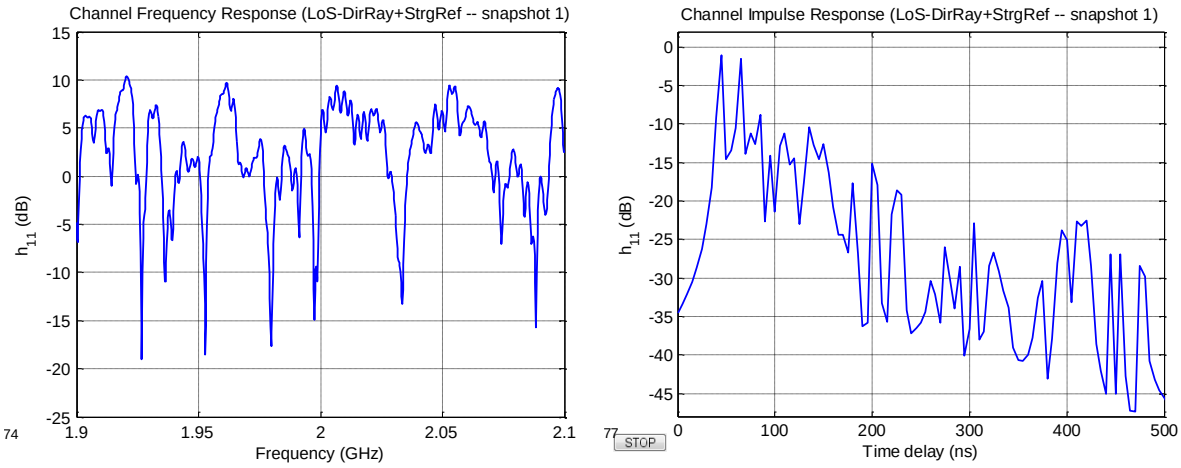

Figure 5-14: One realization. **Left:** Frequency response. **Right:** Impulse response (obtained by IFFT).

Figure 5-15 exhibits the channel autocorrelations: the left-side contains the frequency autocorrelation of the channel realization shown in left-side of Figure 5-14 and in the right-side, the spatial autocorrelation corresponding (partially) to the channel realization series presented in the right-side of Figure 5-13. Indeed, the spatial autocorrelation has been computed considering only one receiver route scan and using a smaller inter-samples separation, so that the autocorrelation function is properly displayed. Also represented in this figure is the zero order Bessel function of the first kind, which theoretically rules the spatial autocorrelation function: a reasonable agreement is found for this frequency.

As discussed in section 3.1, the correlation bandwidth of the channel may be computed from the frequency autocorrelation. On the other hand, the spatial autocorrelation provides information on the correlation level for a given spatial separation or the minimum spatial separation to achieve a given correlation threshold.

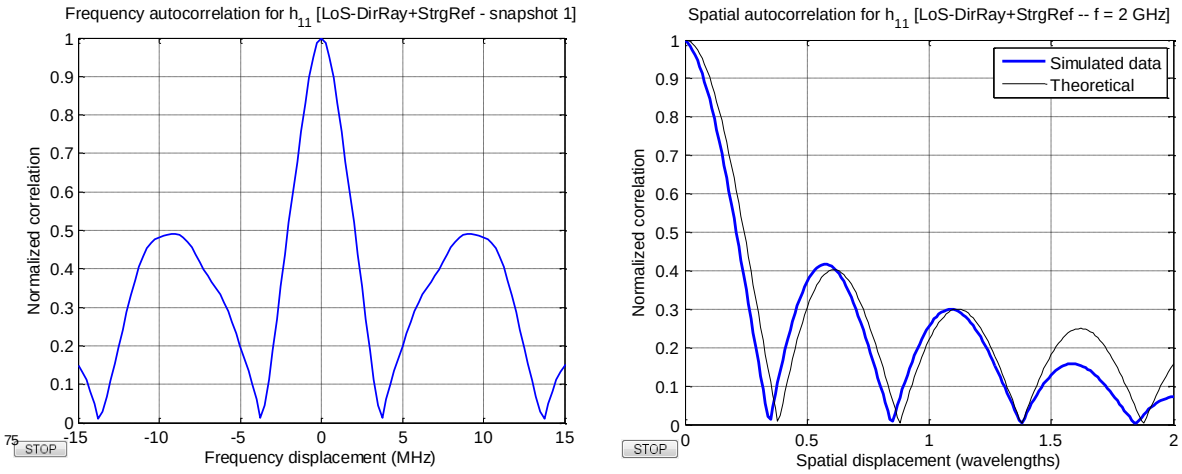

Figure 5-15: Channel autocorrelation. **Left:** Frequency domain. **Right:** Spatial domain.

MIMO outputs

The left-side of Figure 5-16 presents the six channel cross-correlations: these are computed, for each frequency, as the correlation between each series pair of the channel matrix entries. For a 2x2 MIMO setup it is possible to compute six channel cross-correlations. It is expected that two of these depend only on the separation at the receiver side, where each one considers a fixed transmitter and the two receivers: these two – $R_{h11,h21}$ and $R_{h12,h22}$ – are represented by the yellow-red pair, respectively, and should be roughly the same (because when considering one transmitter or the other would not have much influence).

In a similar manner, there are two comparable cross-correlation values depending only on the separation at the transmitter side (where each one considers a fixed receiver and the two transmitters): these two – $R_{h11,h12}$ and $R_{h21,h22}$ – correspond to the cyan-blue pair. For each pair it is, actually, observed that cross-correlations are similar to each other and similar to those of the other pair, as well. This result is comprehensible given the symmetry of the simulated MIMO arrangement (same inter-antenna spacing and also same number of antennas, at the transmitter and receiver sides).

Moreover, there are two cross-correlations depending on the separation, either at the transmitter either at the receiver sides: $R_{h11,h22}$ and $R_{h21,h12}$. These are represented in green and black, respectively, and present also, approximately, analogous behavior to each other (i.e., the same frequency comportment with approximately the same levels).

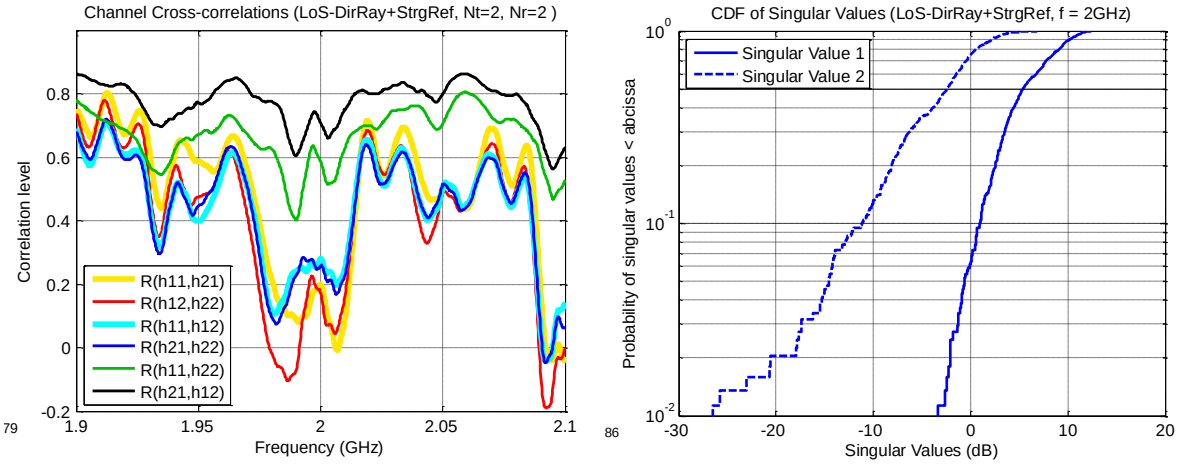

Figure 5-16: **Left:** Channel cross-correlations. **Right:** CDF of the channel singular values for f =2 GHz.

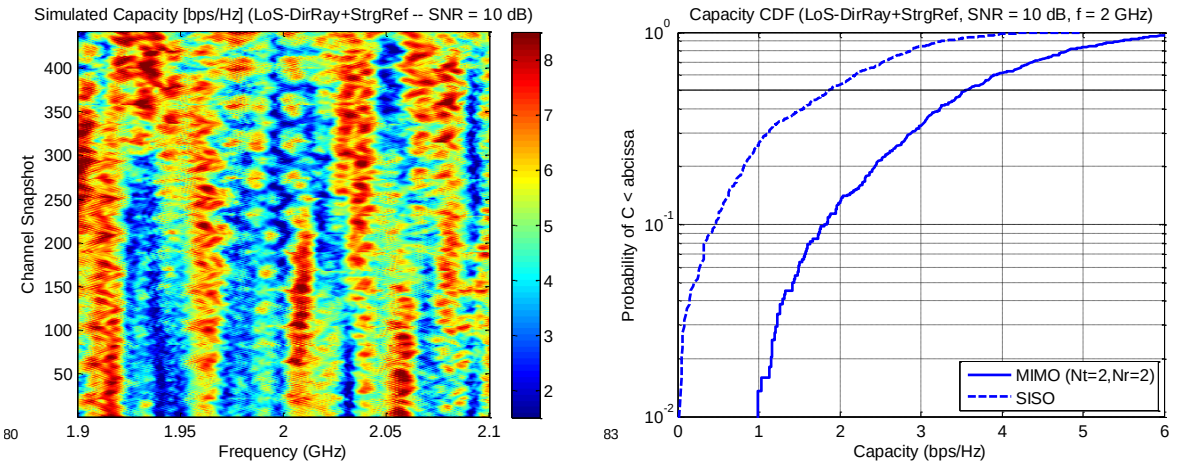

Figure 5-17: Channel capacity. **Left:** Global data set. **Right:** Capacity CDF for f =2 GHz.

Series of the two singular values of each 2x2 MIMO channel matrix, for each frequency have been computed. In the right-side of Figure 5-16 the corresponding CDFs are given while in the left-side of Figure 5-17 it is displayed the instantaneous capacity for the global data set (all frequencies and channel realizations), considering a SNR of 10 dB. In the right-side of the same figure the corresponding CDF for f =2 GHz is presented, where it is also included the CDF of the SISO capacity computed using one transmit-receive antenna pair (h_{11}).

Ergodic capacities, corresponding to the right-side of Figure 5-17 are, respectively for MIMO and SISO, 3.6 bps/Hz and 1.9 bps/Hz, providing a capacity gain of about 1.9, almost achieving, for this frequency, the theoretical linear capacity increase given by $r = \min(Nr, Nt) = 2$. Nevertheless, if similar investigations are made for f =1.9 GHz (for

example), corresponding results are, respectively for MIMO and SISO, 6.1 bps/Hz and 3.7 bps/Hz: capacity gain has slightly decreased, but the ergodic capacity has effectively increased. The capacity increase for this frequency may be explained because the corresponding channel amplitude seems to be, generally, higher than that obtained for the channel corresponding to f =2 GHz (cf. with the left-sides of Figure 5-13 and Figure 5-17 the stain of red is greater for 1.9 GHz than for 2 GHz, which, instead presents more blue). The slight decrease in the capacity gain may be explained by the increase presented by all cross-correlations (cf. with the left-side of Figure 5-16).

5.4. MIMO Measurement Campaign

The channel simulator developed in this work enables the characterization and analysis of the multipath MIMO channel. However, in order to perceive how accurately the channel is being described, the simulator must be, itself, assessed and validated. For this purpose, a MIMO measurement campaign, in the same propagation scenario, has been planned.

The SIMO measurement system, presented in section 3.2, has been modified in order to allow MIMO radio channel measurements: as shown in the left-side of Figure 5-18, the two linear positioning units have been detached. In addition, the software which controls the equipment, acquires and saves experimental data has been updated. By this way, the updated measurement system provides linear synthetic arrays both at the transmitter and receiver, thus, MIMO measurements. As the main measuring task is performed by the VNA under the control of the computer, the setup is easily interchanged from one configuration to the other by attaching or detaching the two positioning units.

The right-side of Figure 5-18 displays a photograph taken during one specific measurement. On the other hand, the left-side of Figure 5-19 presents the transmitter and receiver arrangement of positions, for all accomplished measurements. By observing this figure, it can be acknowledged that measurements were performed by placing the transmitter and the receiver exactly on the same positions as those used for SIMO measurements (cf. Figure 3-2). Moreover, for each arrangement, the same designation has been adopted. However, there are two SIMO arrangements (PAV 3 and PAV 5) that could not be repeated using the MIMO measurement setup, due to limitations on the length of the cables which feed the stepper motors.

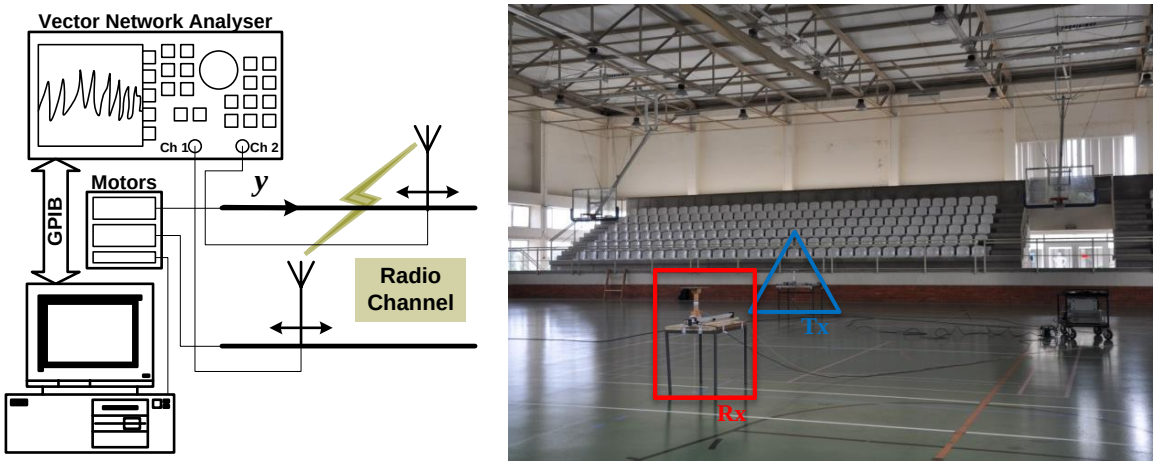

Figure 5-18: **Left:** Block diagram of the MIMO channel measurement system. **Right:** Photograph corresponding to the one measurement position ("PAV 10").

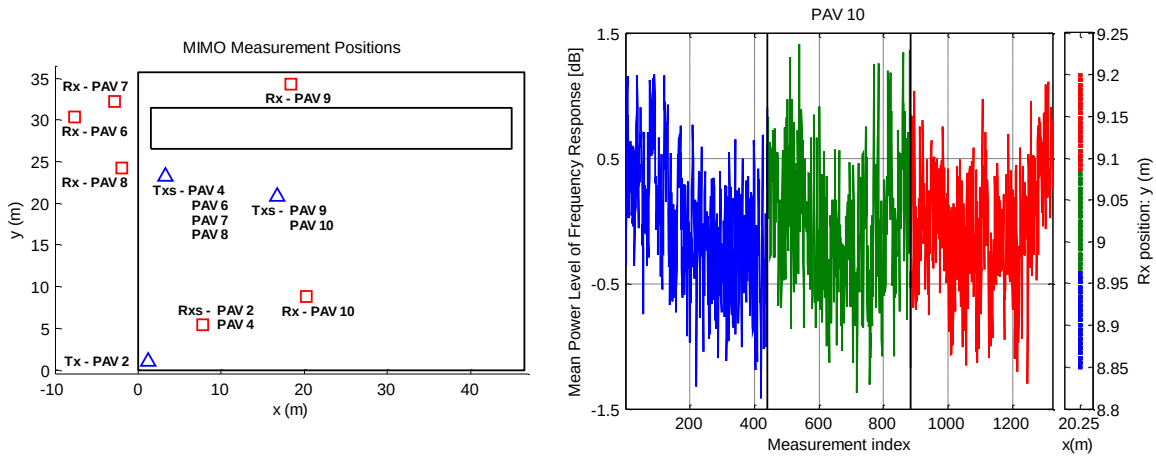

Figure 5-19: **Left:** Description of the MIMO measurement positions in the scenario. **Right:** Mean power level of each measured frequency response for the arrangement "PAV 10".

Transmitter and receiver were both equipped with one $\lambda/4$ monopole antenna (the same used on SIMO measurements). For each transmitter-receiver arrangement of positions, the frequency response of the time-invariant channel has been measured, spaced by $\lambda/4$ in the y-axis (at both sides), using 21 positions at the transmitter and 3×21 positions at the receiver. The RF bandwidth used was 200 MHz centered at 2 GHz and comprises 801 frequency sample points. Indeed, the length of each linear positioning unit is about 75 cm, which at 2 GHz represents 5λ, thus, allowing 21 samples if measurements are spaced by $\lambda/4$. Therefore, for each global measurement collection corresponding to one transmitter-receiver arrangement, the receiver positioning unit has been manually placed

three times, where each sub-collection delivers $21 \times 21 = 441$ frequency responses: for each of the 21 transmitter positions, the receiver performs an entire scan along the positioning unit. The channel transfer matrix, for different MIMO configurations, may be obtained by selecting the adequate sample points during post-processing.

The right-side of Figure 5-19 depicts the mean power level for all the $3 \times 441 = 1323$ frequency responses available corresponding to one transmitter-receiver arrangement, where each of the three sub-collections (each comprising 441 frequency responses), is identified by one color. Indeed, power levels presented in this figure were normalized so that the global mean power corresponds to 0 dB (actually, the measured mean power level is about −61 dB).

In addition, for some measuring positions, it has been observed a slight variation (about ±1 dB for this particular data set) in the mean power level corresponding to each sub-collection of frequency responses. This behavior may be due to mismatches in the cable junctions (particularly in the interface antenna-cable) caused by the antenna motion which drags and imposes some tension on the cables. In order to unify the mean power level for the three data sub-collections, each section has been adjusted individually.

5.5. Measurements Results vs Simulator Outputs

In this section, results obtained directly from the MIMO measurements are compared to the simulator outputs, for validation purposes. To accomplish a rationale comparison (i.e., rigorous and yet fair), the simulator is parameterized so it reproduces the structure of the measured channel conveniently. Therefore, instead of generating the cluster centroids randomly (using parameters presented in Table 5-3), these are alternatively established by consulting the database created with the clustered DCIRs and whose statistical analysis has been presented in section 5.2.

Regarding cluster 0, the database supplies the direct ray characterization, comprising its delay, τ_0, and power, $|\alpha_{\mathrm{D}}|^2$. Likewise, if a strong specular reflection is present, its delay and power are also specified. Similarly, the power of other MPCs belonging to this cluster is given, whereas their delay and azimuth are randomly drawn from the underlying statistical distributions as explained in section 5.3.1. Nevertheless, applicable parameters reported in Table 5-4 were correspondingly updated in order to reflect the characteristics of this specific measurement point.

For the remaining clusters, the database provides the cluster centroids. For clusters type 1, it stipulates the centroids delay τ_{ck}, DoA azimuth, ϕ_{ck}^{DoA}, and power, P_{ck}. For clusters type

2, it gives additionally, the centroid DoD azimuth, ϕ_{ck}^{DoD}. As in cluster 0, individual MPCs belonging to each cluster are then randomly drawn, once more, according to the assumed statistical distributions and as explained in section 5.3.1. Again, related parameters stated in Table 5-4 were consistently refreshed.

Furthermore, in order to exactly reproduce the measurement conditions, parameters in Table 5-5 may not be adjusted freely: namely, the transmitter and receiver routes and the arrangement of the antenna arrays must be compliant with the available measurements. This means, for example, that the minimum inter-antenna and inter-sampling separations, Δ_{Tx}, Δ_{Rx}, δ_{Tx} and δ_{Rx}, are constrained to $\lambda/4$, corresponding to the measurement separation. Aside from these restrictions, the remaining simulation steps (i.e., the generation of the channel scatterers and the computation of the frequency responses matrix) run exactly in the same way as for any other free simulation.

Results presented in this section concern the data set designated as "PAV 10", corresponding to a LoS plus strong reflection case. This data set has been used along this thesis to explain each step of the work carried out, so that a guiding thread is maintained. Figure 5-20 shows the generated channel for simulation of this measurement point: in the left-side of this figure it is presented the channel impulse response, while, in the right-side it may be observed the corresponding channel scattereres overlaid on the scenario layout (using the coordinate axes of Figure 5-9). By prescribing directly the cluster centroids for simulation, it becomes guaranteed a correct description of the main physical contributions from the propagation scenario.

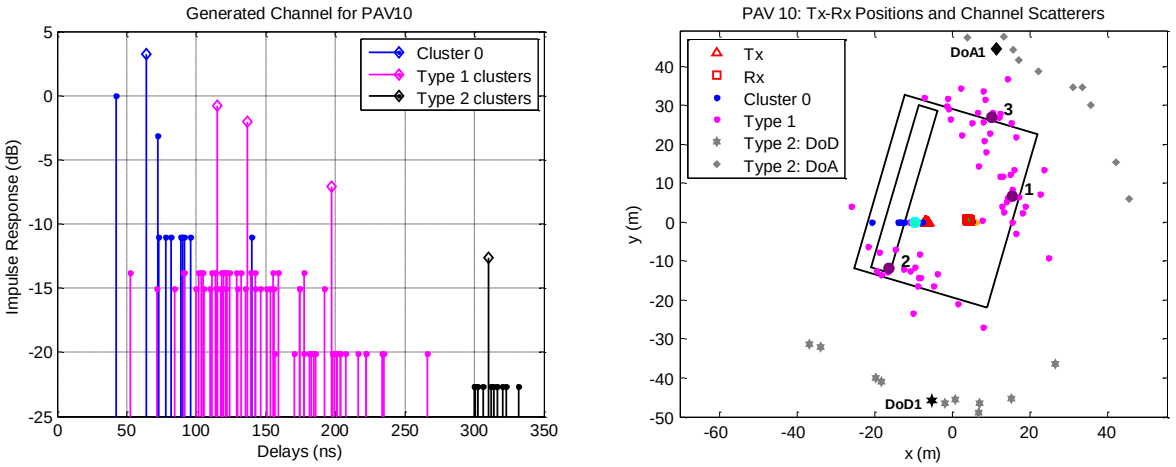

Figure 5-20: Generated channel for "PAV 10". **Left:** Channel MPCs. **Right:** Channel scatterers.

For this evaluation study, the transmitter and receiver number of antennas have been both set to $Nt = Nr = 2$; whereas parameters Δ_{Tx}, Δ_{Rx}, δ_{Tx} and δ_{Rx} were all set to $\lambda/4$, thus, providing the maximum number of channel realizations. Nevertheless, it has been decided to use only the red part of the data set presented in Figure 5-19 (comprising samples from a single data sub-collection), though, similar conclusions would be obtained if a different (or even more than one) sub-collection had been chosen.

Recalling the power reference established for simulations (0 dB for direct ray under LoS condition) and the adjustment made to the measurements (0 dB for mean power level) it can be easily concluded that measurements and simulations use different power references. For comparison purposes of certain features (received amplitude, impulse response, etc.) it is important to use the same reference level. One way of achieving this normalization is to find the power level of the direct ray for the measurements and bring it to the same level used in simulations (or vice-versa). However, the power level of the direct ray has been estimated from SIMO measurements and as referred before, even in MIMO measurements made in a single batch, some power fluctuations were observed. For this reason, it was preferred to adjust the mean power level by forcing the mean power level of measurements to match the simulations mean power level.

In the following, the validation of the channel simulator is given by evaluating the achieved channel characterization for SISO and for MIMO setups: measurements and the corresponding simulations results are compared, mainly using graphical arrangements. Given the high amount of available figures, some are instead presented in appendix C.

5.5.1. Assessment of the SISO Characterization

The left-side of Figure 5-21 presents the frequency response for a single channel realization (snapshot) and the right-side shows the channel realization series for 2 GHz. The CDFs of these specific data sets may be found in (appendix C) Figure C-2, whereas Figure C-1 shows the measured and simulated global data sets.

The frequency domain autocorrelation, corresponding to the frequency response shown in the left-side of Figure 5-21, is displayed also in the left-side of Figure 5-22: from this it is possible to evaluate the coherence bandwidth of the channel, for a given correlation level. For this specific channel realization and considering the 50% correlation level, the coherence bandwidth is about 1.96 MHz for measurements and 1.53 MHz for simulations. Indeed, for this channel realization simulations and measurements differ substantially, but by examining other channel realizations it can be concluded that this behavior is not systematic. The mean value of the coherence bandwidth has been found to be 1.63 MHz

for simulations and 1.69 MHz for measurements (deviation of 3.6%). The CDF of coherence bandwidths corresponding to the several channel realizations is given in left-side of Figure C-3.

The right-side of Figure 5-22 presents the spatial autocorrelation of the channel realization shown in the right-side of Figure 5-21 (f = 2 GHz). Again, as for the simulations presented in section 5.3.5, to achieve an adequate sampling so that the autocorrelation function is correctly displayed, the channel series had been simulated using a smaller inter-samples separation. However, measurements were acquired using $\lambda/4$ as sample spacing; therefore an interpolation is performed using the data points available from measurements. Similarly to the simulations presented before, in this figure is represented (black line) the zero order Bessel function of first kind. A reasonable agreement between the three curves is observed. Additionally, Figure 5-23 exhibits the spatial autocorrelation for the entire set of sample frequencies available: similar structures are observed, but the correlation (relative) side maxima tend to be more exacerbated for simulation results than in the measurements. On the other hand, the main lobe is slightly larger for measurements: on average, for a displacement of $\lambda/4$, the correlation level is about 0.28 for simulations and 0.32 for measurements (cf. with right-side of Figure C-3).

Figure 5-24 offers time domain results: in the left-side of this figure it is given the channel impulse response for the channel realization presented in the left-side of Figure 5-21 (obtained by IFFT); whereas the right-side shows the delay spread CDF computed from impulse responses as the one presented in the left-side (delay spread has been computed by considering only impulse response points above the threshold represented by the black line, corresponding, in this case, to −33 dB). Obtained average delay spread is 56.4 ns for simulations and 58.6 ns for measurements.

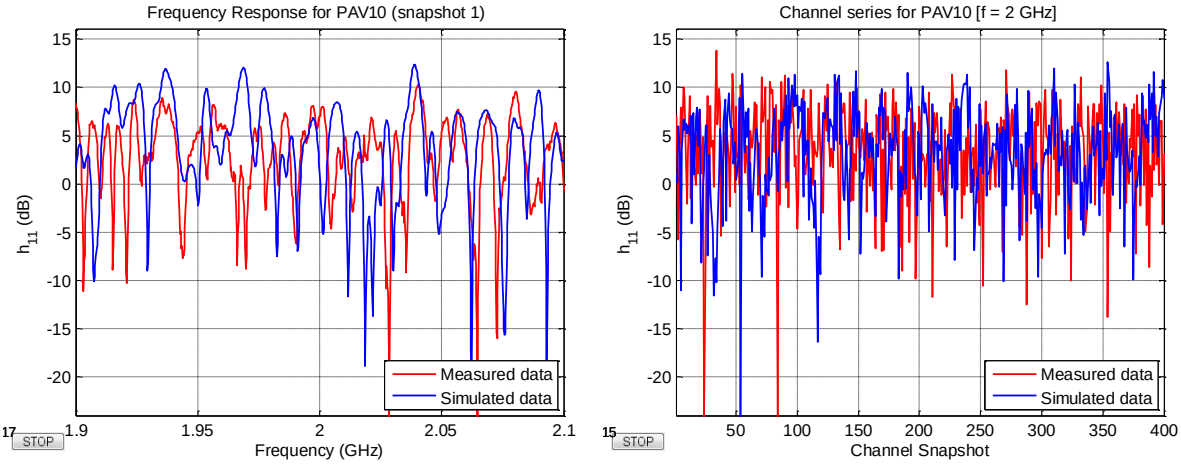

Figure 5-21: Received amplitude (one antenna) for "PAV 10". **Left:** Frequency response of one channel realization. **Right:** Channel realization series for f = 2 GHz.

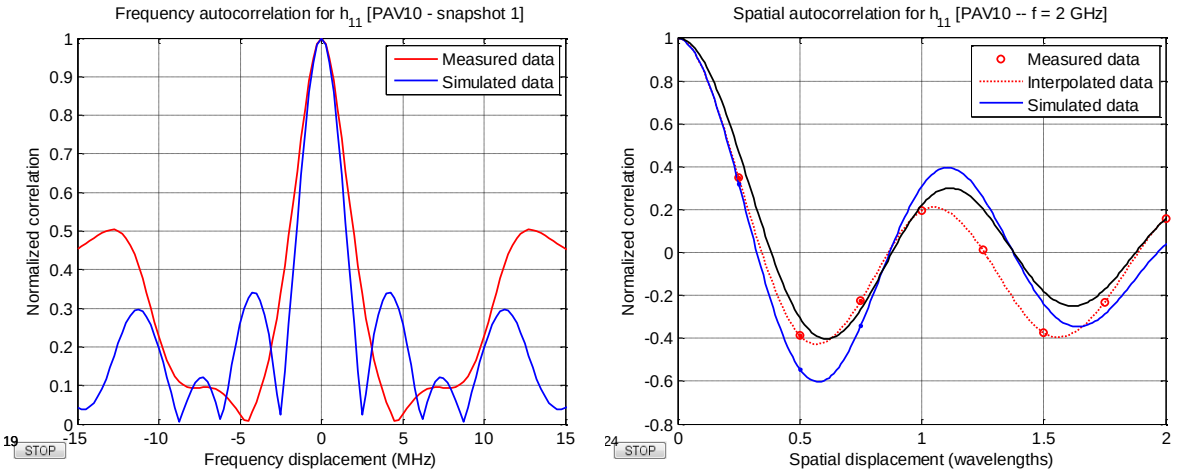

Figure 5-22: Channel autocorrelation. **Left:** Frequency domain autocorrelation (one channel realization). **Right:** Spatial domain autocorrelation for f = 2 GHz.

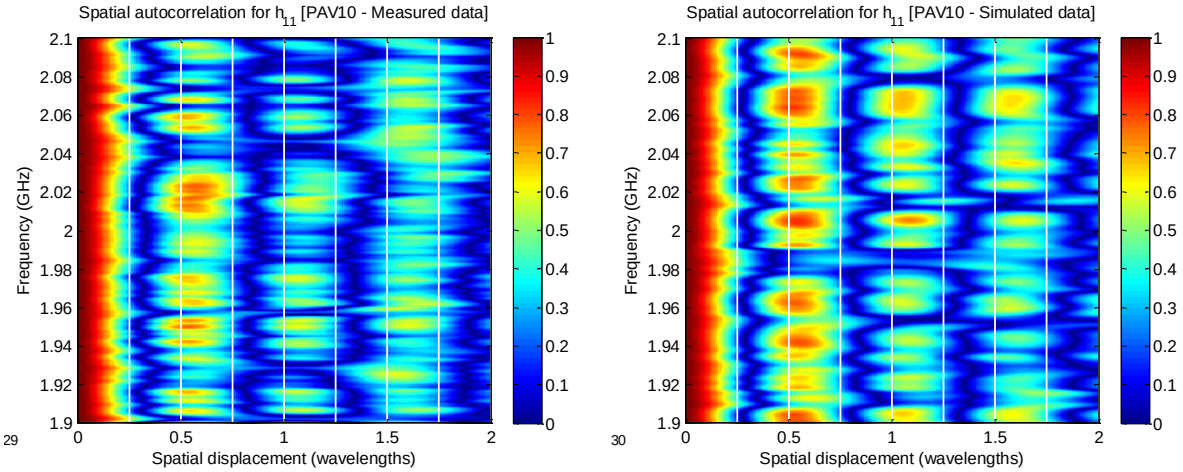

Figure 5-23: Spatial autocorrelation for all frequencies available.

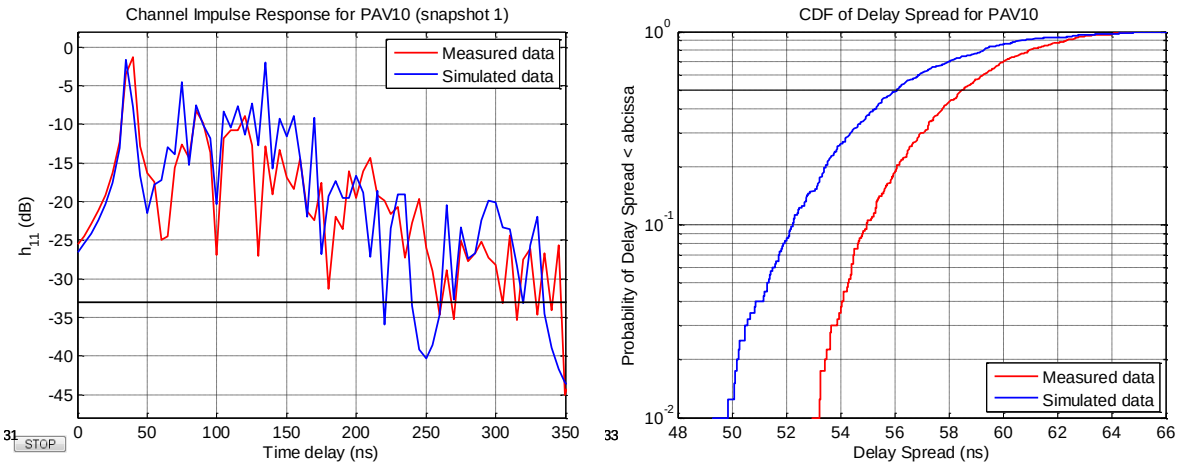

Figure 5-24: **Left:** Channel impulse response (one snapshot). **Right:** CDF of delay spread.

Taking into consideration results presented in this subsection, it may be considered that the channel simulator is able to characterize the SISO channel in a satisfactory way. Although some acceptable deviations, the results obtained directly from measurements and those obtained from simulations present, for all investigated features, similar behavior. Additionally, observed deviations were about 5 % and regularly less 10 %.

5.5.2. Assessment of the MIMO Characterization

Figure 5-25 depicts the channel cross-correlations. The two analogous cross-correlation values depending only on the separation at the receiver side (those considering a fixed transmitter and the two receivers) are represented by the yellow-red pair for measurements and the cyan-blue pair for simulations, in the topmost graphic. Likewise, the two comparable cross-correlation values depending only on the separation at the transmitter side (those where each one considers a fixed receiver and the two transmitters), appear in the middle and use also the same color scheme, for measurements and simulations (as used for cross-correlations depending only on the receiver side separation).

For both cross-correlations mentioned, it may be observed that measurements and simulations present analogous correlation levels. Once more, as for the simulations presented before (section 5.3.5), cross-correlations depending only on the receiver side separation present very similar behavior to those depending only on the transmitter side separation. Again, this observation may be justified with the symmetry of the simulated MIMO arrangement (same inter-antenna spacing and also same number of antennas, at the transmitter and receiver sides).

For cross-correlations depending on the separation, either at the transmitter either at the receiver sides, the concordance between measurements and simulations is not so good. A careful analysis evidences that for one of these two cross-correlations, simulation results tend to be overestimated, whereas for the other simulation results tend to be underestimated. Consequently, this means that the MIMO channel characterization in global terms (singular values, capacity gain, etc.), may not be compromised.

In the left-side of Figure 5-26 are displayed the CDFs of the singular values corresponding to the channel realization series for 2 GHz, while in the right-side of this figure the CDFs of the channel capacity, for the same channel realization series, are given (cf. Figure C-4). In addition, the right-side of Figure 5-26 also presents, for comparison purposes, the SISO channel capacity: it is clear that, for this specific channel, the capacity gain, although close, does not achieve the theoretical value given by $r = \min(Nr, Nt) = 2$ (capacity increase found is about 1.7, but recall that this is a LoS channel).

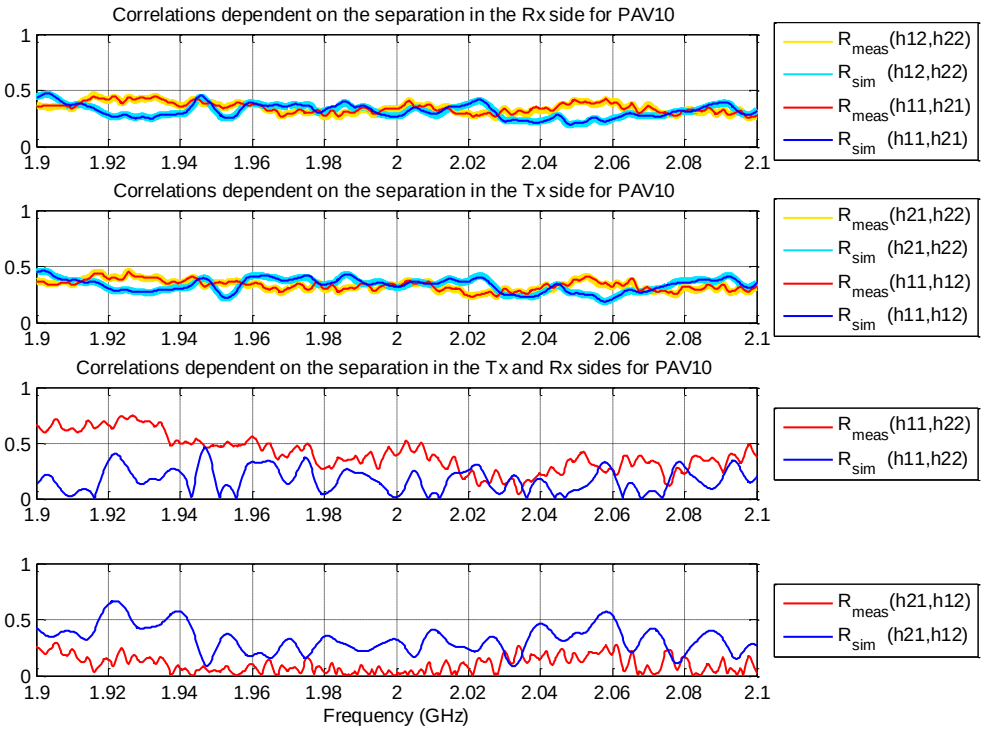

Figure 5-25: Channel cross-correlations.

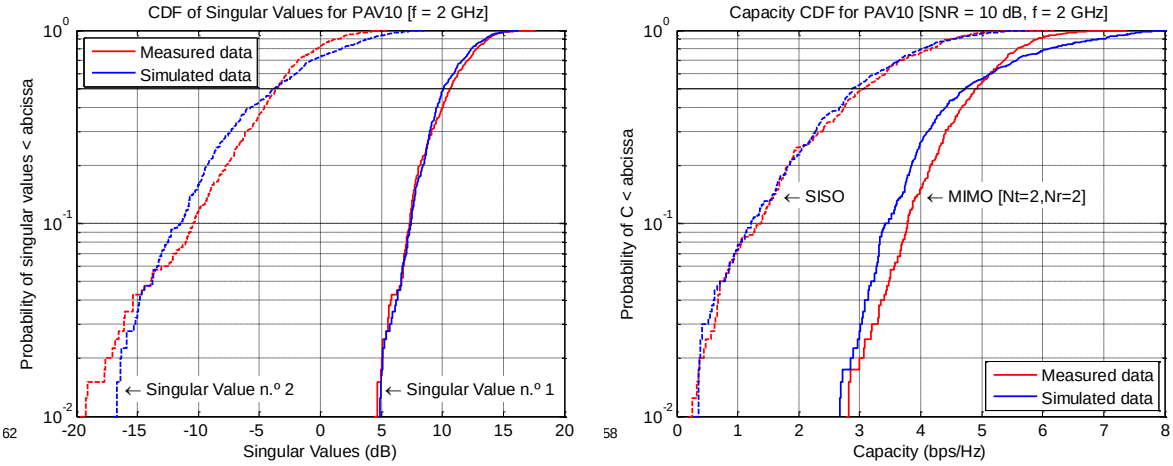

Figure 5-26: CDFs of channel realization series for f = 2 GHz (cf. Figure C-4). **Left:** CDF of singular values. **Right:** CDF of capacity.

Globally, it can be perceived a satisfactory and realistic description of the channel. Again, as for the SISO characterization, acceptable deviations (roughly about 5%), between measurements and simulations, were found. Indeed, it has been found that if the SISO characterization of the channel succeeds; then the subsequent MIMO channel description obtained is also adequate. Indubitably, the SISO (directional) channel already incorporates the relevant "*signature codes*" that determine the channel behavior. These engraved

"*signature codes*" are, essentially, the contributions from the scatterers present in the propagation scenario. By characterizing the channel scatterers properly (complex amplitude and position), the question becomes merely of geometric nature. Consequently, evolving from SISO to MIMO setups represents, essentially, a problem of spatial sampling.

5.6. Final Comments on the Modeling Methodology

Results and considerations presented above substantiate (once more) the geometry-based stochastic modeling methodology proposed in this work. Recall that, for validation purposes, only the cluster centroids and the respective power were supplied, whereas individual MPCs were randomly generated. Nevertheless, these prescribed data (for validation) may also be randomly generated. If realistic and well parameterized rules are available, then, aside from statistical variability (inherent to any random draw), the generated channel MPCs will be, as well, realistic and ultimately, also the corresponding generated scatterers.

As just explained, the more realistic are the underlying statistics and rules characterizing the channel the more realistic would be the simulation outputs. If different propagation scenarios should be characterized, an exploratory analysis of corresponding available measurements must be carried out. However, as the problem of the radio channel characterization has been deeply investigated, it may be possible to make use of the knowledge available in the literature.

On the other hand, the validation procedure has opened the possibility of directly prescribe some channel data (cluster centroids). Therefore, this opportunity may also be used, particularly, if important channel contributions may be easily estimated by a simple analysis of the propagation scenario or if they can be extracted from available measurement data or results reported in the literature.

Chapter 6

Conclusion

Capabilities of MIMO systems are limited by the characteristics of the radio channel. In fact, the benefits of MIMO (spatial multiplexing, spatial diversity and beamforming) depend on the structure of the underlying radio multipath propagation.

This work represented an effort to give a contribution to the characterization of the radio channel for MIMO systems. Some of the existing physical channel models assume that MPCs arrive in clusters, i.e., groups of MPCs showing analogous parameters such as delay, DoA and DoD. Actually, results from measured channels show that MPCs often appear in clusters and usually, this may be confirmed by a simple visual inspection. However, in order to accurately describe the relevant characteristics of the clusters, such models may be parameterized by extracting the information from experimental data. On the other hand, the consciousness that the channel properties are intrinsically ruled by the interactions between the transmitted signal and the scatterers existent in the propagation scenario, motivated the entire approach followed. The work main steps and the adopted methodology are, thus, delineated:

- The directional channel has been described using experimental measurements of the double-directional channel (each double-directional measurement comprises one forward direction plus one reverse direction SIMO measurements). By using a high resolution algorithm, the most relevant MPCs (delay, direction of arrival and complex amplitude) of the channel were obtained, from SIMO measurements.

- Afterwards, using a clustering algorithm, MPCs composing each directional channel impulse response were grouped into clusters and then, each pair of clustered DCIRs (composing one double-directional data set) were, jointly, analyzed physically, so that each cluster is further classified according to the type of propagation mechanism that it represents (single- or multiple-bounce).
- Finally, a statistical analysis of the structured database has been performed: rules, underlying statistics and corresponding parameterization values have been extracted. The gathered data has been used to parameterize the channel simulator, which uses it in order to randomly generate a set of MPCs that reproduce the most significant features of the channel; from these the channel scatterers are obtained and lastly, the channel transfer matrix is computed by considering the interaction of the transmitted signal with each scatterer.

6.1. Final Remarks

In the following, the main achievements presented in each chapter are summarized. Chapter 2 presents the fundamental results from information theory, which motivated the interest on MIMO systems, and a discussion about some of their potential benefits. Still in this chapter, the most important aspects and models for the MIMO channel description are reviewed.

Chapter 3 opens with a short outline of the wideband radio channel characterization, then, the SIMO measurement system and the measurement campaign, carried out inside a sports hall, are described. Subsequently, the SAGE algorithm, which, among some high resolution tools available, has been chosen for estimating the channel MPCs, is presented. The ability of the SAGE algorithm in retrieving the superimposed signals (MPCs) has been examined using synthetic data, which was generated with the extended Saleh-Valenzuela model. Results on this performance study evidenced that, occasionally, the algorithm fails to estimate some of the most delayed and lower power MPCs and provides, in their place, some fictitious MPCs. As the number of MPCs in the channel and the power decay increases, the number of MPCs whose estimate is lost increases and therefore, the number of fictitious MPCs retrieved also increases. Nevertheless, the lost MPCs are those with less power and thus, less relevant in the channel characterization. Despite these observations suggest some failures, the estimates obtained for the directional impulse responses were considered satisfactory, so globally, this tool has been considered adequate to be employed with experimental data.

In chapter 4, the data classification problem is addressed and starts with a brief review of the clustering algorithms, focusing mainly on the selected algorithm: a version of the K-means algorithm (KPM algorithm), which also uses the power of the MPCs when performing the clustering, has been used. The most pertinent issues, in the global clustering framework, comprise: the selection of a measure for evaluating the distance between MPCs; the initialization procedure; and cluster validation (i.e., the estimation of the number of clusters in a given data set). Although it has been found very useful tools in the literature, some original contributions were also included in the global framework, namely, in the initialization procedure and in the cluster validation steps. These contributions were, partially, motivated by the results of a very complete performance study that has been carried out, using synthetic data. The clustering framework implemented was then applied to the DCIRs estimated from measurements, in the previous chapter (chapter 3), using the SAGE algorithm. To close, this chapter also presents a physical analysis of the clustered DCIRs, where further classification of each cluster of the channel is accomplished. This classification has been achieved by relating each cluster delay and azimuth to the objects in the scenario and by combining simultaneously the information of the two single-directional measurements, which compose one double-directional measurement. Thereby, the type of interaction that each cluster represents (direct ray, single-bounce or multiple-bounce) is identified and a linkage between each forward and reverse measurement pairs is attained.

At last, in chapter 5 a set of assumptions are postulated, which include rules and underlying statistical distributions governing the channel structure in terms of cluster centroids and individual MPCs (inside clusters). These assumptions allowed the developing of the channel simulator for MIMO systems that has been validated using MIMO measurements carried out in the same scenario. The validation of the channel simulator consisted of a comprehensive comparison (including SISO and MIMO evaluation measures) between measurements results and simulator outputs. In general terms and despite some acceptable deviations between measurements and simulations, the achieved characterization of the channel may be considered very satisfactory. Another important conclusion is that as long as the channel scatterers are accurately characterized, the subsequent channel properties will be also correctly described, because the channel scatterers definitely determine the intrinsic channel properties. In this case, the channel characterization (for SISO to MIMO systems) is generically a geometric problem.

6.2. Future Work

The present work may be enriched by considering improvements of practical nature, as software/programming enhancements of the simulator developed and also, enlargements related with the extent of application. Among possible advances it can be referred:

- To attain a friendly data input into the simulator. Indeed, there is a significant volume of data that must be defined in order to run the channel simulator. Default parameters were included within the programming routines, but, it would be desirable to have an agreeable way of changing these parameters (so that different configurations can be easily interchanged). The best solution it would be to have a graphical user interface running on top of the routines already implemented. This graphical interface could be thought to provide also amenable visualization and analysis of the simulator outputs.
- The available parameterization data could be enlarged, so that other scenarios or environments are considered. The idea would be to provide typical sets of parameters (as those given for the scenario contemplated in this thesis) so the simulator could be used more extensively. This could be achieved by performing new measurement campaigns and undertake an exploratory analysis similar to that present in this thesis. Alternatively, it may be possible to make use of the knowledge available in the literature. On the other hand, it may be possible to estimate important channel contributions by a simple analysis of the propagation scenario allowing to directly prescribing the cluster centroids (as made in the validation).
- The computation of channel matrix is being already performed using 3-D coordinates, but, the scatterers placement (in the scenario) considers only 2-D information (DoAs and DoDs correspond to azimuths). If 3-D DoAs and DoDs are available (comprising azimuth and elevation), the routine for the scatterers placement could be updated and an even more realistic description of the channel scatteres could be achieved.
- Finally, the channel characterization could be made polarization dependent.

Appendix A

Method for Generating Random Variables

The CDF transformation method [101] assumes a random variable, *U*, uniformly distributed in the interval $[0,1]$. Let $F_X(x)$ be the CDF of the random variable that must be generated. Consider the random variable, $Z = F_X^{-1}(U)$, where $F^{-1}(x)$ represents the inverse function of $F(x)$. Thus, first *U* is selected and then *Z* is found as indicated in Figure A-1. The CDF of *Z* is

$$P[Z \le x] = P\left[F_X^{-1}(U) \le x\right] = P\left[U \le F_X(x)\right]. \tag{A.1}$$

Since U is uniformly distributed in $[0,1]$ and if $0 \le h \le 1$, then $P[U \le h] = h$, consequently, $P[Z \le x] = F_X(x)$, so $Z = F_X^{-1}(U)$ has the desired CDF.

Exponential distribution: The CDF of a random variable *X* exponentially distributed is given by

$$F_X(x) = 1 - \exp\left(-\frac{x}{\beta}\right), \quad x \ge 0, \tag{A.2}$$

where $\beta > 0$ is the scale parameter. The expected value of *X*, is $E[X] = \beta$ and the variance is $\mathrm{var}[X] = \beta^2$ (so, the standard deviation is $\sigma = \beta$).

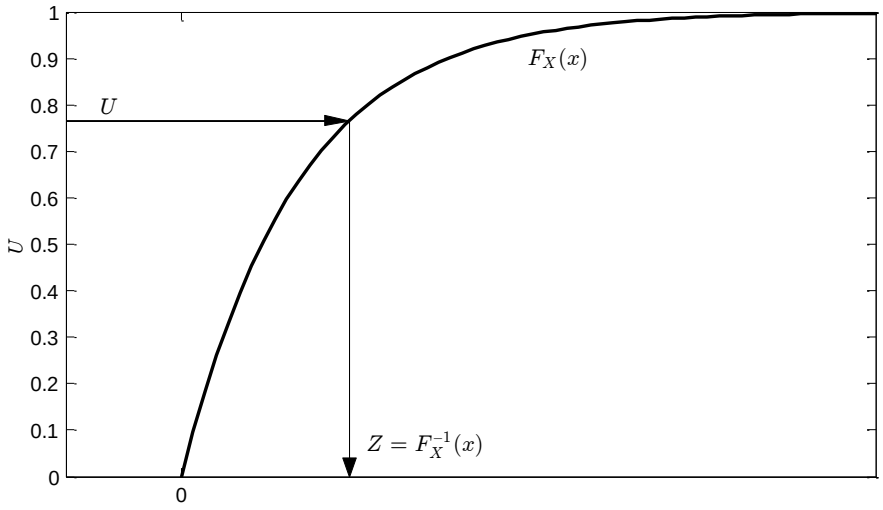

Figure A-1: Transformation method for generating a random variable with CDF $F_X(x)$.

An exponential random variable may be generated by inverting the following expression

$$U = F_X(x) = 1 - \exp\left(-\frac{x}{\beta}\right), \tag{A.3}$$

which results

$$X = -\beta \ln(1-U), \tag{A.4}$$

where $\ln(\bullet)$ denotes the natural logarithm function. Note that as U is uniformly distributed in $[0,1]$, then $1-U$ is also uniformly distributed in the same interval, so the simpler expression $X = -\beta \cdot \ln(U)$ may be used instead.

Laplace distribution: The CDF of a random variable X, following a Laplace distribution with parameters μ and b, is expressed as

$$F_X(x) = \begin{cases} \frac{1}{2}\exp\left(\frac{x-\mu}{b}\right), & x < \mu \\ 1 - \frac{1}{2}\exp\left(-\frac{x-\mu}{b}\right), & x \geq \mu \end{cases}, \tag{A.5}$$

with μ a location parameter and $b \geq 0$ a scale parameter. The expected value of X, is $E[X] = \mu$ and the variance is $\text{var}[X] = 2b^2$ (thus, the standard deviation is $\sigma = \sqrt{2}b$). The CDF of the random variable X may be observed in Figure A-2.

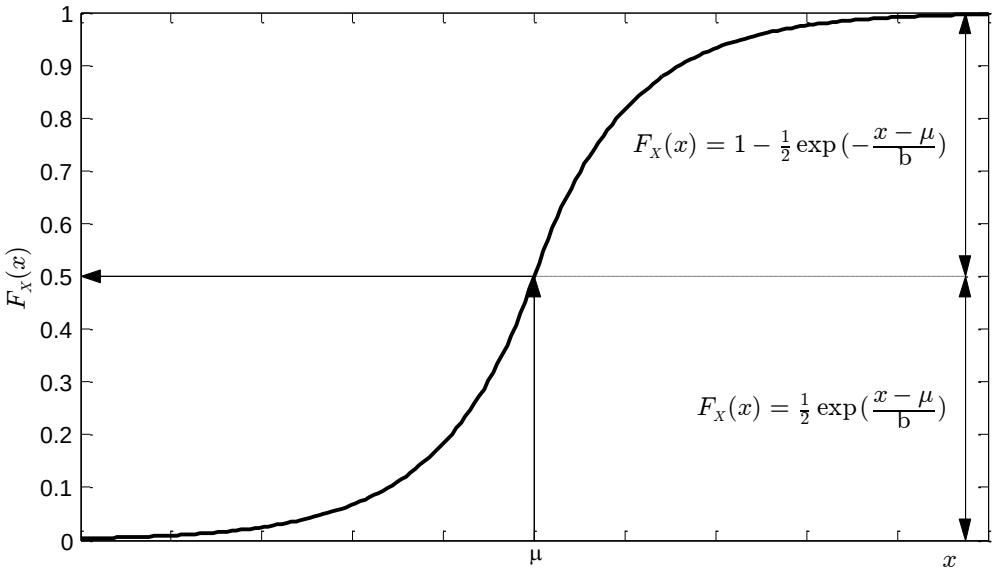

Figure A-2: CDF a random variable following a Laplace distribution with parameters μ and b.

To generate random variables that follow a Laplace distribution the CDF transformation method may be applied as in the previous case of the exponential distribution. But, in this case the CDF has two branches as illustrated in Figure A-2, therefore the inverse function for each branch must be found and, additionally, the variable U must be split into two uniform variables, U_1 and U_2, covering the intervals $[0, ½[$ and $[½, 1]$, respectively. By inverting

$$U_1 = \frac{1}{2}\exp\left(\frac{x-\mu}{b}\right), \tag{A.6}$$

and

$$U_2 = 1-\frac{1}{2}\exp\left(-\frac{x-\mu}{b}\right), \tag{A.7}$$

results

$$X_1 = \mu + b\cdot\ln(2U_1), \tag{A.8}$$

and

$$X_2 = \mu - b\cdot\ln(2(1-U_2)), \tag{A.9}$$

where $2U_1$ and $2(1-U_2)$ are both uniformly distributed in the interval $[0,1]$. Furthermore, consider the following change of variables

$$\begin{aligned} 1+2U_1' &= 2U_1 \\ 1-2U_2' &= 2(1-U_2) \end{aligned}. \tag{A.10}$$

Thus, U_1' and U_2' become, respectively, uniformly distributed in $[-½, 0[$ and $[0, ½]$. Besides, $|U_1'| = -U_1'$ and $|U_2'| = U_2'$, consequently,

$$\begin{aligned} 1-2|U_1'| &= 2U_1 \\ 1-2|U_2'| &= 2(1-U_2) \end{aligned}. \tag{A.11}$$

In addition, let $U = [U_1' \quad U_2']$, thus equations (A.8) and (A.9) may be written simply as

$$X = \mu - \frac{\sigma}{\sqrt{2}} \operatorname{sgn}(U) \ln(1-2|U|), \tag{A.12}$$

where U is uniformly distributed in $[-½, ½]$, $\operatorname{sgn}(\bullet)$ represents the sign function and the scale parameter has been replaced by $\sigma = \sqrt{2}b$.

Appendix B

Simulator Sample Results: OLoS Channel

This appendix presents some output results obtained for a sample OLoS channel.

B.1. Channel MPCs and Scatterers

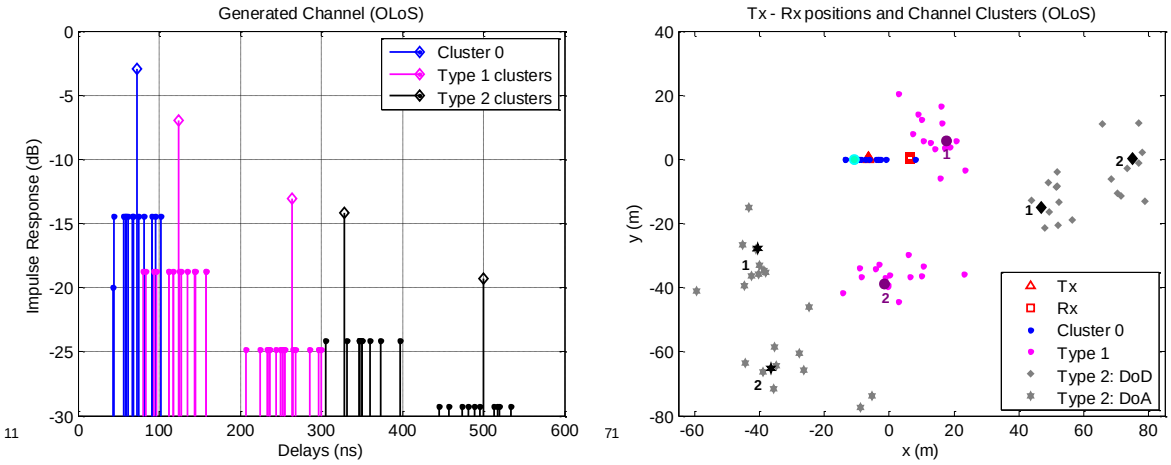

Figure B-1: Generated sample OLoS channel. **Left:** Channel MPCs. **Right:** Channel scatterers.

B.2. SISO Outputs

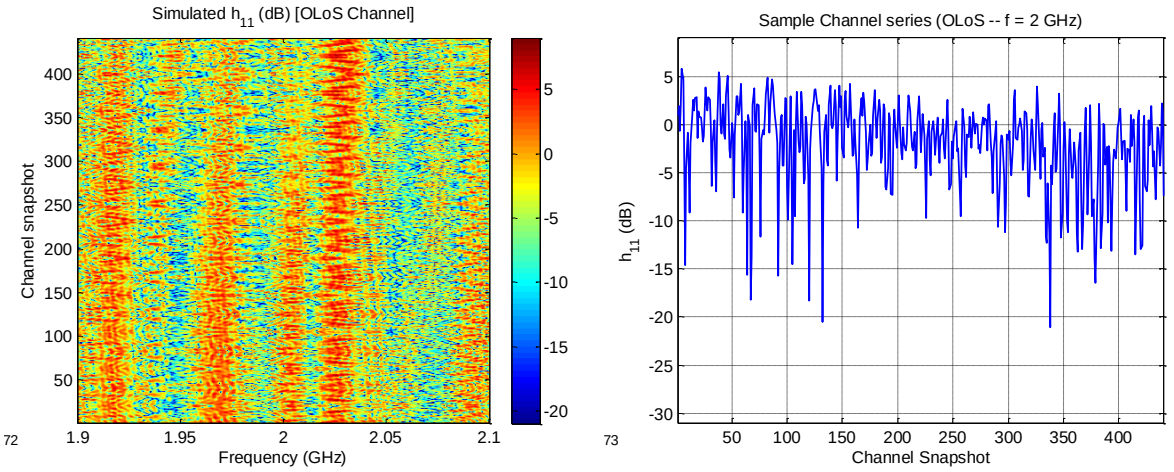

Figure B-2: Received amplitude for the generated sample OLoS channel. **Left:** Complete data set generated. **Right:** Channel realization series for f =2 GHz.

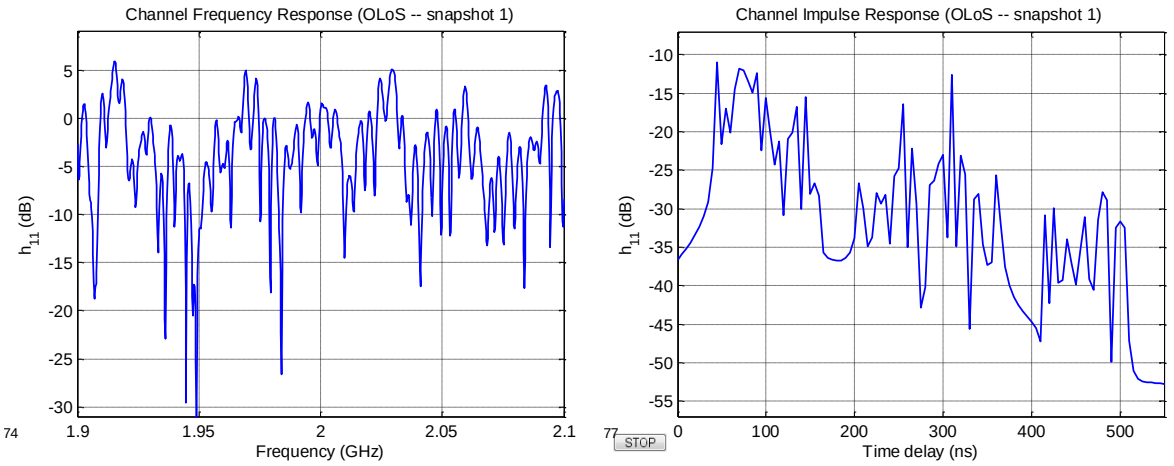

Figure B-3: One realization. **Left:** Frequency response. **Right:** Impulse response (obtained by IFFT).

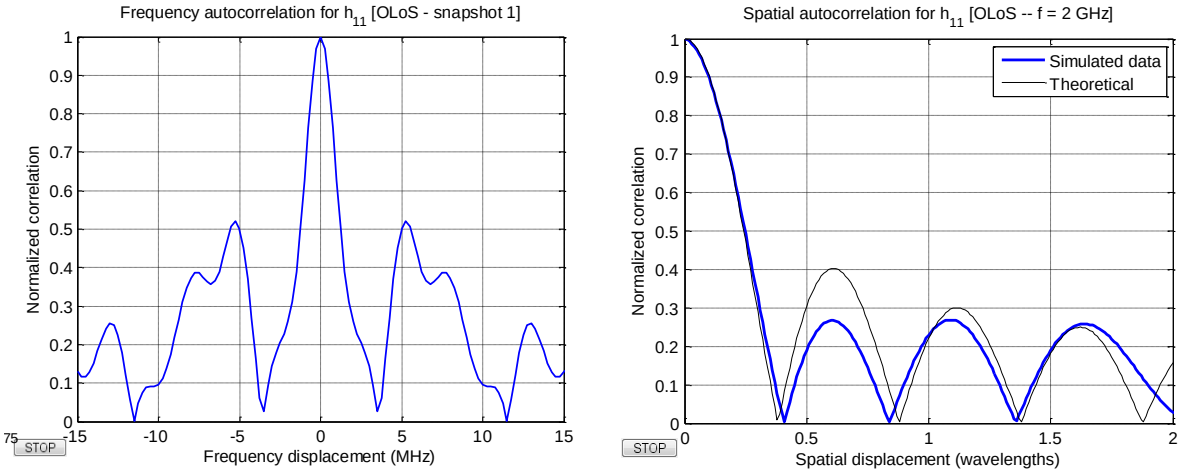

Figure B-4: Channel autocorrelation. **Left:** Frequency domain. **Right:** Spatial domain.

B.3. MIMO Outputs

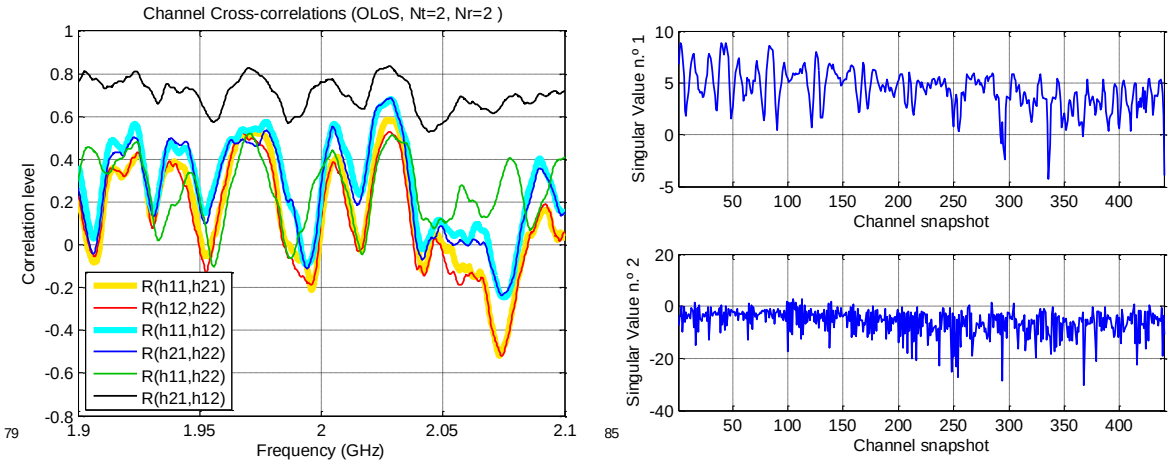

Figure B-5: **Left:** Channel cross-correlations. **Right:** CDF of the channel singular values for f =2 GHz.

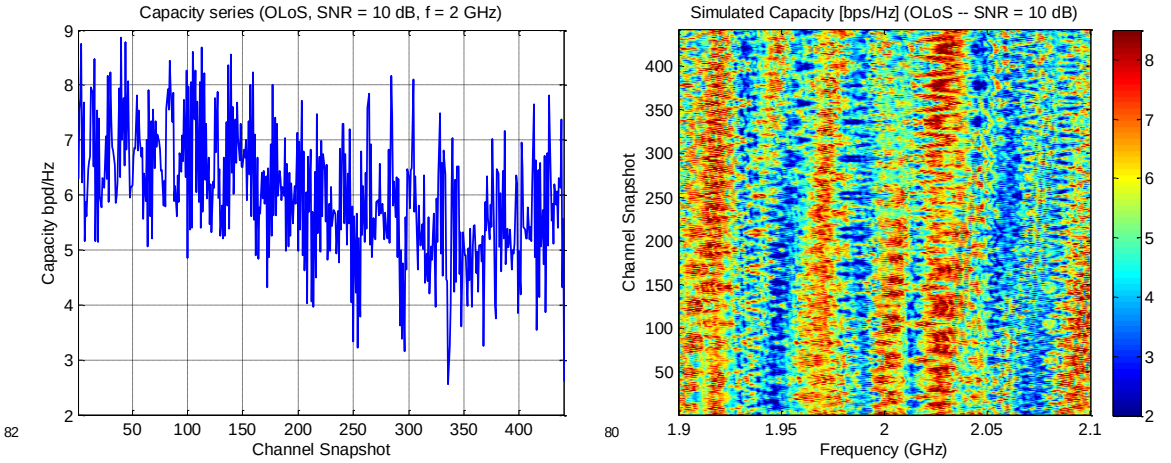

Figure B-6: Channel instantaneous capacity. **Left:** Series for f =2 GHz. **Right:** complete data set.

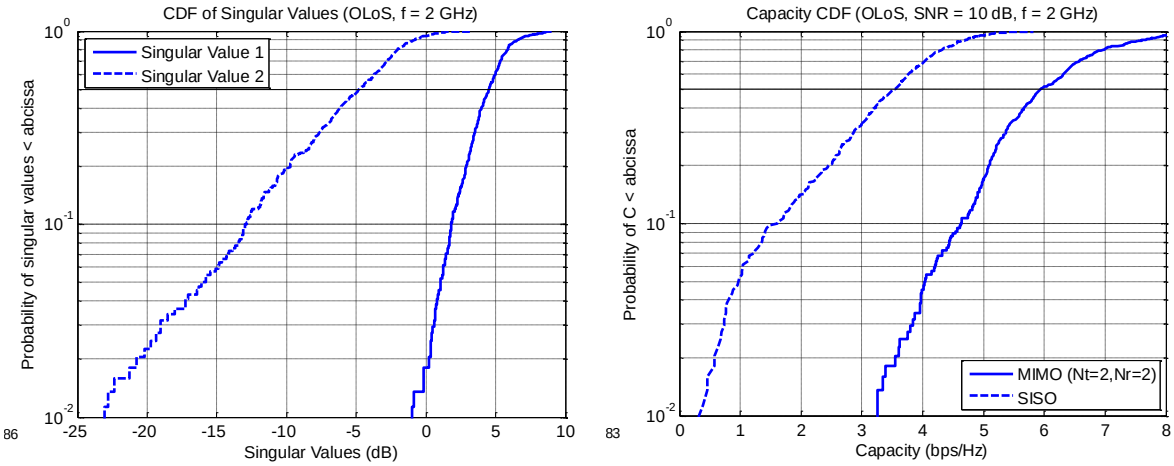

Figure B-7: CDFs of obtained series for f =2 GHz. **Left:** Singular values. **Right:** Channel capacity.

Appendix C

Measurements vs Simulations: Additional Results

This appendix presents additional output results obtained for the evaluation study presented in section 5.5 using the data set designated as "PAV 10".

C.1. Assessment of the SISO Characterization

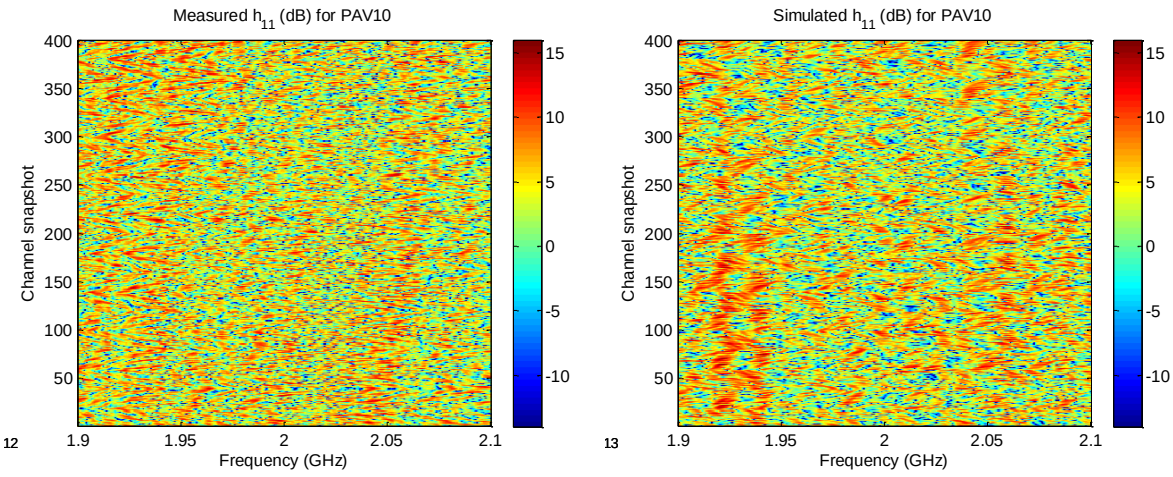

Figure C-1: Received amplitude (one antenna) for "PAV 10". **Left:** Measurements. **Right:** Simulations.

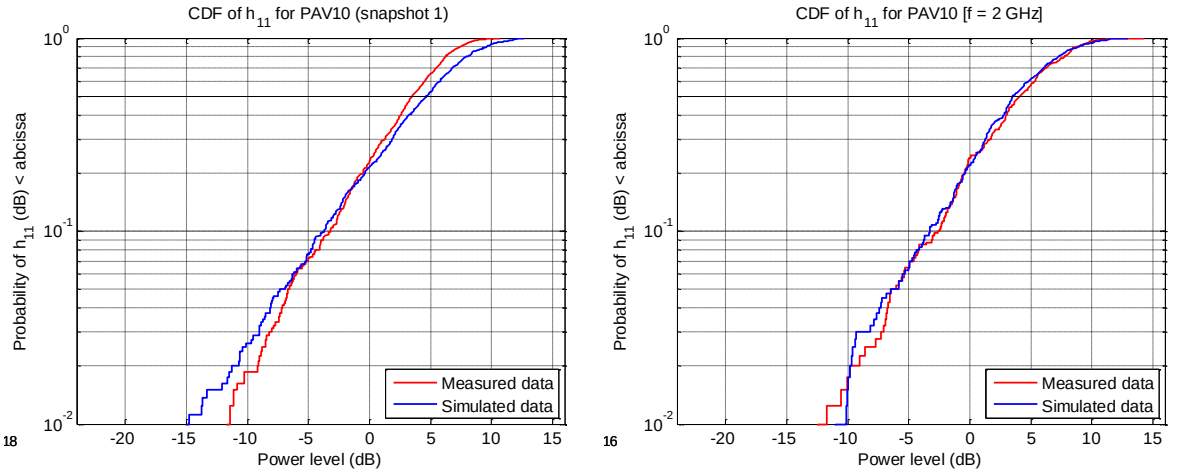

Figure C-2: CDF of received amplitude for "PAV 10" (cf. Figure 5-21). **Left:** CDF of the frequency response corresponding to one channel realization. **Right:** Amplitude CDF for f = 2 GHz.

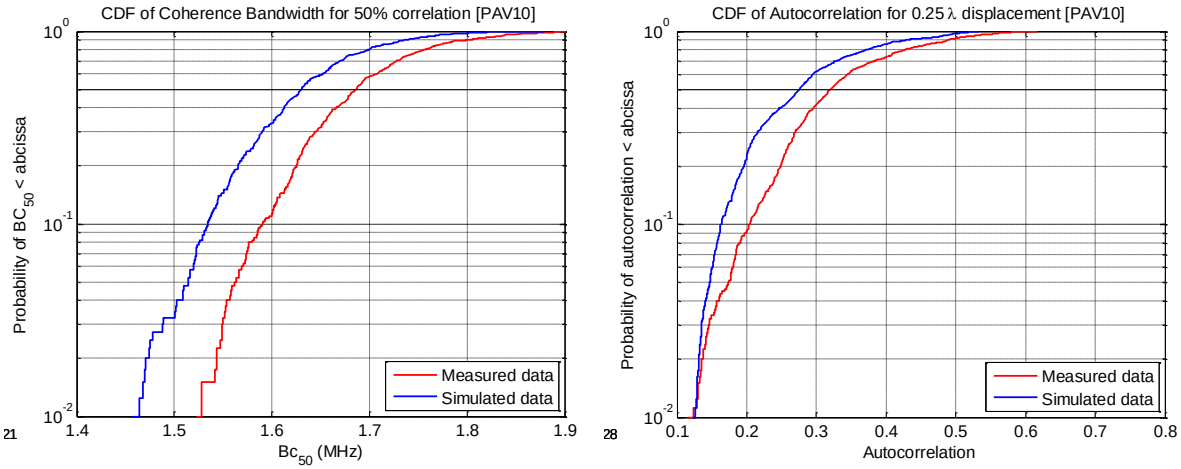

Figure C-3: CDF of channel autocorrelation (cf. Figure 5-22). **Left:** Coherence bandwidth for 50% correlation level. **Right:** Correlation level for a spatial displacement of $\lambda/4$.

C.2. Assessment of the MIMO Characterization

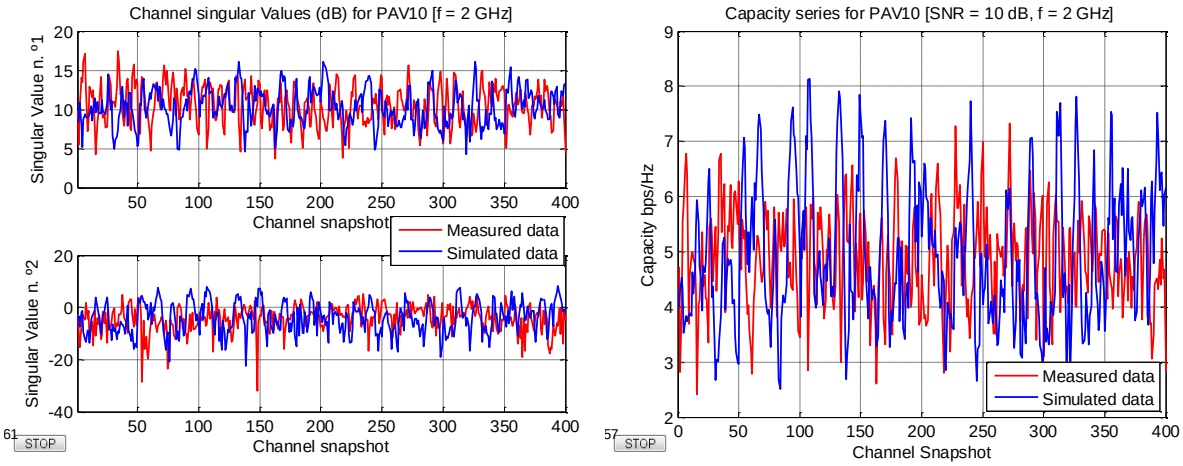

Figure C-4: Channel realization series for f = 2 GHz. **Left:** Singular values. **Right:** Capacity.

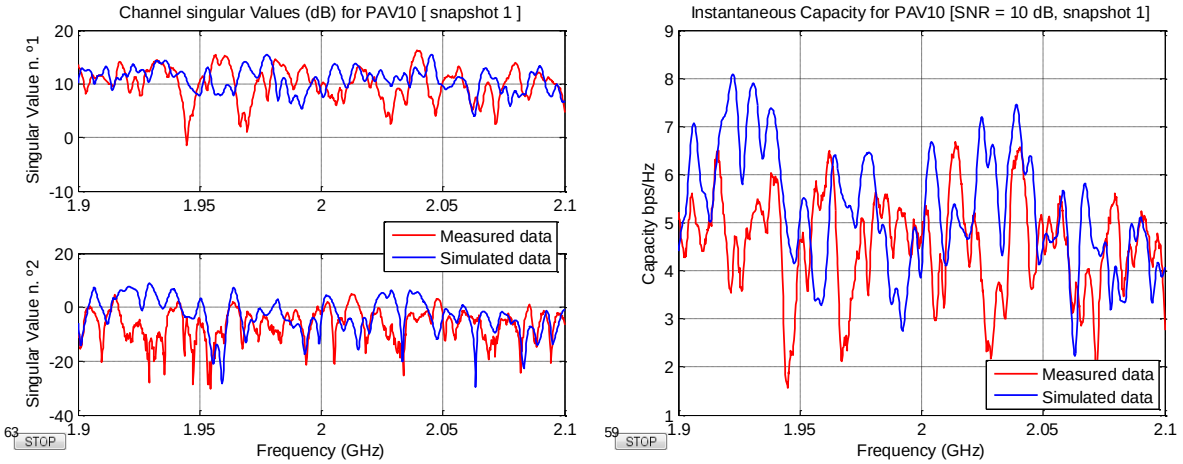

Figure C-5: One channel realization. **Left:** Singular values. **Right:** Capacity.

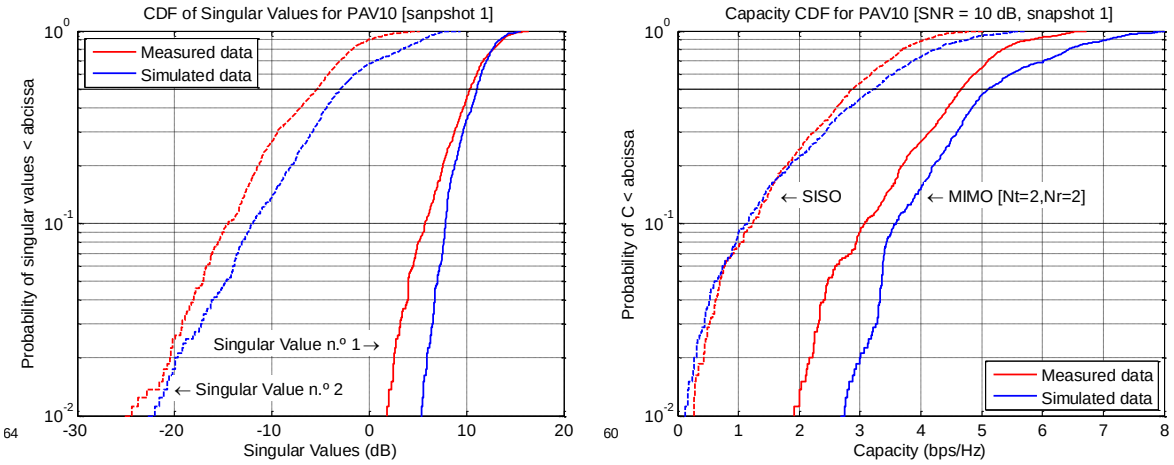

Figure C-6: CDFs of channel realization shown in Figure C-5. **Left:** Singular values. **Right:** Capacity.

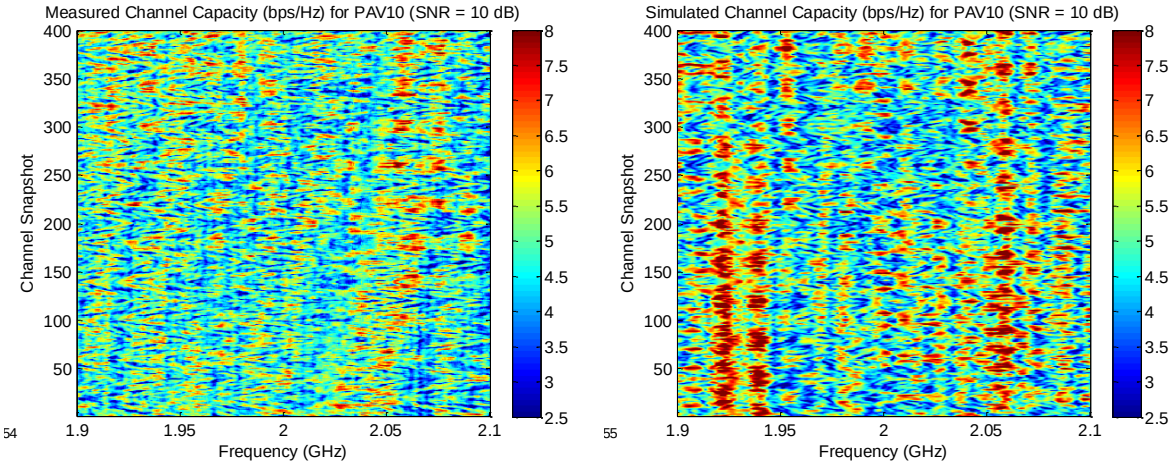

Figure C-7: Channel instantaneous capacity of the global data set.

References

[1] H. Krim and M. Viberg, "Two decades of array signal processing research - The parametric approach," *IEEE Signal Processing Magazine,* vol. 13, pp. 67-94, Jul 1996.

[2] L. C. Godara, "Applications of antenna arrays to mobile communications .1. Performance improvement, feasibility, and system considerations," *Proceedings of the IEEE,* vol. 85, pp. 1031-1060, Jul 1997.

[3] J. H. Winters, "Smart antennas for wireless systems," *IEEE Personal Communications,* vol. 5, pp. 23-27, Feb 1998.

[4] A. Wittneben, "A new bandwidth efficient transmit antenna modulation diversity scheme for linear digital modulation," in *Communications, 1993. ICC 93. Geneva. Technical Program, Conference Record, IEEE International Conference on*, 1993, pp. 1630-1634 vol.3.

[5] J. H. Winters, "The diversity gain of transmit diversity in wireless systems with Rayleigh fading," *IEEE Transactions on Vehicular Technology,* vol. 47, pp. 119-123, Feb 1998.

[6] L. C. Godara, "Application of antenna arrays to mobile communications .2. Beam-forming and direction-of-arrival considerations," *Proceedings of the IEEE,* vol. 85, pp. 1195-1245, Aug 1997.

[7] B. D. Van Veen and K. M. Buckley, "Beamforming: a versatile approach to spatial filtering," *ASSP Magazine, IEEE [see also IEEE Signal Processing Magazine]*, vol. 5, pp. 4-24, 1988.

[8] G. J. Foschini and M. J. Gans, "On Limits of Wireless Communications in a Fading Environment when Using Multiple Antennas," *Wireless Personal Communications,* vol. 6, pp. 311-335, 1998.

[9] E. Telatar, "Capacity of multi-antenna Gaussian channels," *European Transactions on Telecommunications,* vol. 10, pp. 585-595, Nov-Dec 1999.

[10] G. J. Foschini, D. Chizhik, M. J. Gans, C. Papadias, and R. A. Valenzuela, "Analysis and performance of some basic space-time architectures," *IEEE Journal on Selected Areas in Communications,* vol. 21, pp. 303-320, Apr 2003.

[11] S. Haykin, M. Sellathurai, Y. de Jong, and T. Willink, "Turbo-MIMO for wireless communications," *IEEE Communications Magazine,* vol. 42, pp. 48-53, Oct 2004.

[12] E. G. Larsson and P. Stoica, *Space-time block coding for wireless communications*. Cambridge: Cambridge University Press, 2003.

[13] A. Paulraj, R. Nabar, and D. Gore, *Introduction to space-time wireless communications*. Cambridge: Cambridge University Press, 2003.

[14] M. Jankiraman, *Space-time codes and MIMO systems*. Boston: Artech House, 2004.

[15] C. N. Chuah, D. N. C. Tse, J. M. Kahn, and R. A. Valenzuela, "Capacity scaling in MIMO wireless systems under correlated fading," *IEEE Transactions on Information Theory,* vol. 48, pp. 637-650, Mar 2002.

[16] T. S. Rappaport, *Wireless communications principles and practice*. Upper Saddle River, N.J.: Prentice Hall PTR, 1996.

[17] S. M. Alamouti, "A simple transmit diversity technique for wireless communications," *IEEE Journal on Selected Areas in Communications,* vol. 16, pp. 1451-1458, Oct 1998.

[18] V. Tarokh, N. Seshadri, and A. R. Calderbank, "Space-time codes for high data rate wireless communication: Performance criterion and code construction," *IEEE Transactions on Information Theory,* vol. 44, pp. 744-765, Mar 1998.

[19] V. Tarokh, H. Jafarkhani, and A. R. Calderbank, "Space-time block codes from orthogonal designs," *IEEE Transactions on Information Theory,* vol. 45, pp. 1456-1467, Jul 1999.

[20] G. D. Golden, C. J. Foschini, R. A. Valenzuela, and P. W. Wolniansky, "Detection algorithm and initial laboratory results using V-BLAST space-time communication architecture," *Electronics Letters,* vol. 35, pp. 14-16, Jan 7 1999.

[21] A. F. Naguib, N. Seshadri, and A. R. Calderbank, "Increasing data rate over wireless channels," *IEEE Signal Processing Magazine,* vol. 17, pp. 76-92, May 2000.

[22] D. Gesbert, M. Shafi, D. S. Shiu, P. J. Smith, and A. Naguib, "From theory to practice: An overview of MIMO space-time coded wireless systems," *IEEE Journal on Selected Areas in Communications,* vol. 21, pp. 281-302, Apr 2003.

[23] L. Z. Zheng and D. N. C. Tse, "Diversity and multiplexing: A fundamental tradeoff in multiple-antenna channels," *IEEE Transactions on Information Theory,* vol. 49, pp. 1073-1096, May 2003.

[24] R. W. Heath and A. J. Paulraj, "Switching between diversity and multiplexing in MIMO systems," *IEEE Transactions on Communications,* vol. 53, pp. 962-968, Jun 2005.

[25] P. Almers, E. Bonek, A. Burr, N. Czink, M. Debbah, V. Degli-Esposti, *et al.*, "Survey of channel and radio propagation models for wireless MIMO systems," *Eurasip Journal on Wireless Communications and Networking,* pp. -, 2007.

[26] C. Oestges and B. Clerckx, *MIMO wireless communications : from real-world propagation to space-time code design*, 1st ed. Oxford: Academic Press (Elsevier), 2007.

[27] J. D. Parsons, *The mobile radio propagation channel*, 2nd ed. Chichester: John Wiley & Sons, 2000.

[28] M. Steinbauer, A. F. Molisch, and E. Bonek, "The double-directional radio channel," *IEEE Antennas and Propagation Magazine,* vol. 43, pp. 51-63, Aug 2001.

[29] A. M. Sayeed, "Deconstructing multiantenna fading channels," *IEEE Transactions on Signal Processing,* vol. 50, pp. 2563-2579, Oct 2002.

[30] A. G. Burr, "Capacity bounds and estimates for the finite scatterers MIMO wireless channel," *IEEE Journal on Selected Areas in Communications,* vol. 21, pp. 812-818, Jun 2003.

[31] W. Debbah and R. R. Muller, "MIMO channel modeling and the principle of maximum entropy," *IEEE Transactions on Information Theory,* vol. 51, pp. 1667-1690, May 2005.

[32] J. P. Kermoal, L. Schumacher, K. I. Pedersen, P. E. Mogensen, and F. Frederiksen, "A Stochastic MIMO radio channel model with experimental validation," *IEEE Journal on Selected Areas in Communications,* vol. 20, pp. 1211-1226, Aug 2002.

[33] W. Weichselberger, M. Herdin, H. Ozcelik, and E. Bonek, "A stochastic MIMO channel model with joint correlation of both link ends," *IEEE Transactions on Wireless Communications,* vol. 5, pp. 90-100, Jan 2006.

[34] W. C. Y. Lee, "Effects on Correlation between 2 Mobile Radio Base-Station Antennas," *IEEE Transactions on Communications,* vol. Co21, pp. 1214-1224, 1973.

[35] P. Petrus, J. H. Reed, and T. S. Rappaport, "Geometrical-based statistical macrocell channel model for mobile environments," *IEEE Transactions on Communications,* vol. 50, pp. 495-502, Mar 2002.

[36] P. Petrus, J. H. Reed, and T. S. Rappaport, "Geometrically based statistical channel model for macrocellular mobile environments," *IEEE Globecom 1996 - Conference Record, Vols 1-3,* pp. 1197-1201, 1996.

[37] J. C. Liberti and T. S. Rappaport, "A geometrically based model for line-of-sight multipath radio channels," *1996 IEEE 46th Vehicular Technology Conference, Proceedings, Vols 1-3,* pp. 844-848, 1996.

[38] M. Lu, T. Lo, and J. Litva, "Physical spatio-temporal model of multipath propagation channels," *IEEE 47th Vehicular Technology Conference Proceedings,* pp. 810-814, 1997.

[39] O. Norklit and J. B. Andersen, "Diffuse channel model and experimental results for array antennas in mobile environments," *IEEE Transactions on Antennas and Propagation,* vol. 46, pp. 834-840, Jun 1998.

[40] J. Fuhl, A. F. Molisch, and E. Bonek, "Unified channel model for mobile radio systems with smart antennas," *IEE Proceedings-Radar Sonar and Navigation,* vol. 145, pp. 32-41, Feb 1998.

[41] D. S. Shiu, G. J. Foschini, M. J. Gans, and J. M. Kahn, "Fading correlation and its effect on the capacity of multielement antenna systems," *IEEE Transactions on Communications,* vol. 48, pp. 502-513, Mar 2000.

[42] C. Oestges, V. Erceg, and A. J. Paulraj, "A physical scattering model for MIMO macrocellular broadband wireless channels," *IEEE Journal on Selected Areas in Communications,* vol. 21, pp. 721-729, Jun 2003.

[43] A. F. Molisch, "A generic model for MIMO wireless propagation channels in macro- and microcells," *IEEE Transactions on Signal Processing,* vol. 52, pp. 61-71, Jan 2004.

[44] N. Czink and C. Oestges, "The COST 273 MIMO Channel Model: Three Kinds of Clusters," in *Spread Spectrum Techniques and Applications, 2008. ISSSTA '08. IEEE 10th International Symposium on*, 2008, pp. 282-286.

[45] A. F. Molisch, H. Asplund, R. Heddergott, M. Steinbauer, and T. Zwick, "The COST 259 directional channel model - Part I: Overview and methodology," *IEEE Transactions on Wireless Communications,* vol. 5, pp. 3421-3433, Dec 2006.

[46] A. Abdi and M. Kaveh, "A space-time correlation model for multielement antenna systems in mobile fading channels," *IEEE Journal on Selected Areas in Communications,* vol. 20, pp. 550-560, Apr 2002.

[47] A. A. M. Saleh and R. A. Valenzuela, "A Statistical-Model for Indoor Multipath Propagation," *IEEE Journal on Selected Areas in Communications,* vol. 5, pp. 128-137, Feb 1987.

[48] Q. H. Spencer, B. D. Jeffs, M. A. Jensen, and A. L. Swindlehurst, "Modeling the statistical time and angle of arrival characteristics of an indoor multipath channel," *IEEE Journal on Selected Areas in Communications,* vol. 18, pp. 347-360, Mar 2000.

[49] J. W. Wallace and M. A. Jensen, "Modeling the indoor MIMO wireless channel," *IEEE Transactions on Antennas and Propagation*, vol. 50, pp. 591-599, May 2002.

[50] T. Zwick, C. Fischer, and W. Wiesbeck, "A stochastic multipath channel model including path directions for indoor environments," *IEEE Journal on Selected Areas in Communications*, vol. 20, pp. 1178-1192, Aug 2002.

[51] "Spacial channel model for Multiple Input Multiple Output (MIMO) simulations," 3GPP TR 25.996 V6.1.0 Release 6 (2003-09).

[52] "Spacial channel model for Multiple Input Multiple Output (MIMO) simulations," 3GPP TR 25.996 V10.0.0 Release 10 (2011-04).

[53] G. Calcev, D. Chizhik, B. Goransson, S. Howard, H. Huang, A. Kogiantis, *et al.*, "A wideband spatial channel model for system-wide simulations," *IEEE Transactions on Vehicular Technology*, vol. 56, pp. 389-403, Mar 2007.

[54] V. Erceg, L. Schumacher, P. Kyritsi, A. Molisch, D. S. Baum, A. Y. Gorokhov, *et al.*, "TGn Channel Models," IEEE P802.11 Wireless LANs, 2004.

[55] V. Erceg, K. V. S. Hari, M. S. Smith, D. S. Baum, K. P. Sheikh, C. Tappenden, *et al.*, "Channel Models for Fixed Wireless Applications," IEEE 802.16 Broadband Wireless Access Working Group, IEEE 802.16.3c-01/29r4, 2001.

[56] "Mobile Release 1.0 Channel Model," WiMAX Forum®, 2008.

[57] D. S. Baum, J. Hansen, J. Salo, G. Del Galdo, M. Milojevic, and P. Kyosti, "An interim channel model for beyond-3G systems - Extending the 3GPP spatial channel model (SCM)," *Vtc2005-Spring: 2005 IEEE 61st Vehicular Technology Conference, Vols 1-5, Proceedings*, pp. 3132-3136, 2005.

[58] D. S. Baum, H. El-Sallabi, T. Jämsä, J. Meinilä, P. Kyösti, X. Zhao, *et al.*, "Final Report on Link Level and System Level Channel Models," IST-2003-507581 WINNER D5.4 v. 1.4, 2005.

[59] P. Kyösti, J. Meinilä, L. Hentilä, X. Zhao, T. Jämsä, C. Schneider, *et al.*, "WINNER II Channel Models," IST-4-027756 WINNER II D1.1.2 V1.2, 2007.

[60] P. Kyösti, J. Meinilä, L. Hentilä, X. Zhao, T. Jämsä, C. Schneider, *et al.*, "WINNER II interim channel models," IST-4-027756 WINNER II D1.1.1 V1.1, 2006.

[61] J. Meinilä, P. Kyösti, L. Hentilä, T. Jämsä, E. Suikkanen, E. Kunnari, *et al.*, "D5.3: WINNER+ Final Channel Models," Wireless World Initiative New Radio – WINNER+2010.

[62] F. Pérez Fontán and P. Mariño Espiñeira, *Modeling the wireless propagation channel : a simulation approach with Matlab*. Chichester, West Sussex [etc.] ,: John Wiley & Sons, 2008.

[63] P. Stoica and A. Nehorai, "MUSIC, maximum likelihood, and Cramer-Rao bound," *Acoustics, Speech and Signal Processing, IEEE Transactions on,* vol. 37, pp. 720-741, 1989.

[64] Y. L. C. De Jong and M. H. A. J. Herben, "High-resolution angle-of-arrival measurement of the mobile radio channel," *Antennas and Propagation, IEEE Transactions on,* vol. 47, pp. 1677-1687, 1999.

[65] R. Roy and T. Kailath, "ESPRIT-estimation of signal parameters via rotational invariance techniques," *Acoustics, Speech and Signal Processing, IEEE Transactions on,* vol. 37, pp. 984-995, 1989.

[66] M. Haardt and J. A. Nossek, "Unitary ESPRIT: how to obtain increased estimation accuracy with a reduced computational burden," *Signal Processing, IEEE Transactions on,* vol. 43, pp. 1232-1242, 1995.

[67] M. D. Zoltowski, M. Haardt, and C. P. Mathews, "Closed-form 2-D angle estimation with rectangular arrays in element space or beamspace via unitary ESPRIT," *Signal Processing, IEEE Transactions on,* vol. 44, pp. 316-328, 1996.

[68] J. Fuhl, J. P. Rossi, and E. Bonek, "High-resolution 3-D direction-of-arrival determination for urban mobile radio," *Antennas and Propagation, IEEE Transactions on,* vol. 45, pp. 672-682, 1997.

[69] J. A. Fessler and A. O. Hero, "Space-alternating generalized expectation-maximization algorithm," *IEEE Transactions on Signal Processing,* vol. 42, pp. 2664-2677, Oct 1994.

[70] M. Feder and E. Weinstein, "Parameter-estimation of superimposed signals using the EM algorithm," *IEEE Transactions on Acoustics Speech and Signal Processing,* vol. 36, pp. 477-489, Apr 1988.

[71] J. A. Fessler and A. O. Hero, "Penalized maximum-likelihood image-reconstruction using space-alternating generalized EM algorithms," *IEEE Transactions on Image Processing,* vol. 4, pp. 1417-1429, Oct 1995.

[72] P. J. Chung and J. F. Bohme, "Comparative convergence analysis of EM and SAGE algorithms in DOA estimation," *IEEE Transactions on Signal Processing,* vol. 49, pp. 2940-2949, Dec 2001.

[73] P. J. Chung and J. F. Bohme, "Experimental study of the EM and SAGE algorithms with application to sonar data," in *Sensor Array and Multichannel Signal Processing Workshop Proceedings*, 2002, pp. 77-81.

[74] B. H. Fleury, M. Tschudin, R. Heddergott, D. Dahlhaus, and K. I. Pedersen, "Channel parameter estimation in mobile radio environments using the SAGE algorithm," *IEEE Journal on Selected Areas in Communications,* vol. 17, pp. 434-450, Mar 1999.

[75] C. C. Chong, D. I. Laurenson, C. M. Tan, S. McLaughlin, M. A. Beach, and A. R. Nix, "Joint detection-estimation of directional channel parameters using the 2-D frequency domain SAGE algorithm with serial interference cancellation," in *ICC 2002: IEEE International Conference on Communications*, 2002, pp. 906-910 vol.2.

[76] M. Tschudin, R. Heddergott, and P. Truffer, "Validation of a high resolution measurement technique for estimating the parameters of impinging waves in indoor environments," in *Ninth IEEE International Symposium on Personal, Indoor and Mobile Radio Communications, Vols 1-3*, 1998, pp. 1411-1416.

[77] I. Ferreira, S. Mota, and A. Rocha, "Results from MIMO channel measurements and comparison to the extended Saleh-Valenzuela model," in *Antennas and Propagation (EuCAP), 2010 Proceedings of the Fourth European Conference on*, 2010, pp. 1-5.

[78] S. Mota, M. Outeiral Garcia, A. Rocha, and F. Perez Fontan, "Estimation of the Radio Channel Parameters using the SAGE Algorithm," *Radioengineering*, vol. 19, pp. 695-702, 2010.

[79] M. Wax and T. Kailath, "Detection of signals by information theoretic criteria," *IEEE Transactions on Acoustics Speech and Signal Processing*, vol. 33, pp. 387-392, 1985.

[80] Q. T. Zhang, K. M. Wong, P. C. Yip, and J. P. Reilly, "Statistical-analysis of the performance of information theoretic criteria in the detection of the number of signals in array-processing," *IEEE Transactions on Acoustics Speech and Signal Processing*, vol. 37, pp. 1557-1567, Oct 1989.

[81] E. Fishler, M. Grosmann, and H. Messer, "Detection of signals by information theoretic criteria: general asymptotic performance analysis," *IEEE Transactions on Signal Processing*, vol. 50, pp. 1027-1036, May 2002.

[82] B. Nadler, "Nonparametric detection of signals by information theoretic criteria: performance analysis and an improved estimator," *IEEE Transactions on Signal Processing*, vol. 58, pp. 2746-2756, May 2010.

[83] C. C. Chong, C. M. Tan, D. I. Laurenson, S. McLaughlin, M. A. Beach, and A. R. Nix, "A new statistical wideband spatio-temporal channel model for 5-GHz band WLAN systems," *IEEE Journal on Selected Areas in Communications*, vol. 21, pp. 139-150, Feb 2003.

[84] A. K. Jain, M. N. Murty, and P. J. Flynn, "Data clustering: A review," *ACM Computing Surveys*, vol. 31, pp. 264-323, Sep 1999.

[85] J. Han and M. Kamber, *Data mining concepts and techniques*, 2nd ed ed. San Francisco (CA): Morgan Kaufmann, 2006.

[86] N. Czink, P. Cera, J. Salo, E. Bonek, J. P. Nuutinen, and J. Ylitalo, "A Framework for Automatic Clustering of Parametric MIMO Channel Data including Path Powers," in *2006 IEEE 64th Vehicular Technology Conference*, 2006, pp. 114-118.

[87] C. Schneider, M. Bauer, M. Narandzic, W. A. T. Kotterman, and R. S. Thoma, "Clustering of MIMO channel parameters - performance comparison," in *2009 IEEE Vehicular Technology Conference*, 2009, pp. 309-313.

[88] N. Czink, P. Cera, J. Salo, E. Bonek, J. P. Nuutinen, and J. Ylitalo, "Automatic clustering of MIMO channel parameters using the multi-path component distance measure," presented at the WPMC'05, Aalborg, Denmark, 2005.

[89] D. Weihui, Z. Jianhua, G. Xinyin, Z. Ping, and W. Yufei, "Cluster Identification and Properties of Outdoor Wideband MIMO Channel," in *Vehicular Technology Conference, 2007. VTC-2007 Fall. 2007 IEEE 66th*, 2007, pp. 829-833.

[90] N. Czink, R. Y. Tian, S. Wyne, F. Tufvesson, J. P. Nuutinen, J. Ylitalo, *et al.*, "Tracking time-variant cluster parameters in MIMO channel measurements," presented at the 2007 Second International Conference in Communications and Networking in China, Vols 1 and 2, 2007.

[91] W. N. Wang and Y. J. Zhang, "On fuzzy cluster validity indices," *Fuzzy Sets and Systems*, vol. 158, pp. 2095-2117, Oct 1 2007.

[92] K. Kryszczuk and P. Hurley, "Estimation of the Number of Clusters Using Multiple Clustering Validity Indices," *Multiple Classifier Systems, Proceedings*, vol. 5997, pp. 114-123, 2010.

[93] X. L. L. Xie and G. Beni, "A Validity Measure for Fuzzy Clustering," *IEEE Transactions on Pattern Analysis and Machine Intelligence*, vol. 13, pp. 841-847, Aug 1991.

[94] U. Maulik and S. Bandyopadhyay, "Performance evaluation of some clustering algorithms and validity indices," *IEEE Transactions on Pattern Analysis and Machine Intelligence*, vol. 24, pp. 1650-1654, Dec 2002.

[95] M. K. Pakhira, S. Bandyopadhyay, and U. Maulik, "Validity index for crisp and fuzzy clusters," *Pattern Recognition*, vol. 37, pp. 487-501, Mar 2004.

[96] J. C. Bezdek and N. R. Pal, "Some new indexes of cluster validity," *IEEE Transactions on Systems Man and Cybernetics Part B-Cybernetics*, vol. 28, pp. 301-315, Jun 1998.

[97] S. Mota, M. O. Garcia, A. Rocha, and F. Perez-Fontan, "Clustering of the multipath radio channel parameters," in *Proc. of the 5th European Conference on Antennas and Propagation (EUCAP)*, 2011, pp. 3232-3236.

[98] S. Mota, F. Perez-Fontan, and A. Rocha, "Estimation of the Number of Clusters in Multipath Radio Channel Data Sets," *Antennas and Propagation, IEEE Transactions on*, vol. 61, pp. 2879-2883, 2013.

[99] S. Mota, A. Rocha, and F. Perez-Fontan, "Physical and statistical analysis of clustered multipath radio channel data," in *Antennas and Propagation (EuCAP), 2013 7th European Conference on*, 2013, pp. 3669-3673.

[100] S. Mota, N. Almeida, A. Rocha, and F. Perez-Fontan, "Results from a First Approach to a Point-Scatter Simulator for MIMO Radio Channel Modeling," in *Vehicular Technology Conference, 2009. VTC Spring 2009. IEEE 69th*, 2009, pp. 1-4.

[101] A. Leon-Garcia, *Probability and random processes for electrical engineering*, 2nd ed. Reading, Mass.: Addison-Wesley, 1994.